Western Graduate&PostdoctoralStudies

Western University
Scholarship@Western

Electronic Thesis and Dissertation Repository

8-19-2011 12:00 AM

Rational Design and Advanced Fabrication of Metallic Nanostructures for Surface-Enhanced Raman Spectroscopy

Betty Cristina Galarreta, *The University of Western Ontario*

Supervisor: Dr. François Lagugné-Labarthet, *The University of Western Ontario*
Joint Supervisor: Dr. Peter R. Norton, *The University of Western Ontario*
A thesis submitted in partial fulfillment of the requirements for the Doctor of Philosophy degree in Chemistry
© Betty Cristina Galarreta 2011

Follow this and additional works at: https://ir.lib.uwo.ca/etd

Part of the Analytical Chemistry Commons, Materials Chemistry Commons, Optics Commons, and the Physical Chemistry Commons

Recommended Citation

Galarreta, Betty Cristina, "Rational Design and Advanced Fabrication of Metallic Nanostructures for Surface-Enhanced Raman Spectroscopy" (2011). *Electronic Thesis and Dissertation Repository*. 220.
https://ir.lib.uwo.ca/etd/220

This Dissertation/Thesis is brought to you for free and open access by Scholarship@Western. It has been accepted for inclusion in Electronic Thesis and Dissertation Repository by an authorized administrator of Scholarship@Western. For more information, please contact wlswadmin@uwo.ca.

RATIONAL DESIGN AND ADVANCED FABRICATION OF METALLIC NANOSTRUCTURES FOR SURFACE-ENHANCED RAMAN SPECTROSCOPY

(Spine title: Design and Fabrication of Metallic Nanostructures for SERS)

(Thesis format: Integrated Article)

by

Betty Cristina Galarreta

Graduate Program in Chemistry

A thesis submitted in partial fulfillment
of the requirements for the degree of
Doctor of Philosophy

The School of Graduate and Postdoctoral Studies
The University of Western Ontario
London, Ontario, Canada

© Betty C. Galarreta 2011

THE UNIVERSITY OF WESTERN ONTARIO
School of Graduate and Postdoctoral Studies

CERTIFICATE OF EXAMINATION

Supervisor

Dr. François Lagugné-Labarthet

Co-Supervisor

Dr. Peter R. Norton

Supervisory Committeee

Examiners

Dr. Ricardo Aroca

Dr. Lyudmila Goncharova

Dr. T.K. Sham

Dr. Ron R. Martin

The thesis by

Betty Cristina Galarreta

entitled:

Rational Design and Advanced Fabrication of Metallic Nanostructures for Surface-Enhanced Raman Spectroscopy

is accepted in partial fulfillment of the
requirements for the degree of
Doctor of Philosophy

Date

Chair of the Thesis Examination Board

Abstract

One of the main challenges in analytical science and technology is to develop devices that provide unambiguously the chemical nature of the material of interest with the minimum intrusiveness, the smallest amount of analyte, and the shortest acquisition time. Among the promising methods for such purpose, optical spectroscopy such as surface-enhanced Raman scattering is considered a suitable option. This spectroscopic technique takes advantage of the interaction between an optical field and metallic nanostructures to magnify the electromagnetic field in the vicinity of the nanostructure, resulting in an amplified signal of the vibrational fingerprints of the adsorbed molecules onto the metallic surface.

In this Thesis, the rational design and fabrication of gold nanostructures optimized to probe molecular systems, at the monolayer level in a variety of configurations, is described. Using advanced nanofabrication techniques, two-dimensional arrays of metallic nanostructures were inscribed onto glass slides. The fabricated SERS platforms were first physically and optically characterized. Then, a rational analysis of the properties was performed through numerical calculations and experimental measurements, to estimate the polarization dependence of such nanostructures. The results led toward the optimization of the SERS platforms, and to the study of different complex surface molecular systems. Finally, these platforms were embedded in a microfluidic device for *in-situ* probing of molecules opening the possibility to develop micro total analysis in combination with Raman measurements.

Keywords

nanostructure, electron beam lithography, plasmon, finite-difference time domain, surface-enhanced Raman spectroscopy, vibrational spectroscopy, azobenzene polymer, self-assembled monolayer, micro-total analysis system, biotin, Streptavidin, aptamers

Dedication

A mi familia

(To my family)

Co-Authorship Statement

The following thesis contains material from previously published manuscripts. Dr. François Lagugné-Labarthet and Dr. Peter R. Norton were co-authors on the presented papers and were responsible for the supervision of Betty C. Galarreta over the course of her studies.

All published papers presented in Chapters 2, 3, 4 and 6, Betty C. Galarreta was the primary author responsible for the majority of experimental work, as well as the writing and revision of all drafts, including final manuscripts. Some data were jointly acquired and analyzed by co-authors, Dr. Nicolas Marquestaut, Etienne Harté, Ian Rupar, and Amanda Young. Betty is appreciative of their experimental assistance and useful discussions.

Dr. Valerie Guieu, of the Département de Pharmacochimie Moléculaire - UMR 5063 CNRS, Université de Grenoble, France, performed the fluorescence experiments described in Chapter 6. Her contribution is gratefully appreciated.

Acknowledgments

To begin, I would like to thank my supervisors: Dr. François Lagugné-Labarthet, and Dr. Peter Norton, for their advice and guidance when it was needed. This thesis would not have been possible without their encouragement and interest in my work.

Second, I would like to offer my gratitude to the staff from the Nanofabrication facility at Western: Tim Goldhawk, Dr. Todd Simpson and Dr. Rick Glew. Thank you for helping me with all the technical difficulties in the fabrication of my devices. I would like to give thanks to Mary Jane Walzak from Surface Science Western, for lending me their Raman microscope. A special thanks to Dr. Seyed Tadayyon for his help with the AFM microscope, and Etienne Harté for building some of the optical setup in the lab. I owe my gratitude to all the former and current members of the FLL and Norton group. Thank you very much for providing experimental aid, interesting discussions, and several forms of support.

I would like to give special thanks to Christine Séguin, Amanda Leclair and Sarvesh Varma for their constant moral support. Most importantly, thank you for letting me into your lives, and making me feel at home. All your help and kindness was essential for the completion of this thesis.

My deepest appreciation goes to my family, for the encouragement to pursue my goals, and for always being there to offer the kindest words in my moments of crisis: “Muchísimas gracias mami y Ana Paula por ser como son”.

Finally, I would like to thank to all the people that have helped me and inspired me with their words and behavior during the development of this dissertation project.

Table of Contents

CERTIFICATE OF EXAMINATION ii

Abstract iii

Dedication iv

Co-Authorship Statement v

Acknowledgments vi

Table of Contents vii

List of Tables xii

List of Figures xiii

List of Abbreviations, Symbols and Nomenclature xx

List of Appendices xxiv

Chapter 1: General Introduction 1

1.1. Overview 1

1.2. Plasmonic properties of metals 4

1.2.1. Plasmon 4

1.2.2. Surface plasmon 4

1.2.3. Localized surface plasmon resonance 8

1.3. Surface-Enhanced Raman Scattering 12

1.3.1. SERS Enhancement Mechanisms 12

1.4. Fabrication of SERS Substrates – General Considerations 16

1.5. Scope of Thesis 17

1.6. References 18

Chapter 2: Design, Fabrication and Characterization of Plasmonic Nanostructures 22

2.1. Introduction 22

2.2. Current fabrication methods of two-dimensional nanostructures 23
2.3. Plasmonic properties of metallic nanostructures 25
2.4. Design of hexagonal array of nanotriangles 29
2.5. Experimental methods 31
2.5.1. Fabrication 31
2.5.2. Physical characterization 32
2.5.3. Extinction spectra 33
2.6. Results and discussion 34
2.6.1. Optical properties of a series of Fischer's patterns 34
2.6.2. Polarized LSPR spectral contributions 37
2.7. Conclusions 39
2.8. References 40
Chapter 3: Modeling the Electric Field Distribution around a Hexagonal Array of Gold Nanotriangles 44
3.1. Introduction 44
3.2. Experimental methods to detect the LSPR in nanostructures 45
3.2.1. In the far-field 45
3.2.2. In the near-field 46
3.3. Numerical approximations to model the LSPR in nanostructures 47
3.3.1. Discrete dipole approximation (DDA) 48
3.3.2. Finite element method (FEM) 49
3.3.3. Finite-difference time domain (FDTD) 50
3.4. Theoretical calculations 51
3.5. Results and discussion 53
3.5.1. Polarized LSPR spectral contributions 53

3.5.2. Total near-field enhancement spectra of Fischer's pattern: length and polarization effect 56

3.5.3. Contribution of the electric field components 58

3.5.4. Near-field distribution 59

3.5.5. Localized electric field. 62

3.6. Conclusion 71

3.7. References 72

Chapter 4: Mapping Hot-Spots in Hexagonal Arrays of Metallic Nanotriangles with Azobenzene Polymer Thin Films 76

4.1. Introduction 76

4.2. Azobenzene polymers 78

4.2.1. Photochemical process 78

4.2.2. Azobenzene polymer as a tool for near-field detection 80

4.3. Experimental methods 82

4.3.1. Calculations 82

4.3.2. Preparation of nanotriangle arrays 83

4.3.3. Azobenzene polymer photoinduced migration 84

4.3.4. Surface characterization 84

4.4. Results and discussion 84

4.4.1. Electric field distribution 84

4.4.2. Topographic analysis 86

4.5. Conclusions 91

4.6. References 92

Chapter 5: Detecting the Enhancement Factor on Hexagonal Array of Nanotriangles 95

5.1. Introduction 95

5.2. Enhancement Factor 96

5.2.1. Single molecule enhancement factor....97
5.2.2. Analytical enhancement factor....98
5.2.3. SERS substrate enhancement factor....99
5.3. Experimental consideration....100
5.3.1. Scattering volume....101
5.3.2. Number of molecules probed....102
5.4. Experimental section....103
5.4.1. Fabrication of SERS platforms. 103
5.4.2. Extinction spectra....103
5.4.3. Physical characterization 103
5.4.4. Functionalization of the SERS platforms 104
5.4.5. Raman spectra....104
5.5. Results and discussion....105
5.5.1. Optimization of the parameters of the microscope 105
5.5.2. Characteristics of SERS Platforms....108
5.5.3. SERS Surface Enhancement Factor 109
5.6. Conclusions....113
5.7. References....114
Chapter 6: Applications and Integration of SERS Platforms in Bioanalysis....116
6.1. Introduction....116
6.2. Self-assembled monolayers (SAMs)....118
6.3. Streptavidin/biotin molecular system....120
6.4. Ochratoxin A-binding aptamer 121
6.5. Micro-total analysis system (μ-TAS)....123
6.6. Materials and methods....124

6.6.1. Fabrication of SERS platforms 124
6.6.2. Functionalization of gold. 124
6.6.3. Fabrication of microfluidic SERS device 127
6.6.4. Physical characterization 129
6.6.5. Finite difference time domain (FDTD) calculations 130
6.6.6. Extinction spectra 130
6.6.7. Raman spectroscopy 131
6.6.8. Fluorescence spectroscopy 131
6.7. Results and discussion 132
6.7.1. Optimization of SERS platforms 132
6.7.2. Streptavidin/biotin monolayer assemblies 134
6.7.3. OTA aptameric sensor 140
6.8. Conclusion 146
6.9. References 147
Chapter 7: Conclusions and Prospects 154
7.1. References 158
Appendix A. 160
Copyrights 160
Curriculum Vitae 163

List of Tables

Table 3.1. Summary of the localized electric field enhancement of Fischer's pattern lattice unit irradiated with Py and Px-beam 63

Table 5.1. Experimental conditions of the Raman experiments 104

Table 6.1. Methods for the characterization of alkanethiolated SAMs on gold 120

Table 6.2. Experimental conditions of the Raman spectra taken. 131

Table 6.3. Assignment of the Raman bands in the spectra of Strep, and Strep/BAT complex. 139

Table 6.4. Assignment of the Raman bands in the spectra of Aptamer and Aptamer/OTA complex. 145

List of Figures

Figure 1.1. Cross section of some optical processes. RS: Raman scattering, RRS: resonance Raman scattering, SERS: surface enhanced Raman scattering, SERRS: surface enhanced resonance Raman scattering 3

Figure 1.2. Dielectric function of gold and silver according to the Lorentz-Drude model. 5

Figure 1.3. Surface plasmon distribution over a continuous metallic surface. 6

Figure 1.4. Dispersion relation (black) and propagation length (dash line) of a surface plasmon on a gold-air interface according to the Drude model..... 7

Figure 1.5. Localized surface plasmon resonance of metallic nanospheres. 8

Figure 1.6. Calculated extinction, scattering and absorption cross section of gold nanospheres surrounded by water according to Mie's theory. 10

Figure 1.7. Illustration of two configurations of a pair of metallic particles interacting with polarized light 11

Figure 1.8. Brief illustration of the chemical mechanism contributions: charge transfer (a) and resonance Raman (b). 15

Figure 2.1. NSL and surface patterns made with 470 nm beads (a) and without beads (b and c) coated with 40 nm gold over a glass substrate 23

Figure 2.2. Scanning electron micrographs of 2-D nanostructures written using EBL. . 24

Figure 2.3. Transmission (a), reflection (b), and dark field (c) systems used to detect the LSPR properties in far-field. 25

Figure 2.4. Schematic representation of different LSPR multipoles of a metallic nanosphere 26

Figure 2.5. DDA calculation of the plasmonic properties of a silver nanotriangles 29

Figure 2.6. SEM image of hexagonal array of nanotriangles fabricated by EBL 30

Figure 2.7. Fabrication process of nanostructured platforms fabricated by EBL.....32

Figure 2.8. Scheme of the extinction measurement setup.....33

Figure 2.9. SEM image of a Fischer's pattern array (a) and of an array fabricated with a dose of 100 $\mu C/cm^2$ (b). Effect of the area dose exposure on the length size (c) and gap distance (d) of the individual triangles. 34

Figure 2.10. Atomic force micrograph of an array of Fischer's pattern made of gold over a microscope coverslip (a), and its cross section image (b).....35

Figure 2.11. Extinction spectra of Fischer's pattern made at different area dose exposure percentage with respect to the nominal area dose -100 $\mu C/cm^2$- (a), and summary of the peaks trends (b) 37

Figure 2.12. Extinction spectra of an array of Fischer's pattern-A (357 nm length size and 184 nm gap distance). 39

Figure 3.1. Yee cell.....50

Figure 3.2. Schematic representation of a periodic array of Fischer's pattern where the lattice unit has been highlighted and the points studied have been labeled 53

Figure 3.3. Experimental extinction spectra of Fischer's pattern-A (357 nm length size, 184 nm gap distance and 40 nm gold thickness) (a), calculated extinction spectra (b), calculated near-field intensity spectra for one unit lattice of Fischer's pattern-A (c). All the spectra shown here were spatially correlated. 55

Figure 3.4. Calculated sum of the total near-field per area irradiated for the arrays of Fischer's patterns, when the length size of the triangles is modified (L:

100-300 nm), and when the incoming polarization is along the Y (a,c) or X (b, d) axes. Spectra in (a) and (b) have been spatially correlated 57

Figure 3.5. Intensity spectra of the total electric field of Fischer's pattern-A lattice unit as well as the contribution to the intensity of each component when the incoming light is X polarized (a) and Y polarized (b).....59

Figure 3.6. Calculated electric field distribution of a L100-nm unit lattice at 704 nm wavelength (a) and at 603 nm wavelength (b), when irradiated with a Py-input (row 1 and 3) and a Px-input (row 2 and 4): total electric field (column 1), in-plane X component (column 2), in-plane Y component (column 3), and out-of-plane Z component (column 4).....61

Figure 3.7. Calculated localized electric field spectra ($|E|^2/|E_0|^2$) for P1 when irradiated with a Py (a, c) and Px input (b, d). Spectra on A and B have been spatially correlated and the direction of the arrows indicates the increase on the length of the triangles in the array (L100-300 nm).....64

Figure 3.8. Calculated localized electric field spectra ($|E|^2/|E_0|^2$) for P2 when irradiated with a Py (a, c) and Px input (b, d). Spectra on A and B have been spatially correlated and the direction of the arrows indicates the increase on the length of the triangles in the array (L100-300 nm).....66

Figure 3.9. Calculated localized electric field spectra ($|E|^2/|E_0|^2$) for P3 when irradiated with a Py (a, c) and Px input (b, d). Spectra on A and B have been spatially correlated and the direction of the arrows indicates the increase on the length of the triangles in the array (L100-300 nm).....68

Figure 3.10. Calculated localized electric field spectra ($|E|^2/|E_0|^2$) for P4 when irradiated with a Py (a, c) and Px input (b, d). Spectra on A and B have been spatially correlated and the direction of the arrows indicates the increase on the length of the triangles in the array (L100-300 nm).....70

Figure 4.1. Chemical structure of p(DR1M-co-MMA) 11% (a) and absorption spectrum of the azobenzene moiety (b).....78

Figure 4.2. Surface Modification of a thin film of p(DR1M-co-MMA) after irradiation at 532 nm with a 100 mW/cm2 focalized and linearly polarized Gaussian beam (objective used 50x, N.A=0.63). 79

Figure 4.3. Photochemical induced reaction of azobenzene moieties. 80

Figure 4.4. AFM image of a silver bow tie assembly coated with an azobenzene polymer thin film after being irradiated at 532 nm with a linearly polarized beam perpendicular (a) and parallel (b) to the interparticle distance axis of the dimer. Their respective calculated near-field intensity distribution ($|E_{x/y}|^2$, $|E_z|^2$, $|E_{tot}|^2$) are also shown in the same row (c-h) 81

Figure 4.5. Schematic representation of the molecular migration of azobenzene polymer under the effect of an in-plane (a) and an out-of-plane (b) polarized field 82

Figure 4.6. SEM image of a hexagonal array of gold nanotriangles (length: 327±20 nm, gap: 116±15 nm, metallic thickness: 40±5 nm).....83

Figure 4.7. Calculated electric field distribution of hexagonal array of gold (a) and silver (b-d) nanotriangles irradiated with a linearly polarized beam parallel to the bow tie axis at 532 nm. The left side column represents the electric field distribution calculated 10 nm above the metallic surface, while the other two columns show the cross section intensity maps of these structures, one parallel to the polarization of the incoming beam (middle column) and another one with a 60 degrees rotation (right side column), as shown on the inset. In the case of silver, the in-plane component parallel to the bow tie axis (c), as well as the out-of-plane electric field component (d) are also illustrated.....85

Figure 4.8. AFM images of a periodic array of silver nanotriangles coated with pDR1M thin film before (a) and after (b) being irradiated with a linearly polarized laser beam at 532 nm parallel to the bow tie axis. 87

Figure 4.9. AFM image of a hexagonal array of silver (top set) and gold (bottom set) nanotriangles coated with pDR1M before (a, c) and after irradiation (b, d). The cross section profiles (e) and (f) show the change in topography before (green) and after (red) irradiation for silver and gold at the center of the lattice, respectively. The cross sections profiles (g) and (h) show the change of topography along the bow tie assemblies parallel to the input polarized light, as shown in the inset; and the profiles (i) and (j) show the change of topography along the bow tie assemblies oriented at 60° with respect to the direction of the linearly polarized light, as shown in the inset. 88

Figure 4.10. Calculated electric field distribution cross sections for gold (left side) and for silver (silver) hexagonal array of nanotriangles along the center of the lattice unit, when irradiated with a linearly polarized beam is polarized along the X direction, as shown on the insets. The total (a, b) and partial field components: $|E_x|^2$ (c, d), $|E_y|^2$ (e, f), $|E_z|^2$ (g, h) are shown 90

Figure 5.1. Effect of the microscope internal filters (a) and of the pinhole size (b) in the intensity of the Raman laser and of the silicon signal, respectively. 106

Figure 5.2. Raman map of the border of a silicon thin film (a) and profile intensity plot of the silicon signal that allows the estimation of effective scattering area (b). 107

Figure 5.3. Intensity profile of silicon when the distance from the focal point is tuned. 108

Figure 5.4. Summary of the properties of the Fischer's patterns studied 109

Figure 5.5. Raman spectrum of concentrated solution of benzenethiol when excited with a 632.8 nm laser 110

Figure 5.6. SERS spectra of adsorbed benzenethiol on SERS platforms 111

Figure 5.7. SERS enhancement factor (a) and plasmon band (b) of the arrays fabricated by a different area dose 112

Figure 6.1. Guanine quartet of thrombin-binding aptamer showing the characteristics vibration frequencies 123

Figure 6.2. Sreptavidin/biotin functionalization process of nanostructured platforms. 125

Figure 6.3. Fabrication process of master mold by photolithography and casting of PDM layers. 128

Figure 6.4. Binding process of SERS platforms and DPMS microfluidic layer (a) and optical picture of the assembled device..... 129

Figure 6.5. SEM image of fabricated array of gold nanotriangles over a glass slide. The inset plot shows the extinction spectrum of the platform together with the Raman excitation wavelength (λ= 632.8 nm) and the Raman signals regions used for the Raman experiment (a). Localization of the hot spot spots over a lattice unit of the SERS platform The input linear polarization direction is along a bow tie axis (b) 133

Figure 6.6. AFM scans of the gold nanostructured platforms before (a) and after being functionalized with BAT:OEG mixture (b), and when Strep assembled with the BAT molecules (c).The graph (d) summarizes the height difference and the average arithmetic roughness value (Ra) of samples a-c..... 135

Figure 6.7. Raman spectra of Strep(s) and Strep(ads) on a functionalized gold SERS platform (a). Raman spectra BAT and OEG present at the surface of the gold SERS platform and at the surface of a bare gold substrate (b). 137

Figure 6.8. Effect of OTA on the fluorescence anisotropy of the aptamer. 141

Figure 6.9. Raman spectrum (a) of ochratoxin-A (b) in solid state. 143

Figure 6.10. Raman spectra of aptamer SAM on bare gold surface ($Apt_{(bare\ Au)}$), aptamer SAM functionalized in a SERS platform integrated in a microfluidic device ($Apt_{(SERS\ \mu\text{-}fluidic)}$) and after OTA was adsorbed on this functionalized nanostructured platform($Apt/OTA_{(SERS\ \mu\text{-}fluidics)}$). 144

List of Abbreviations, Symbols and Nomenclature

α	polarizability of a molecule
δ	bending mode
β	in-plane bending mode
ε_o	permittivity of free-space
ε_d	permittivity of a dielectric
ε_m	complex dielectric function of a metal
λ	wavelength of light
λ_{LSPR}	localized surface plasmon resonance excitation band
μ_M	surface density of the hot-spots present in a metallic nanostructure
μ_S	surface density of the the molecular probes adsorbed on a metallic surface
μ-TAS	micro-total analysis system
$\eta_\perp$	axial detection effieciency
$\eta(\rho,z)$	detection efficiency profile
ν	stretching mode
$\bar{\nu}$	wavenumber
ϖ_p	plasma frequency
$\sigma_{ext/sca/abs}$	extinction/scattering/absorption cross section
$(\sum\|E\|^2)$/area	sum of the total electric field intensity ratio per area
χ	shape factor of a nanoparticles
ω_0	waist of the excitation profile
2D	two dimensional
A_M	total metallic surface area
A_{eff}	effective scattered area
AEF	analytical enhancement factor
Ala	alanine
Apt	aptamer
Apt/OTA	aptamer/OTA complex
AFM	atomic force microscopy
BAT	11-mercaptoundecanoic-[13-biotinoylamido-4,7,10-trioxatrydecanyl]amide
BAT/OEG	mixture of BAT and OEG
bio	biotin
BT	benzenethiol
c	speed of light
c_{RS}	concentration of molecules probed under non-SERS conditions
CCD	charge-coupled device
CHEM	non-resonant chemical mechanism
CT	charge transfer mechanism
e	electron charge
d	diameter of a nanoparticles

$d\sigma_{SERS/RS}^{SM}/d\Omega$	differential SERS/Raman cross section
DDA	discrete dipole approximation
DDDI	doubly distilled deionized water
E_o	incident electromagnetic field
E_f	Fermi energy level
$\|E\|^2$	total electric field intensity
$\|E_{x/y/z}\|^2$	Intensity of the x/y/z electric field component
EBL	electron beam lithography
EF	enhancement factor
F-Apt	5′-F-GAT-CGG-GTG-TGG-GTG-GCG-TAA-AGG-GAG-CAT-CGG-ACA-3′
F-Scr	5’-F-GGC-ATA-GAG-GCG-GCG-AGA-GGT-CTG-TCA-GGT-GTA-GAG-3’
f.a.s.	fluorescence anisotropy signal
FDTD	finite-difference time domain
EM	electromagnetic
FEM	finite element method
Glu	glutamic acid
H_{eff}	effective scattered height
HS-Apt	5′-HS-$(CH_2)_6$-GAT-CGG-GTG-TGG-GTG-GCG-TAA-AGG-GAG-CAT-CGG-ACA-3′
HFSS	high frequency structure simulator
HOMO	highest occupied molecular orbital
I_{SERS}^{SM}	SERS intensity of a single molecule
$\langle I_{RS}^{SM} \rangle$	average Raman intensity of a single molecule
$[I_{SERS}^{SM}]$	average of SERS intensity for every possible orientation of a probed molecule
I^R	Raman intensity
$I(\rho, z)$	excitation intensity profile
$I_{vv/vh}$	vertically/horizontally polarized components of the fluorescence emission after excitation by a vertically polarized light
$Im(\varepsilon_m)$	imaginary component of the dielectric function of a metal
K_d	dissociation constant
k_{SP}	surface plasmon wave vector
l_{SP}	propagation property of a surface plasmon
	electron density of the metal
L100-nm	hexagonal array of nanotriangles (length side of triangle = 100 nm)
LSPR	localized surface plasmon resonance
LUMO	lowest unoccupied molecular orbital
Lys	lysine
m	electron mass
$n\ N_{Surf}$	number of molecules adsorbed on a surface
NA	numerical aperture
NSL	nanosphere lithography
NSOM	near-field scanning optical microscopy

OEG	[11-mercaptoundec-11-yl]tryethylene glycol
OTA	ochratoxin-A
p(DR1M-*co*-MMA)	poly[2-[4-((4-nitrophenyl)azo)-phenyl)ethylamino]ethyl methacrylate-*co*-methyl methacrylate]
P_i	polarization induced
Px/y	linearly polarized along X/Y axis
PBS	phosphate buffer solution
PDMS	polydimethylsiloxane
PEEM	photoemission electron microscopy
Phe	phenylalanine
PM-IRRAS	polarization modulationinfrared reflection absorption
Q_M	normal coordinate of a molecules
$Q_{ext/sca/abs}$	extinction/scattering/absorption efficiency
r	radius of a metallic nanoparticles
r.coil	random coil
R/R_f	anisotropy ratio between the aptamer of various concentrations whether target molecule is present (R), and theaptamer in the absence of the target molecule (R_f)
Ra	average roughness
$Re(\varepsilon_m)$	real component of the dielectric function of a metal
RIE	reactive ion etching
RR	resonance Raman mechanism
RRS	resonance Raman spectroscopy/scattering
RS	Raman spectroscopy/scattering
r.t.	room temperature
S-Au	sulfur-gold interaction
SAM	self-assembled monolayer
SEIRA	surface-enhanced infrared absorption
SELEX	Systematic evolution of ligands by exponential enrichment
SEM	scanning electron microscopy
Ser	serine
SERS	surface-enhanced Raman spectroscopy/scattering
SERRS	surface-enhanced resonance Raman spectroscopy/scattering
SMD	single molecule detection
SMEF	single molecule enhancement factor
SP	surface plasmon
SPR	surface plasmon resonance
SSEF	SERS substrate enhancement factor
STEM	scanning transmission electron microscopy
STM	scanning tunneling microscopy
Strep	Streptavidin from *S. avidinii*
$Strep_{(ads)}$	adsorbed Streptavidin
Strep/BAT	Streptavidin/biotinylated complex
TERS	tip-enhanced Raman spectroscopy/scattering
TBS	Tris buffer solution
Thr	threonine
Trp	tryptophan

Tyr	tyronsine
V_{eff}	effective scattering volume
VSFG	vibrational sum frequency generation
X-R-SH	alkanethiol
XPS	X-ray photoelectron spectroscopy

List of Appendices

Appendix A. 160

Chapter 1: General Introduction

1.1. Overview

The design of optical devices with the ability to perform a rapid screening of small molecule analytes is a topic of interest in different fields of science, such as biology, medical diagnosis, environmental monitoring, security screening and many others.[1,2] One of the goals in the development of analytical methods is to combine very high spatial and temporal resolution techniques with molecular spectroscopy to probe different materials and to understand some fundamental chemical processes. To accomplish this, it is required to use platforms that can be patterned and functionalized and which present a high sensitivity to detect trace molecules at the monolayer level. In addition, when combined with optical techniques, it is important to minimize the intensity of the laser source and the exposure time, in order to avoid photo-damage of the molecules of interest. Last, in cases when spatial resolution of the measurement is necessary, the platforms can be combined with other techniques to obtain sub-wavelength spatial resolution and identify unambiguously a material or chemical system.

In this context, Raman scattering microscopy is desirable because it is highly specific, it is label-free, and it presents a high spatial resolution when combined with optical confocal microscopy. The specificity of Raman spectroscopy relies on the detection of the vibrational fingerprint of molecules. The Raman spectrum of a molecule is the result of the different vibrational modes of a polarizable molecular system, as described in **(1)**.

$$I^R \propto \left|\frac{\partial \alpha}{\partial Q_M}\right|^2 \qquad \textbf{(1)}$$

Herein, the Raman intensity (I^R) of the different vibrational modes is proportional to a change of the molecular polarizability of the molecule (α) along the normal coordinate of the molecule (Q_M).[2-4] Therefore, it is possible to discriminate between different chemicals

in a system by having a good understanding of their individual vibrational spectra.[5,6] Furthermore, the Raman spectrum of a molecule in some cases can provide relevant information related to the orientation and conformation of molecules at surfaces, interfaces and in anisotropic materials.[7,8] As opposed to fluorescence spectroscopy, Raman spectroscopy does not require the use of a molecular label in order to promote detection, and is simply based on the scattering of the chosen molecules of interest.[9,10] The only requirement for normal Raman spectroscopy measurements is to have Raman active modes, with no intrinsic fluorescence, and that present a vibrational mode than can be discriminated from the rest of the sample such as the matrix or a surface. Another great advantage of Raman scattering is the possibility to combine it with optical microscopy, as the scattered light is generally in the visible spectrum. Therefore, the combination of a Raman system together with confocal microscopy allows one to conduct measurements with a spatial resolution limited by the Rayleigh criterion, which is about half the wavelength of the excitation light.[3] The aforementioned advantages, as well as the technological developments in lasers, optical filters, confocal microscopes and detector sensitivity, have provided renewed interest for Raman spectroscopy as a powerful analytical technique.[1-4]

Despite its benefits, Raman spectroscopy (RS) has a poor sensitivity, thereby limiting its application. Compared to other optical methods, such as fluorescence spectroscopy, RS has a scattering cross section that is ten orders of magnitude smaller (**Figure 1.1**), resulting in a poor signal/noise ratio or long acquisition time. In Raman spectroscopy, only one out of 10^8 photons will be scattered.[4] This physical limitation can be circumvented by using either electronic resonance conditions, usually referenced as resonance Raman scattering (RRS), or metallic surfaces to conduct surface-enhanced Raman scattering (SERS) measurements. In RRS, the incident wavelength of light matches an allowed electronic transition of the molecule of interest. This technique has been shown to enhance the signal by a factor around 10^3-10^6 and to increase the scattering cross section from 10^{-30} to 10^{-25} cm^2/steradian.[11] This approach is often used for Raman

measurements in biosciences, where the incident wavelength matches the UV absorption of the biomolecules.[1,3,4]

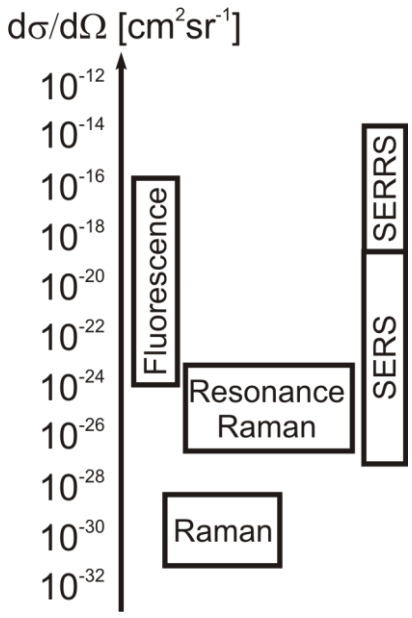

Figure 1.1. Cross section of some optical processes. RS: Raman scattering, RRS: resonance Raman scattering, SERS: surface enhanced Raman scattering, SERRS: surface enhanced resonance Raman scattering.[11]

On the other hand, under optimum conditions, namely using metallic nanostructures, the Raman scattering cross section can be enhanced by ten orders of magnitude, i.e. 10^{-20} cm^2/steradian. This technique is known as SERS. Finally, the Raman signal can lead to even higher improvements by combining both RRS and SERS, also called surface enhanced resonance Raman scattering (SERRS in **Figure 1.1**), allowing one to potentially detect single molecules (SMD).[11]

The main focus of this PhD thesis concerns the design, fabrication, optimization, and characterization of SERS platforms for bio-applications. In the next paragraphs, the

principles of surface plasmons and their consequences in surface enhanced phenomena are reviewed.

1.2. Plasmonic properties of metals

The field enhancement and localization at the surface of a metal constitutes a general field of research known as plasmonics. To better understand Raman-SERS, one must first introduce the notion of the surface plasmon and localized surface plasmon resonance.

1.2.1. Plasmon

The collective oscillation of the conduction electrons in a metal in response to an electromagnetic disturbance, such as an optical field, receives the name of "plasmon". For materials with dimensions larger than the wavelength of the incident light ($d >> \lambda$), these oscillations occur at the plasma frequency (ϖ_p), as described in **(2)**. Where ε_o represents the permittivity of free-space, *n* the electron density of the metal, *e* the electron charge, and *m* the electron mass.[12]

$$\varpi_p = \frac{1}{2\pi}\sqrt{\frac{ne^2}{m\varepsilon_o}} \qquad \textbf{(2)}$$

1.2.2. Surface plasmon

When this excitation is confined to the interface between a conductive material, with a complex dielectric function ($\varepsilon_m = Re(\varepsilon_m) + iIm(\varepsilon_m)$), and a dielectric, with a real permittivity (ε_d), it is called a surface plasmon (SP). To detect the SP mode, the material must have a negative real and a positive imaginary dielectric constant, which is the case of metals.[13,14] From the different metals available, silver and gold are commonly used as their plasmon frequency is in the UV-Visible-Near IR range, as shown in **Figure 1.2**.

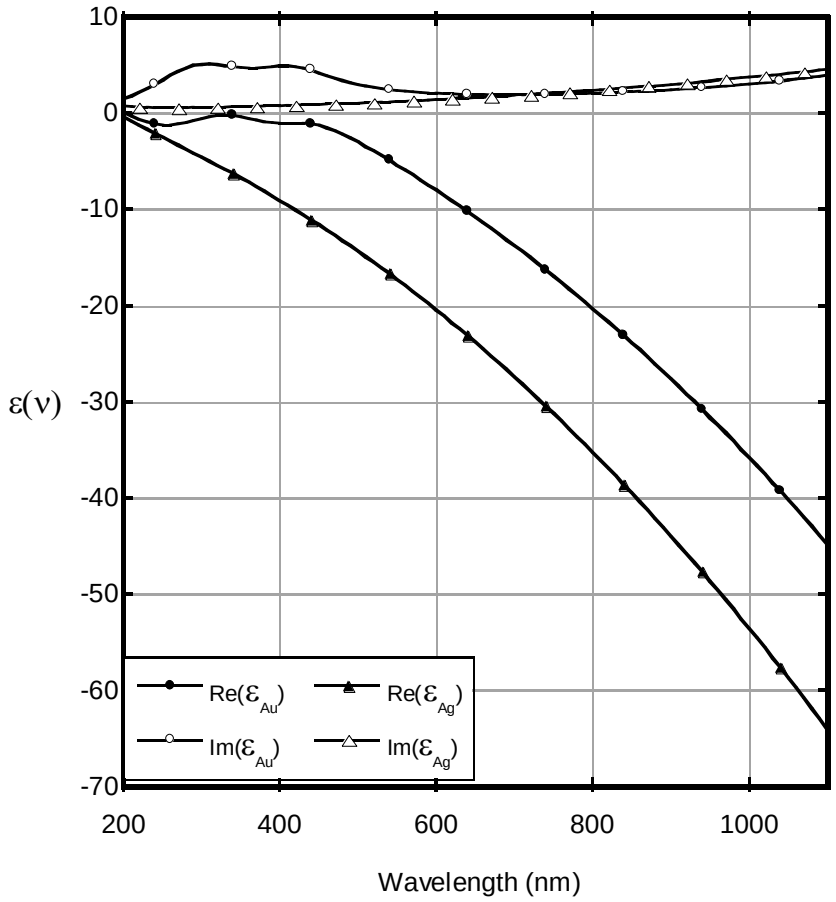

Figure 1.2. Dielectric function of gold and silver according to the Lorentz-Drude model.

When an external electromagnetic field shifts the free conduction electrons of the metals, it produces a charge distribution at the surface leading to a standing or a propagating SP modes, as schematically represented in **Figure 1.3**. This illustration represents the distribution of the electromagnetic field. On the one hand, the field has a component perpendicular to the surface with an evanescent nature as it goes away from the surface, and with a smaller magnitude within the metal than in the dielectric. On the other hand, the scheme also shows the propagating nature of the electric and magnetic modes along the surface plane.

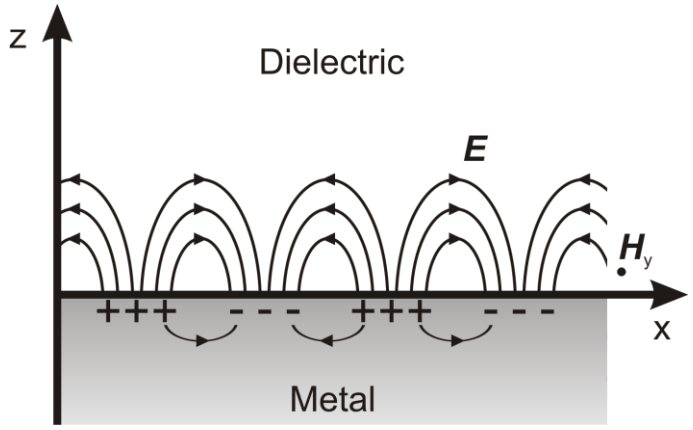

Figure 1.3. Surface plasmon distribution over a continuous metallic surface. [15]

Mathematically, the nature of the SP mode can be explained by solving Maxwell's equations. The interaction between light and the surface charge density produces a change in the complex wave vector (k_{SP}) different than that of a free-space photon at the same frequency ($k_o = \varpi/c$), shown in **(3)**. [12,15-17]

$$k_{SP} = k_o \sqrt{\frac{\varepsilon_d \varepsilon_m}{(\varepsilon_d + \varepsilon_m)}} \qquad \textbf{(3)}$$

The real part of k_{SP} contains the evanescent property of the mode. **Figure 1.4** shows the dispersion of light and the momentum mismatch between the SP and the free-space photon ($\hbar k_{SP} > \hbar k_o$).

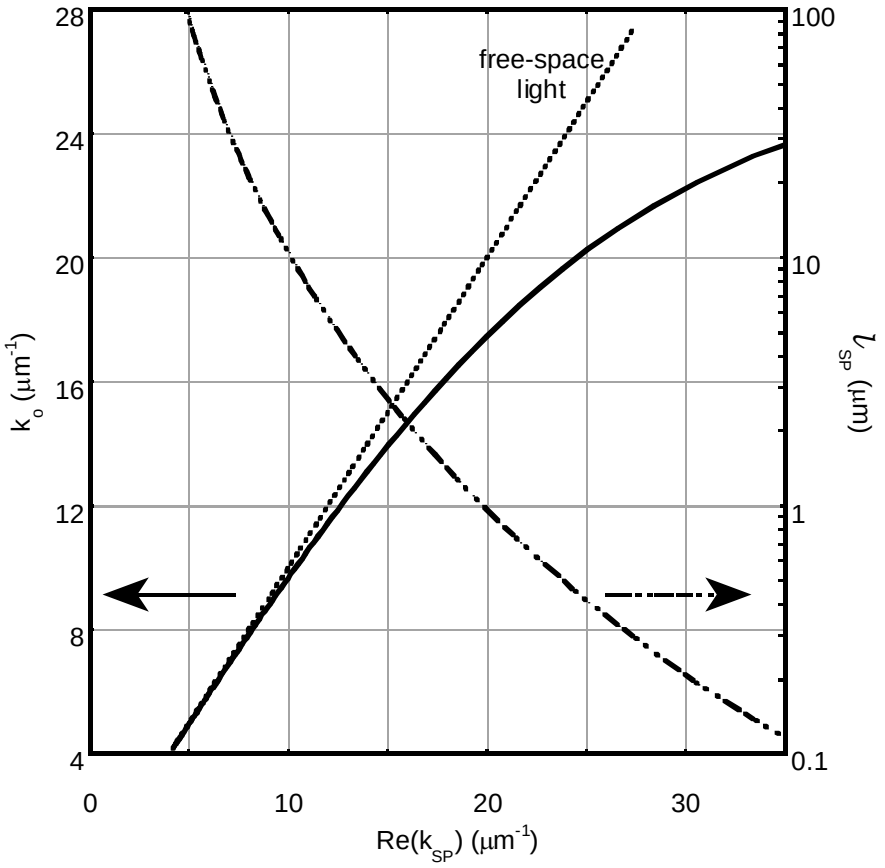

Figure 1.4. Dispersion relation (black) and propagation length (dash line) of a surface plasmon on a gold-air interface according to the Drude model. [15]

As a result, an additional momentum must be generated to overcome this difference of the free-space photon, and this is the momentum responsible of the evanescence. **Figure 1.4** also shows the propagation property of the SP mode, expressed as l_{SP} and defined in **(4)**, where the smaller the dimensions of $Re(k_{SP})$ the larger the distance that the SP mode can travel along the surface.[15]

$$l_{SP} = \frac{2}{[Re(k_{SP})]^3} \frac{[2\pi Re(\varepsilon_m)]^2}{\lambda^2 Im(\varepsilon_m)} \qquad \textbf{(4)}$$

In the case of metallic nanostructures, with a particle size comparable to the incident electromagnetic wavelength of light ($d < \lambda$), it is possible to observe two main effects

associated with localized surface plasmon resonance (LSPR). First, similar to SP, the LSPR is sensitive to the dielectric environment and the complex permittivity of the metal.[13] However, the electromagnetic field can penetrate the nanoparticle and shift the metallic electron cloud with respect to the center of the nanostructure generating an oscillator, as illustrated in **Figure 1.5**.

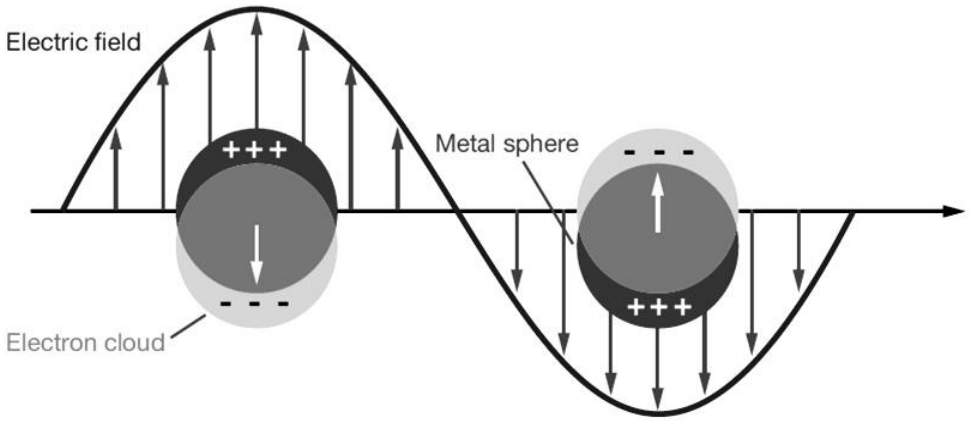

Figure 1.5. Localized surface plasmon resonance of metallic nanospheres. [13]

This leads to a LSPR frequency that are typically found in Visible-NIR range in noble metals.[12,13,18] The second effect of LSPR refers to a change in amplitude of the electromagnetic field, which can be greatly enhanced by several orders of magnitude at specific regions in the surface. These regions are often referred as "hot-spots" and present an evanescent nature, as the intensity of the field rapidly decays with distance.[12,18]

1.2.3. Localized surface plasmon resonance

In contrast to SP, the LSPR mode are not only susceptible to changes in the dielectric environment and the conductive material, but also to the size, the geometry, and the interparticle distance between the nanostructures.[13] Different theories have tried to

explain this susceptibility, and the calculation of the LSPR modes is well described for small nanospheres and spheroids using Mie and Gans theories, respectively.[12,13,19,20] A full description of these theories goes beyond the scope of this thesis, but a simplified example is discussed hereafter to emphasize the different parameters that must be considered when one once calculates the optical properties relating to LSPR.

The localized surface plasmon resonance of metallic nanostructures can be studied in the far field by detecting the extinction (σ_{ext}) and scattering (σ_{sca}) cross section. The susceptibility of the dielectric surroundings, the size, and the shape, affect the LSPR frequency, and as a result, the signal in the cross section spectra of these nanostructures. Mie developed an analytical solution to predict the extinction, scattering and absorption ($\sigma_{abs} = \sigma_{ext} - \sigma_{sca}$). A simplified version of the equations is expressed in ***(5)*** and ***(6)***, for a small nanoparticles ($d << \lambda$) with only one LSPR mode active.[12,13,19] These two equations show how the optical properties of the nanoparticles is sensitive to the dielectric constants of the metal and the dielectric, as well as to the geometry (χ: shape factor), and the size or volume (V) of the nanoparticle.[12]

$$\sigma_{ext} = \frac{18\pi\varepsilon_d{}^{3/2}V}{\lambda^4}\frac{Im(\varepsilon_m)}{[Re(\varepsilon_m)+\chi\varepsilon_d]^2+[Im(\varepsilon_m)]^2} \quad \textbf{(5)}$$

$$\sigma_{sca} = \frac{32\pi^4\varepsilon_d{}^2V^2}{\lambda^4}\frac{[Re(\varepsilon_m)-\varepsilon_d]^2+[Im(\varepsilon_m)]^2}{[Re(\varepsilon_m)+\chi\varepsilon_d]^2+[Im(\varepsilon_m)]^2} \quad \textbf{(6)}$$

Thus, if gold nanospheres ($\chi = 2$) of 20 nm radius are surrounded by water ($\varepsilon_d = 1.7$), then the LSPR extinction peak (λ_{LSPR}) is predicted at ~520 nm, as shown in **Figure 1.6**, after using ***(5)*** and ***(6)***, and explains the red color of a colloidal solution of gold nanospheres.[12]

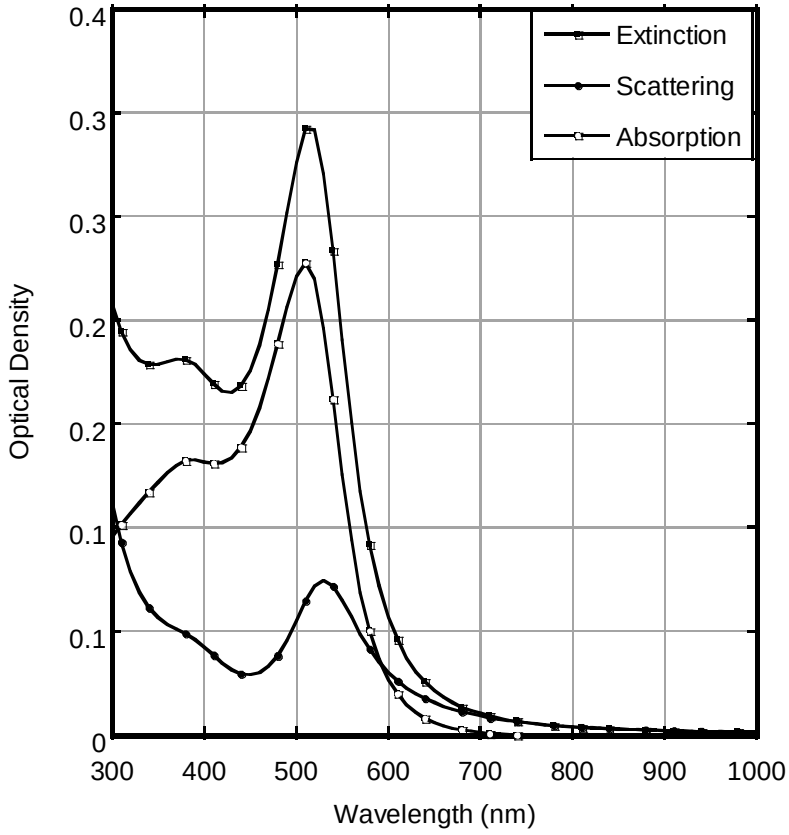

Figure 1.6. Calculated extinction, scattering and absorption cross section of gold nanospheres surrounded by water according to Mie's theory.

Furthermore, the interactions between the nanostructures also affect the LSPR. For example, when the interparticle distance between two nanoparticles is small enough, their electromagnetic excited fields can couple to each other, increasing and confining the excited fields.[16,19] Moreover, the polarization direction of the incident light can also affect such couplings. This is explained qualitatively in **Figure 1.7**, where the polarization of the incident light can be oriented either (**a**) parallel or (**b**) perpendicular to a pair of particles and have different effects. When parallel, the field of both particles will increase the enhancement because both are in the same direction. When they are perpendicular, the two fields will oppose to each other and present a smaller enhancement. From these observations it is critical that the polarization direction as well as the distance between

adjacent metallic particles must be considered to optimize the excitation of LSPR in ideal conditions.[16]

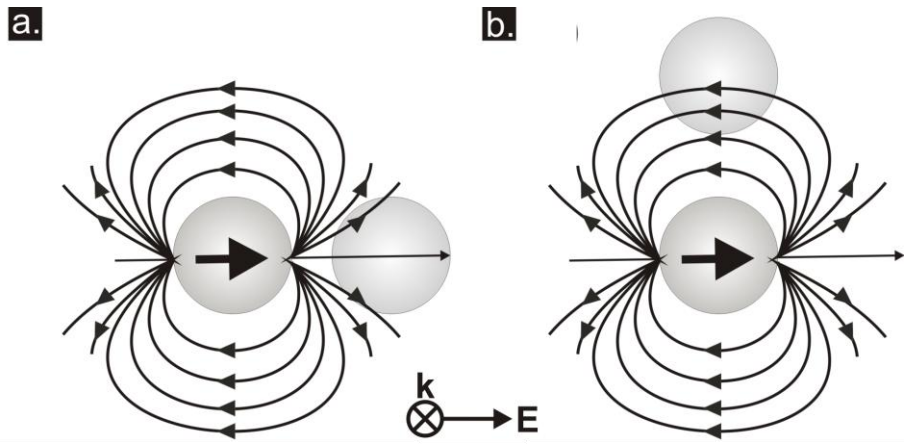

Figure 1.7. Illustration of two configurations of a pair of metallic particles interacting with polarized light. [16]

For nanostructures beyond nanospheres and nanospheroids, the suggested theories are limited, and numerical methods are generally required to predict their optical behavior. Electrodynamic calculations, such as finite-difference time domain (FDTD) method, discrete dipole approximation (DDA) or finite element method (FEM), are used by different groups in order to model the LSPR spectrum. More details about these methods and their use in the detection of the LSPR properties of more complex structures will be given in Chapters 3.

To summarize, plasmons, and in particular localized surface plasmon resonance, are able to guide and enhance the surrounding electromagnetic field. Therefore, their physical properties can be exploited for applications in analytical science, more specifically, as an element in the fabrication of optical sensors that improve the resolution of the Raman signal of trace chemicals.

1.3. Surface-Enhanced Raman Scattering

Surface-enhanced Raman scattering (SERS) was discovered in 1974 by Fleischmann,[21] and correctly interpreted in 1977 by Albrecht and Van Duyne[22,23] Both of them attempted to explain the strong increase in the Raman signals (around 10^5 times) observed for pyridine adsorbed onto rough silver electrodes.[21] The unusual intensity was attributed to an increase in the number of excitable molecules because of the larger surface area offered by the electrodes. However, three years later, these two groups recognized that this marked enhancement could not be explained simply by the increased surface area and SERS was subsequently proposed.[19] The interest in SERS increased drastically in the 1990s when researchers reported the use of SERS for single molecule detection (SMD),[20,24,25] reinforcing SERS as a powerful analytical tool and a very active research field due in part to the development of nanofabrication methods.

1.3.1. SERS Enhancement Mechanisms

The SERS enhancement mechanism has been well explained in the literature.[19,26-28] Complementary models have been proposed to explain the different origins of SERS and can be classified into two groups: the electromagnetic mechanism and the chemical mechanism. The first one is considered to be the dominant factor, accounting for a signal enhancement of approximately 10^6 times, and is directly connected to field of plasmonics, developed in Section 1.1. The latter factor involves an overlap of different factors that consider the interaction between the metal and the adsorbed molecule, or the chemical nature of the adsorbed molecule itself. The nature of the chemical mechanism is considered to be a combination of contributions that could come from the metal-molecule complex formation (charge transfer and resonant Raman scattering), molecular orientation and surface selection rules.

1.3.1.1. Electromagnetic Mechanism of SERS

As stated earlier, the electromagnetic (EM) mechanism is the result of the localized surface plasmon resonance of metallic nanostructures. From the mathematical analysis of the LSPR extinction cross section of nanoparticles ***(3)***, one can infer that the electromagnetic field intensity due to LSPR is sensitive to a change in wavelength of light($E_{LSPR}(\lambda)$), as it is dependent on the complex dielectric function of the metal. Therefore, when a molecule adsorbed on the surface of a metallic nanostructure is irradiated with an excitation laser source, the intensity of the incident field ($|E_o(\lambda)|^2$) is enhanced ($E_{LSPR}(\lambda)$), as well as the Raman scattering light ($E_{LSPR}(\lambda \pm \lambda_R)$), as described in **(7)**.[13,29,30]

$$EF_{EM}(\lambda) = \frac{|E_{LSPR}(\lambda)|^2 |E_{LSPR}(\lambda \pm \lambda_R)|^2}{|E_o(\lambda)|^4} \quad \textbf{(7)}$$

The maximum enhancement will occur when both the incident Raman beam and the Raman scattering signals are close to the LSPR resonance wavelength (λ_{LSPR}). Studies done in this field suggest that the highest enhancement will be observed when the LSPR band is positioned between the Raman excitation wavelength and the Raman shift of the molecule of interest.[13,31] A more detailed description of the enhancement factor and the experimental method to estimate the values in complex nanostructures will be described in Chapter 5.

The electromagnetic mechanism explains most of the enhancement of SERS but some observations cannot be explained by this theory, suggesting there are other factors. Three examples of this inconsistency are: (i) the difference within the SERS spectrum of a molecule and its normal Raman spectrum, (ii) the inconsistent enhancement factor obtained when different kinds of molecules have been studied under the same experimental conditions, and finally (iii) the discrimination in the enhancement of the different bands in a SERS spectrum. Such observations can be better apprehended by the chemical/electronic mechanism.[26,32]

1.3.1.2. Chemical Mechanism of SERS

The chemical mechanism considers the effect of the molecule adsorbed on the surface of the metallic nanostructure and its electronic interaction with the metal.[32 33] Contrary to the EM mechanism, herein the changes in the SERS spectra come from a combination of contributions that involve the charge-transfer (CT), the resonance Raman (RR), and the molecular orientation and surface selection rules.

The first contribution considers that molecules are strongly adsorbed by the metallic cluster, generating an adsorbate-surface complex. This complex then produces a charge-transfer mode with a larger Raman cross section than the one from the original Raman signal of the adsorbate.[1,27] This effect is illustrated in **Figure 1.8.a**, where the original energetic difference of the HOMO and LUMO of the adsorbate is too high to be excited with a convenient laser (dashed arrow line) while the HOMO and LUMO of the metal are at the same energy Fermi level (E_f). The formation of the complex allows a charge-transfer interaction, reducing the energetic distance between bands and increasing the probabilities of the excitation. In other words, the cross section of the scattered light is enhanced by this new complex.[1,27] The CT contribution is the most controversial,[30,33] and most of the time the enhancement is related to a second factor, the resonance Raman contribution.

As it was described above, resonance Raman scattering can increase the intensity of the Raman signals, when the incident Raman beam matches or is close to an allowed electronic transition of the studied molecules. Herein, the presence of the metallic structure alters the excitation energies of the molecule **Figure 1.8.b**, and leads to the formation of surface enhanced resonance Raman scattering (SERRS).[27,30,33] Finally, the molecular orientation and surface selection rules are responsible of the for the of shift in frequency and intensity of the Raman spectrum.[30,33]

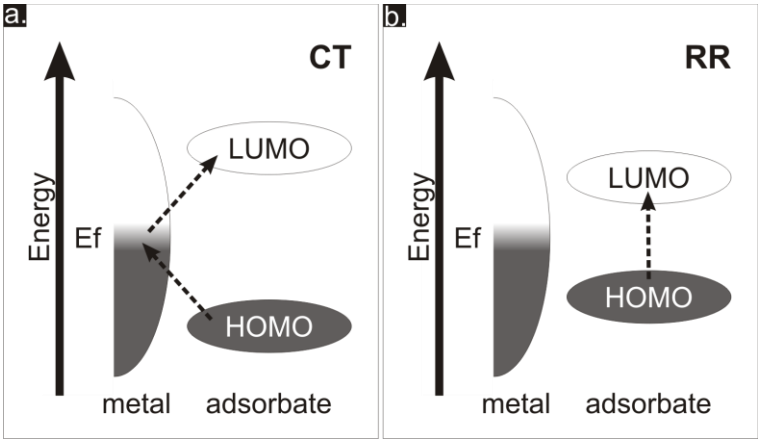

Figure 1.8. Brief illustration of the chemical mechanism contributions: charge transfer (a) and resonance Raman (b).

Since the optical enhancement in SERS is plasmon driven, it can be applied to all molecular systems, i.e. SERS is not molecule specific, which can be confirmed in the compilation of molecules displaying SERS signal and the database available.[34] Notably, the plasmonic enhancement has been confirmed even for molecules with very low scattering cross section such as water[35] and alkanes. However, the challenge of producing reliable, reproducible SERS substrates with an expected enhancement factor remains for the nanostructure fabrication, which would allow one to routinely apply the capabilities of SERS as an analytical tool. The attained electromagnetic enhancement factor (EF), at a given excitation frequency, depends on the dielectric function of the metal nanoparticles, their architecture, size and packing of nanostructures. It is also affected by the dielectric constant of the surrounding medium that wraps the metallic nanostructures. In many cases, the spectral properties of the species adsorbed onto the metal nanoparticles may change on account of the chemical or physical interactions with the nanostructure, and, correspondingly, the electromagnetically enhanced SERS spectrum will contain the information that shed light on these molecule-nanostructure interactions.

The scope of this project is mainly to focus on the electromagnetic field enhancement. However, the theory behind chemical mechanism provides a better understanding of the phenomenon and suggests important factors to consider in the fabrication of a SERS sensor.

1.4. Fabrication of SERS Substrates – General Considerations

One of the first considerations in the fabrication of SERS substrates is the material. As previously described, the dielectric function of the conductor plays an important role in the electromagnetic enhancement mechanism.[1] As described before, noble metals like silver or gold are considered the most appropriate for SERS substrates due to their optical properties in the UV-Visible-NIR region.[13,14] In addition, the chemical and temporal stability, the biocompatibility when used with cells and biomolecules and, reproducibility and feasibility of the preparation are some other important factors in the selection of the best material.[36] From the different metals, gold presents some attractive characteristics: it is the least oxidizable, interacts covalently with some biomolecules (through thiol groups) allowing the adsorbate-metal interaction and it can be deposited over certain surfaces with high reproducibility.

The architecture of the nanostructured surface is an important factor in the fabrication of these substrates. As it was described, the electromagnetic mechanism also involves the size of the features, the interparticle distance and the geometry of the nanostructures in the SERS enhancement. Some experiments suggest that sharp features can increase the enhancement because they behave like antennae, localizing and concentrating the fields, and what is more, larger enhancement occurs when two or more sharp features are close to each other.[36] The first attempts to make SERS substrates, that were based on roughened electrodes or colloidal aggregates, gave very little control over the arrangement at the nanoscale of the metallic particles or size distribution.[37] In recent years, nanofabrication techniques have emerged as a suite of valuable tools to design and prepare a variety of

substrates with distinct shapes, and more importantly with high reproducibility and few defects, opening the door to the manufacture of reliable SERS platforms.

Recent developments in the fabrication of designed-SERS-substrates can be classified as modified surfaces, non-nanosphere-based substrates and lithographic techniques. (i) A substrate can be functionalized to control the position of metallic nanoparticles or colloids, where the concentration and size of the particles will determine the architecture of the substrate and the SERS effect.[37-39] (ii) Nanorods[40] and three-dimensional crescent-shaped nanoparticle substrates have also been prepared, employing a template with size control and used in colloidal solutions.[37,41,42] (iii) Lithography represents one of the most obvious techniques to control the nanoparticle geometry of the SERS substrates. Approaches in this area to simplify the production and reduce the costs of 2D SERS substrates have been made using nanosphere lithography (NSL), though with poor reproducibility.[43] In contrast, electron beam lithography (EBL) allows the full control of the design of different features with a high reproducibility and excellent resolution, around 4 nm.[43] In addition, other lithographic methods,[44] and reactive ion etching (RIE) have also been use in the fabrication of plasmonic substrates.[45-47]

1.5. Scope of Thesis

One of the areas of interest in our group is the creation of SERS platforms that can be integrated in a microfluidic device and used in the development of optical biosensors. In this context, this dissertation is organized around three main themes:

(i) To design and fabricate metallic nanostructures organized in a two dimensional array by electron beam lithography that can be used to perform Raman experiments. These platforms have to meet several criteria: they must be transparent so that they can be used under a confocal microscope in transmission mode. The metallic surface must be biocompatible, as they will be use in the study of biological systems. Their optical

properties must be optimized to enhance the Raman signals of the adsorbed molecules. Chapter 2 will develop the design and fabrication process in detail.

(ii) To characterize the fabricated SERS platforms. This is an important step to determine their plasmonic properties and to select the optimal SERS device. Chapter 3-5 will focus on this characterization using modeling tools to better estimate the electromagnetic field in the vicinity of complex structures. Chapter 3 will focus on the numerical study, using the finite-difference time domain method, of the LSPR properties of these nanostructures, including the estimation of the extinction spectra and the electric field distribution around the nanostructures. Then, Chapter 4 will describe an experimental method to detect the electromagnetic field distribution in the optical near-field around the sample. Furthermore, Chapter 5 will correlate these optical properties with the intensity of the Raman signals, by determining the electromagnetic enhancement factor, and the selection of the optimal SERS platform.

(iii) To incorporate these platforms in a micro-total analysis system that opens the door to the fabrication of integrated biosensors. This last point concerns the applications of the fabricated SERS platforms in the study of bio-systems and the design of a microfluidic device that can be used in SERS experiments. Chapter 6 describes the surface functionalization of the SERS platforms to create a self-assembled monolayer system that can be use as a bio-molecular receptor based on the streptavidin-biotin molecular system. Finally, this chapter also shows the integration of the fabricated SERS platforms in a microfluidic device and the use of such device in the detection of some food toxins by using self-assembled monolayer aptamers.

1.6. References

(1) Kneipp, K.; Kneipp, H.; Itzkan, I.; Dasari, R. R.; Feld, M. S.; *J. Phys.: Condens. Matter*, **(2002)**, *14*, R597.

(2) Schmitt, M.; Popp, J.; *J. Raman Spectrosc.,* **(2006)**, *37*, 20.

(3) Notingher, I.; *Sensors,* **(2007)**, *7*, 1343.

(4) Petry, R.; Schmitt, M.; Popp, J.; *ChemPhysChem,* **(2003)**, *4*, 14.

(5) Jehlicka, J.; Edwards, H. G. M.; Vítek, P.; *Planetary and Space Science,* **(2009)**, *57*, 606.

(6) Bonifas, A. P.; McCreery, R. L.; *Chem. Mater.,* **(2008)**, *20*, 3849.

(7) Lefèvre, T.; Paquet-Mercier, F.; Lesage, S.; Rousseau, M.-E.; Bédard, S.; Pézolet, M.; *Vib. Spectrosc.* , **(2009)**, *51*, 136.

(8) Martel, A.; Burghammer, M.; Davies, R. J.; Di Cola, E.; Vendrely, C.; Riekel, C.; *J. Am. Chem. Soc.,* **(2008)**, *130*, 17070.

(9) Matthew, V. S.; Jacqueline, H. C.; Kathryn, A. D.; Michael, D. M.; Jaclynn, M. K.; Steven, A. G.; Subhadra, S.; Brian, W. P.; *Journal of Biomedical Optics,* **(2008)**, *13*, 020506.

(10) Freudiger, C. W.; Min, W.; Saar, B. G.; Lu, S.; Holtom, G. R.; He, C.; Tsai, J. C.; Kang, J. X.; Xie, X. S.; *Science,* **(2008)**, *322*, 1857.

(11) Pettinger, B.; Picardi, G.; Schuster, R.; Ertl, G.; *Single Molecules,* **(2002)**, *3*, 285.

(12) Mayer, K. M.; Hafner, J. H.; *Chem. Rev.,* **(2011)**, *111*, 3828.

(13) Willets, K. A.; Van Duyne, R. P.; *Annu. Rev. Phys. Chem.,* **(2007)**, *58*, 267.

(14) Banholzer, M. J.; Millstone, J. E.; Qin, L. D.; Mirkin, C. A.; *Chem. Soc. Rev.,* **(2008)**, *37*, 885.

(15) Ebbesen, T. W.; Genet, C.; Bozhevolnyi, S. I.; *Physics Today,* **(2008)**, *61*, 44.

(16) Hohenau, A.; Leitner, A.; Aussenegg, F. R. Near-field and far-field properties of nanoparticle arrays. In *Surface Plasmon Nanophotonics*; Brongersma, M. L., Kik, P. G., Eds.; SPRINGER: BERLIN, 2007; Vol. 131/2007; pp 11.

(17) Wurtz, G. A.; Pollard, R. J.; Zayats, A. Z. Optics of Metallic Nanostructures. In *Handbook of Nanoscale Optics and Electronics*; Wiederrecht, G. P., Ed.; Elsevier B.V.: Amsterdam, 2010; pp 1.

(18) Konstantatos, G.; Sargent, E. H.; *Nat. Nanotechnol.,* **(2010)**, *5*, 391.

(19) Moskovits, M.; *J. Raman Spectrosc.,* **(2005)**, *36*, 485.

(20) Moskovits, M.; Tay, L. L.; Yang, J.; Haslett, T. SERS and the single molecule. In *Optical properties of Nanostructured Random Media*; Shalaev, V. M., Ed.; Springer: Berlin, 2002; pp 215.

(21) Fleischmann, M.; Hendra, P. J.; McQuillan, A. J.; *Chem. Phys. Lett.,* **(1974)**, *26*, 163.

(22) Albrecht, M. G.; Creighton, J. A.; *J. Am. Chem. Soc.,* **(1977)**, *99*, 5215.

(23) Jeanmaire, D. L.; Duyne, R. P. V.; *J. Electroanal. Chem.,* **(1977)**, *84*, 1.

(24) Kneipp, K.; Wang, Y.; Kneipp, H.; Perelman, L. T.; Itzkan, I.; Dasari, R.; Feld, M. S.; *Phys. Rev. Lett.,* **(1997)**, *78*, 1667.

(25) Emory, S. R.; Haskins, W. E.; Nie, S.; *J. Am. Chem. Soc.,* **(1998)**, *120*, 8009.

(26) Campion, A.; Kambhampati, P.; *Chem. Soc. Rev.,* **(1998)**, *27*, 241.

(27) Kambhampati, P.; Child, C. M.; Foster, M. C.; Campion, A.; *J. Chem. Phys.,* **(1998)**, *108*, 5013.

(28) Barnes, W. L.; Dereux, A.; Ebbesen, T. W.; *Nature,* **(2003)**, *424*, 824.

(29) Kosuda, K. M.; Bingham, J. M.; Wustholz, K. L.; Van Duyne, R. P. Nanostructures and Surface-Enhanced Raman Spectroscopy. In *Handbook of Nanoscale Optics and Electronics*; First ed.; Wiederrecht, G., Ed.; Elsevier B.V.: Amsterdam, 2010; pp 309.

(30) Morton, S. M.; Silverstein, D. W.; Jensen, L.; *Chem. Rev.,* **(2011)**, *111*, 3962.

(31) McFarland, A. D.; Young, M. A.; Dieringer, J. A.; Van Duyne, R. P.; *J. Phys. Chem. B,* **(2005)**, *109*, 11279.

(32) Hering, K.; Cialla, D.; Ackermann, K.; Dorfer, T.; Moller, R.; Schneidewind, H.; Mattheis, R.; Fritzsche, W.; Rosch, P.; Popp, J.; *Anal. Bioanal. Chem.,* **(2008)**, *390*, 113.

(33) Jensen, L.; Aikens, C. M.; Shatz, G. C.; *Chem. Soc. Rev.,* **(2008)**, *37*, 1061.

(34) www.spectroscopynow.com.

(35) Chen, Y.-X.; Otto, A.; *J. Raman Spectrosc.,* **(2005)**, *36*, 736.

(36) Chan, G. H.; Zhao, J.; Hicks, E. M.; Schatz, G. C.; Duyne, R. P. V.; *Nano Lett.,* **(2007)**, *7*, 1947.

(37) Lee, S. J.; Morrill, A. R.; Moskovits, M.; *J. Am. Chem. Soc.,* **(2006)**, *128*, 2200.

(38) Choi, D.; Choi, Y.; Hong, S.; Kang, T.; Lee, L. P.; *Small,* **(2010)**, *6*, 1741.

(39) Gibson, K. F.; Correia-Ledo, D.; Couture, M.; Graham, D.; Masson, J.-F.; *Chem. Comm.,* **(2011)**, *47*, 3404.

(40) Lu, Y.; Liu, G. L.; Kim, J.; Mejia, Y.; Lee, L. P.; *Nano Lett.,* **(2005)**, *5*, 119.

(41) Hulteen, J. C.; Treichel, D. A.; Smith, M. T.; Duval, M. L.; Jensen, T. R.; Van Duyne, R. P.; *J. Phys. Chem. B,* **(1999)**, *103*, 3854.

(42) Rodriguez-Lorenzo, L.; Alvarez-Puebla, R. A.; Garcia de Abajo, F. J.; Liz-Marzan, L. M.; *J. Phys. Chem. C,* **(2010)**, *114*, 7336.

(43) Cui, B.; Clime, L.; Li, K.; Veres, T.; *Nanotechnology,* **(2008)**, *19*, 145302.

(44) Wu, W.; Hu, M.; Ou, F. S.; Li, Z.; Williams, R. S.; *Nanotechnology,* **(2010)**, *21*, 255502.

(45) Marquestaut, N.; Martin, A.; Talaga, D.; Servant, L.; Ravaine, S.; Reculusa, S.; Bassani, D. M.; Gillies, E.; Lagugne-Labarthet, F.; *Langmuir,* **(2008)**, *24*, 11313.

(46) Aksu, S.; Yanik, A. A.; Adato, R.; Artar, A.; Huang, M.; Altug, H.; *Nano Lett.,* **(2010)**, *10*, 2511.

(47) http://www.renishawdiagnostics.com/en/klarite-sers-detection-substrates--12515.

Chapter 2: Design, Fabrication and Characterization of Plasmonic Nanostructures℘

2.1. Introduction

The modification of the optical properties of metallic structures at the nanoscale level is a topic or interest in the development of new molecular sensors.[1,2] Changes in the materials,[3,4] in the architecture of the structured surface,[3-5] in the size,[5] and in the interparticle distance between nanosize features[3,5] are some of the factors responsible for the modification of the localized surface plasmon resonance (LSPR) properties. In metallic nanostructures, a large enhancement of the electromagnetic field around the metallic surface can be observed when the frequency of the conduction electrons in the metal matches the frequency of the incident photons.[6] This particular case constitutes the basis of different surface-enhanced spectroscopy techniques, such as surface-enhanced Raman scattering (SERS),[1,2,7-9] tip enhanced Raman scattering (TERS),[10,11] or surface-enhanced infrared absorption (SEIRA).[12-15] Current research projects in these fields are focused on the rational fabrication of highly sensitive, tunable, and reproducible platforms that can be applied for the detection of trace chemicals,[2,16-19] for a broad spectrum of analytical applications.[20-27]

This chapter will focus in the fabrication of nanostructured platforms prepared by electron beam lithography as well as on the methodology used for the physical and optical characterization of such devices. At the end of the chapter the reader will have precise details to prepare arrays of metallic plasmonic nanostructures inscribed onto a glass surface allowing one to perform transmission measurements. The high degree of

---

℘ Part of this Chapter has been published in [*Phys. Chem. Chem. Phys.*, **(2010)**, *12*, 6810.]. Reproduced by permission of the PCCP Owner Societies

tunability of such metallic nanostructures will be demonstrated, opening their application to a large spectral range.

2.2. Current fabrication methods of two-dimensional nanostructures

Different research groups have designed, fabricated and characterized nanostructured surfaces using various techniques, such as immobilized colloid deposition,[28] nanoimprint lithography,[1] chemical etching,[29] on-wire lithography,[30] and many others.[16,17,31-33] Among these nanofabrication techniques, lithography represents one of the most simple methods to control the geometry, size and spacing of the nanoparticles.[17] In order to simplify and reduce the costs of production, substrates have been made using nanosphere lithography (NSL),[17] although there are certain design limitations associated with this technique.

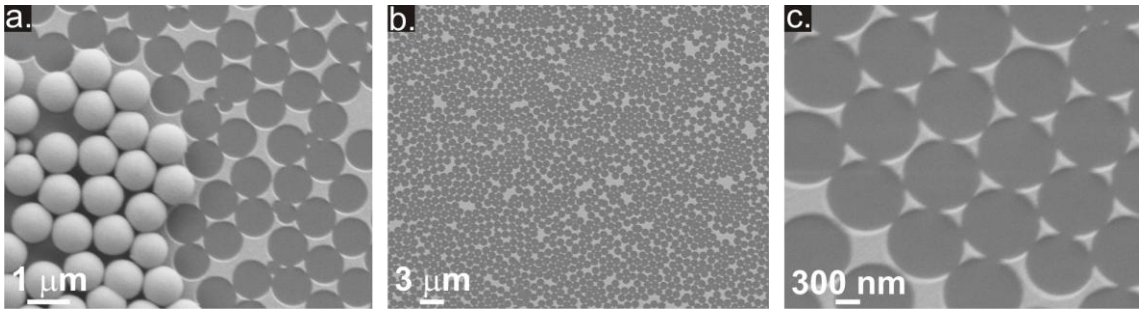

Figure 2.1. NSL and surface patterns made with 470 nm beads (a) and without beads (b and c) coated with 40 nm gold over a glass substrate.

NSL uses a monolayer of nanospheres deposited on a substrate by spin coating,[16] drop-coating,[34] or Langmuir-Blodgett transfer.[32] Then, a thin layer of a noble metal is deposited on top of the sample filling the voids between the spheres and getting transferred onto the substrate surface. Finally, after removing the layer of spheres by

sonication, the substrate is decorated with the nanoscale remains of the metallic patterns composed of bowties assemblies and defects associated with the deposition method.[17] This technique can pattern a larger area with a lower cost, but it is less reproducible and results in significant defects after cleaning the spheres/beads, as shown in **Figure 2.1**.

In contrast, electron beam lithography (EBL) allows full control over the design of different features with a high reproducibility and excellent resolution.[1] However, the features fabricated herein are commonly outside the nanometric scale (> 100 nm).EBL requires first a substrate coated with an electron beam photosensitive polymer, referred generally as a photoresist. Using a scanning electron microscope equipped with a lithographic system, a design can be written on the surface by exposing the photoresist with the electron beam. Then, in the case of a positive photoresist, the coated sample has to be cleaned to remove the exposed polymer and to reveal the developed photoresist stencil mask, which can be used for metal deposition. Finally, after removing the remaining photoresist, the substrate will be decorated with the metallic design. Some patterns made in our group using this technique are shown in **Figure 2.2**, where it can be appreciated that EBL offers a high control of the size, shape and spacing of the features.[16]

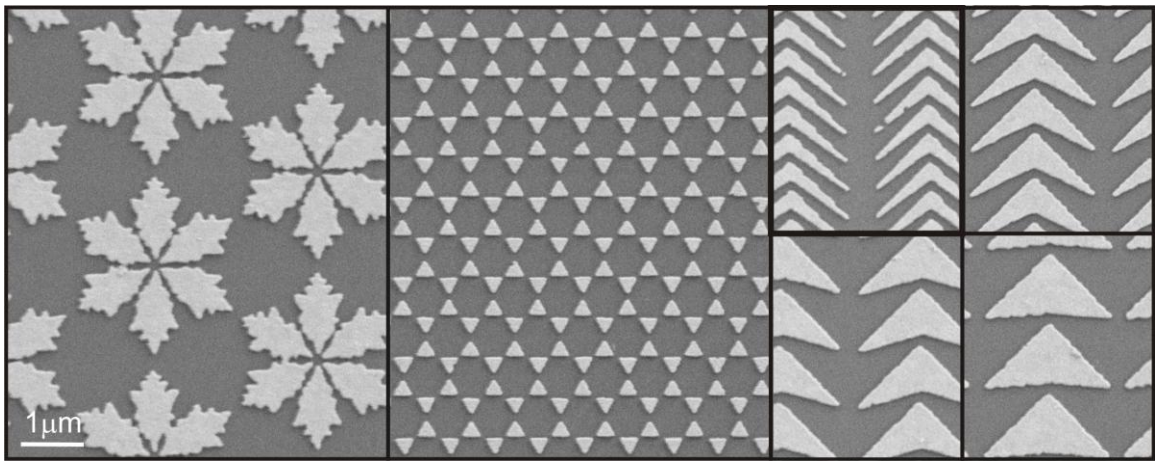

Figure 2.2. Scanning electron micrographs of 2-D nanostructures written using EBL.

2.3. Plasmonic properties of metallic nanostructures

As it was described in Chapter 1, the characterization of the optical properties of metallic nanoparticles, and consequently the determination of the LSPR frequency in the far-field, can be performed by the study of their extinction, scattering or absorption spectra.[9,35] Experimentally this detection can be accomplished by the use of a spectrometer in transmission (**Figure 2.3.a**),[9] or in reflection (**Figure 2.3.b**)[36] mode. In addition, the LSPR scattering of small samples or isolated nanostructures can also be detected by employing dark-field scattering microscope (**Figure 2.3.c**).[37]

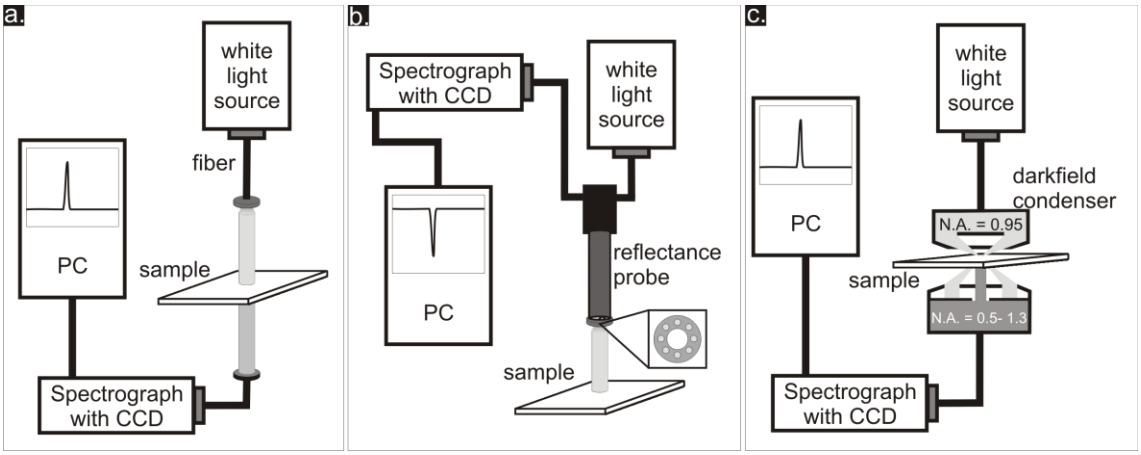

Figure 2.3. Transmission (a), reflection (b), and dark field (c) systems used to detect the LSPR properties in far-field.

The use of a spectrometer in transmission mode can collect the extinction (extinction: absorption plus scattering) spectra of transparent samples; and in the case of non-transparent samples, a change in the setup must be done to detect the reflectance of the sample. While in the first case the LSPR bands appear as a maximum signal, in the case of reflectance the LSPR modes will have a minimum value. In the case of the dark field system, a white light source irradiates the sample with a high angle and the scattering spectrum can be collected at a lower angle with the use of a dark field condenser.[37]

The signals obtained from the spectrum, can then be interpreted as the different localized surface plasmon resonance modes from the structure.[7] These plasmonic modes can be calculated accurately in the case of spherical nanostructures by using Mie's theory, as it was illustrated in Chapter 1 for the detection of the cross section spectra for a gold nanosphere, and that explains the red color of similar colloidal solutions. However, in reality, as the size of the particles increase and the geometry changes, the LSPR spectrum can present multiple bands, as a result of the different LSPR modes. Qualitatively, the first LSPR mode ($l = 1$) in nanoparticles, or simply called dipole mode, is described as the collective oscillation of the electron cloud in the particle that is in-phase with the electromagnetic wave (**Figure 2.4.a**). This is the mode usually described in the literature to explain LSPRs, and tends to be the most intense. On the other hand, the quadrupole mode ($l = 2$) represents the oscillation in-phase of half of the conduction electrons to the plasmonic frequency (**Figure 2.4.b**), and higher modes will represent other distributions of the electron cloud (**Figure 2.4.c**).[4,38]

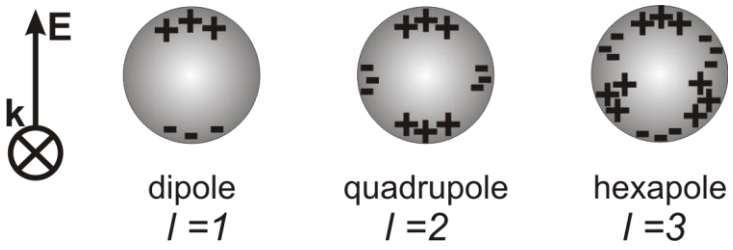

Figure 2.4. Schematic representation of different LSPR multipoles of a metallic nanosphere.

Mathematically, the different plasmon modes can be determined by analyzing the efficiency ($Q = \sigma/(\pi r^2)$) related to the cross section (σ) parameter of a nanosphere of radius r. Thus, by solving Mie theory the efficiency values for the extinction and

scattering cross section of a nanoparticle with a dipole mode will be described by **(1), (2),** and **(3).**[4,39-41]

$$Q_{ext} = 4xIm(g_d) \quad \textbf{(1)}$$

$$Q_{sca} = \frac{8}{3}x^4|g_d|^2 \quad \textbf{(2)}$$

$$x = \frac{2\pi r(\varepsilon_d)^{1/2}}{\lambda} \quad \textbf{(3)}$$

The factor g_L, shown in **(4)**, is responsible for the wavelength dependence of the LSPR mode, as it describes the ratio between the dielectric functions of the metal (ε_m) and the dielectric (ε_d). In addition, this factor also makes a distinction between the different plasmon modes studied, L in **(5)**. Thus in the case of a dipole mode ($l = 1$) the spectrum will show a maximum interaction when $\varepsilon_m = -2\varepsilon_d$.

$$g_L = \frac{\varepsilon_m + \varepsilon_d}{\varepsilon_m + L\varepsilon_d} \quad \textbf{(4)}$$

$$L = \frac{(l+1)}{l} \quad \textbf{(5)}$$

For those spheres that present a dipole (L = 2) and quadrupole mode (L = 3/2) in their cross section spectra, the description of their extinction and scattering efficiency values becomes more complex, as shown in **(6)** and **(7)**.

$$Q_{ext} = 4xIm\left[g_{L=2} + \frac{x^2}{12}g_{L=3/2} + \frac{x^2}{30}(\varepsilon_m - 1)\right] \quad \textbf{(6)}$$

$$Q_{sca} = \frac{8}{3}x^4\left[|g_{L=2}|^2 + \frac{x^4}{240}\left|g_{L=3/2}\right|^2 + \frac{x^4}{900}|\varepsilon_m + 1|^2\right] \quad \textbf{(7)}$$

Based on the aforementioned equations, it is possible to assume that more complex mathematical expressions will be required for bigger nanostructures. Moreover, non-spherical nanostructures present a non-isotropic electron cloud distribution, which often

leads to the detection of other plasmon modes in the spectra, that are strongly dependent on the size, the geometry, the dielectric environment and the polarization of the incoming beam.[3,4,42,43] Rigurous solutions of Maxwell's equations are known only for spheres, spheroids and infinite cylinders. For arbitrary shapes the solutions are found by more complex approximation methods, based on electrodynamic calculations, are necessary to better understand the LSPR effect in more complex structures.[4,43,44] A more detailed description of the some of the current numerical approximations used to detect the plasmon modes is given in Chapter 3.

The complexity of the localized surface plasmon resonance behavior in non-spherical nanostructures can be illustrated by the study reported in the literature for triangular nanoparticles.[4] Herein, the authors describe the interaction of the electromagnetic field with a single isolated silver nanotriangle (100 nm edge length, and 16 nm thick) by using a method known as the discrete dipole approximation (DDA). The results show that the extinction spectrum of this structure gets altered by changing the polarization of the input light (**Figure 2.5.a**). Thus, two plasmon modes are calculated in the visible range when the polarization is parallel to the X and Y axis, one at 770 nm and a second one at 460 nm, and they represent the signals for the in-plane components. The charge distribution of the different modes was also modeled and it was possible to assign the signals to the different modes. A dipole mode is observed when the sample is irradiated at 770 nm (**Figure 2.5.b, left**), while the plasmon resonance at 440 nm correspond to the quadrupole mode (**Figure 2.5.b, right**). In addition, the electric field distribution was also calculated for these two bands and the results show the position of the hot-spots, or the areas where the electric field reaches its maximum value, and how these regions will be localized at the apexes of the triangle when in resonance at the dipole mode (**Figure 2.5.c, left**), and on the sides when irradiated at the quadrupole mode resonance wavelength (**Figure 2.5.c, right**).[4]

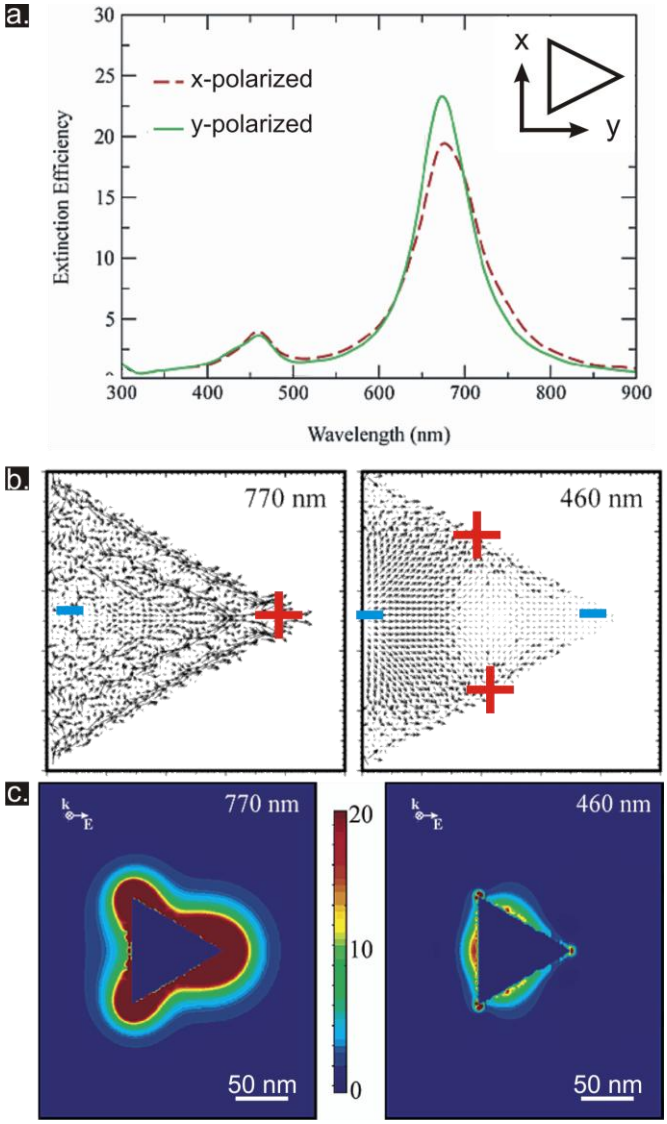

Figure 2.5. DDA calculation of the plasmonic properties of a silver nanotriangles.[4,43]

2.4. Design of hexagonal array of nanotriangles

From the multiple designs that can be made to excite the localized surface plasmon resonance of metals in the visible range, hexagonal arrays of nanotriangles, also known as Fischer's patterns,[45] were the ones selected for this project. These arrays, traditionally made by nanosphere lithography,[17] are broadly used in the fabrication of SERS sensors, however in this project the selected fabrication method used to prepare such designs was electron beam lithography (**Figure 2.6**). As it was explained earlier, EBL allows a full

control and reproducibility of the design which is an important prerequisite to have a clear cut understanding of the plasmonic properties of this common design. EBL allows one to reduce the variables that fabrication defects can generate.

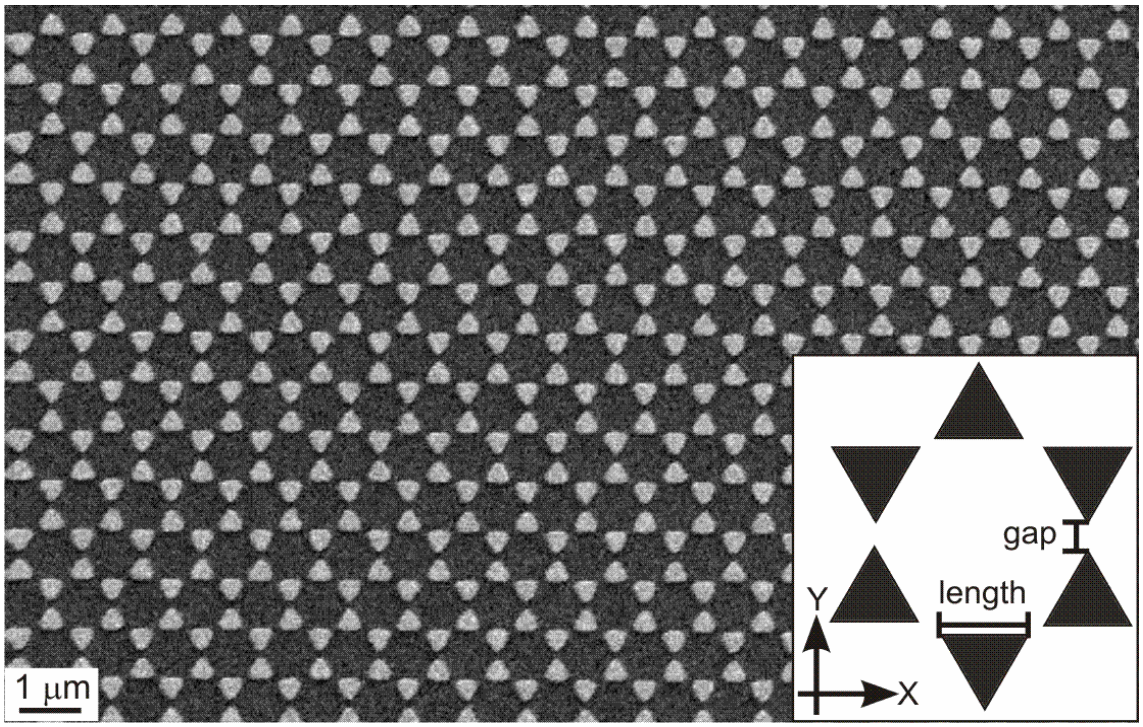

Figure 2.6. SEM image of hexagonal array of nanotriangles fabricated by EBL.

In addition, studies suggest that sharp corners that are close to each other generate a large field enhancement,[23,46,47] therefore, the study of the bow tie interaction in these hexagonal array of nanotriangles and other possible coupling between nanostructures is of interest. Furthermore, as stated in the case of isolated triangles the effect of the input polarization can affect the plasmon bands. Fischer's patterns present a C6 axis symmetry and the effect of the input polarizability has not been considered in the literature.

With these considerations, this chapter will focus on the fabrication of Fischer's patterns. This fabrication method will be used in all the studies done in this thesis, and the following chapter will refer to the description given here. Second, a full description of the physical and optical characterization of the arrays will be given, and finally a polarization study of the arrays will be described and later compared with numerical calculations, in Chapter 3.

2.5. Experimental methods

2.5.1. Fabrication

Samples were fabricated by EBL on VistaVision^{TM} microscope cover glass slides, which were obtained from VWR-Canada. The substrate is therefore transparent in the visible spectral range. First, the slides were cleaned in Nano-strip (Cyantek Inc.) solution and spin-coated with a 500 nm layer of ZEP520A photoresist (Nippon ZEON Ltd.) diluted 1:4 in methylisobutyl ketone. Generally, to inscribe the pattern with EBL, it is essential to have an electrical conductor on the sample surface. To achieve this, a 20 nm chromium layer was deposited over the photoresist thin film using a magnetron sputtering tool (Edwards Auto500). An electron beam system (LEO 1530 Field Emission) was used to write the Fischer's patterns at an accelerating voltage of 30 keV, a current around 30 pA and a nominal area dose of 100 $\mu C/cm^2$. Changing the area dose made it possible to modify the resolution of the exposed patterns, resulting in a better control of the size of the triangles as well as the size of the gaps between triangles. A 4 x 4 array was designed by assigning different area dose exposure, ranging from 70% to 145% of the nominal value. The incremental change of dose was of 5% for each pattern. After exposure, the sample was immersed in chromium etchant solution 1020 (Transene Company Inc.) for 10-15 seconds and rinsed with de-ionized water. The samples were then developed in ZED N50 (Zeon Chemicals L.P.), rinsed in methylisobutyl ketone diluted 1:3 in isopropyl alcohol, dipped in isopropyl alcohol, and gently dried. After the developing process, a 40 nm gold film was deposited on top of the revealed stencil resist film using an e-beam evaporation system (DOC) at a rate of 1Å/s. Finally, the sample was treated in a deep

ultraviolet radiation chamber and immersed in acetone for the lift-off step that consists in removing the remnant photoresist. A summary of the process is illustrated in **Figure 2.7**.

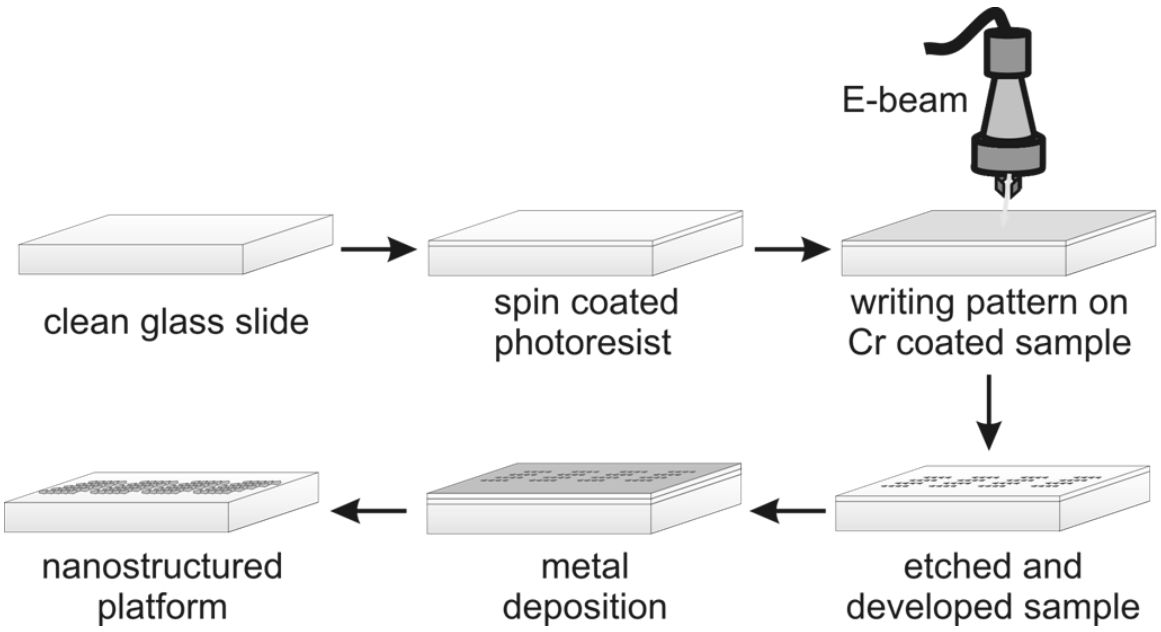

Figure 2.7. Fabrication process of nanostructured platforms fabricated by EBL.

2.5.2. Physical characterization

Atomic Force Microscope (AFM) images were collected primarily on a Nanowizard II (JPK instruments). Alternatively a Veeco Bioscope II was also used. Both contact mode using a NP-S20 cantilever (k=0.06 N/m, Veeco Instuments Inc.) or tapping mode using a NCL-20 cantilever (k=39 N/m, PointProbe®) were used to image the structures. Electronic images were acquired using a SEM (LEO 1530 Field Emission) with a 1.5-3 keV field-emission electron source.

2.5.3. Extinction spectra

The LSPR peaks of the samples were determined from the extinction spectra using a spectrometer coupled with a 100 µm optical fiber to an Olympus IX71 inverted optical microscope. The microscope was equipped with a 10x (NA =0.25) objective. The light source is a halogen lamp that is coupled to a 100 µm optical fiber that illuminates the sample with a collimated beam. The collimation system consisted of a 10x (NA = 0.25) objective to expand the source beam and a 20x (NA = 0.25) objective to collimate the beam on the sample with a spot size of about 60 microns, which is slightly smaller than the size of the platforms. After the sample, the transmitted light was finally collected by a third microscope objective prior to analysis by the spectrometer in the 400-800 nm spectra range. Typically, each spectrum is the result of 30 accumulations. In the case of the experiments conducted under a linearly polarized light source, a polarizer was placed between the 10x and 20x objectives, as shown in **Figure 2.8**.

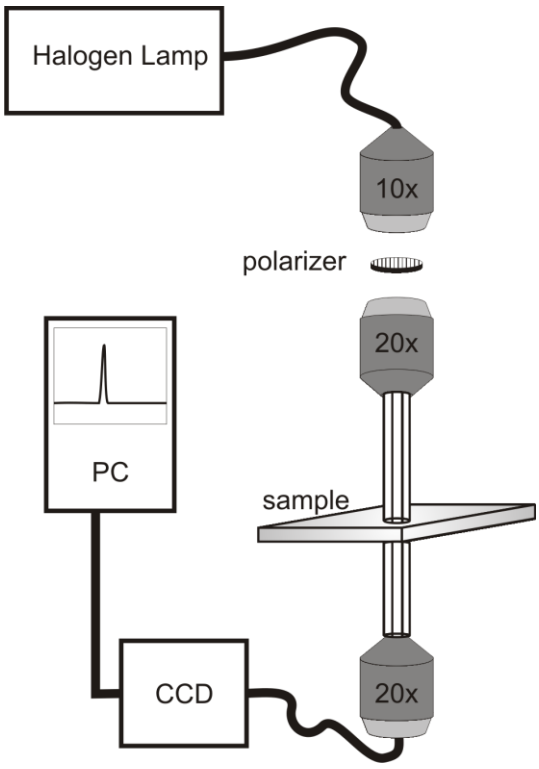

Figure 2.8. Scheme of the extinction measurement setup.

2.6. Results and discussion

2.6.1. Optical properties of a series of Fischer's patterns

The scanning electron micrographs of an array of Fischer's pattern fabricated at different area doses (70-145 μC/cm^2), and of one the patterns fabricated with the nominal area dose are shown on **Figure 2.9**.

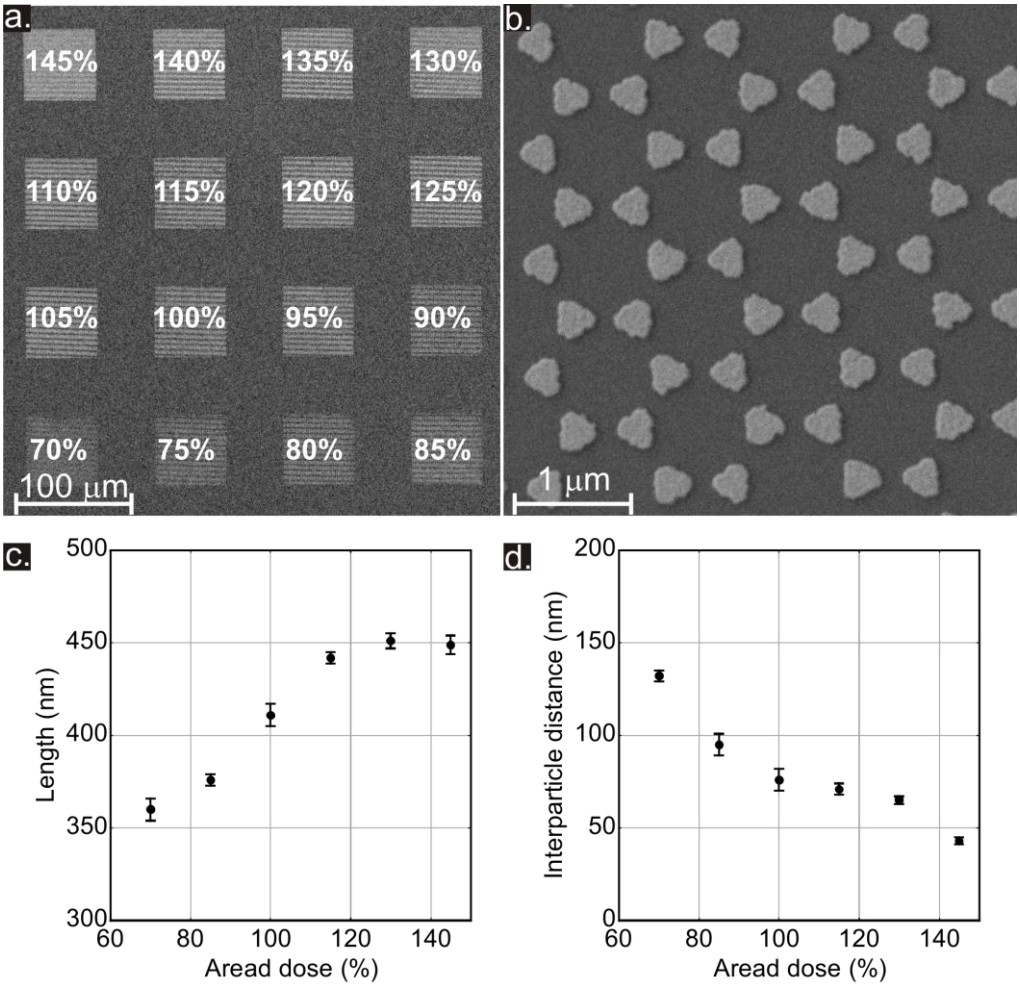

Figure 2.9. SEM image of a Fischer's pattern array (a) and of an array fabricated with a dose of 100 μC/cm^2 (b). Effect of the area dose exposure on the length size (c) and gap distance (d) of the individual triangles.

The gold thickness for the individual patterns was 40±4 nm of gold (**Figure 2.10**), and confirmed the calibration of the deposition apparatus. The AFM scans also provide information related to the roughness of the gold surface (Ra = 1.9 nm).

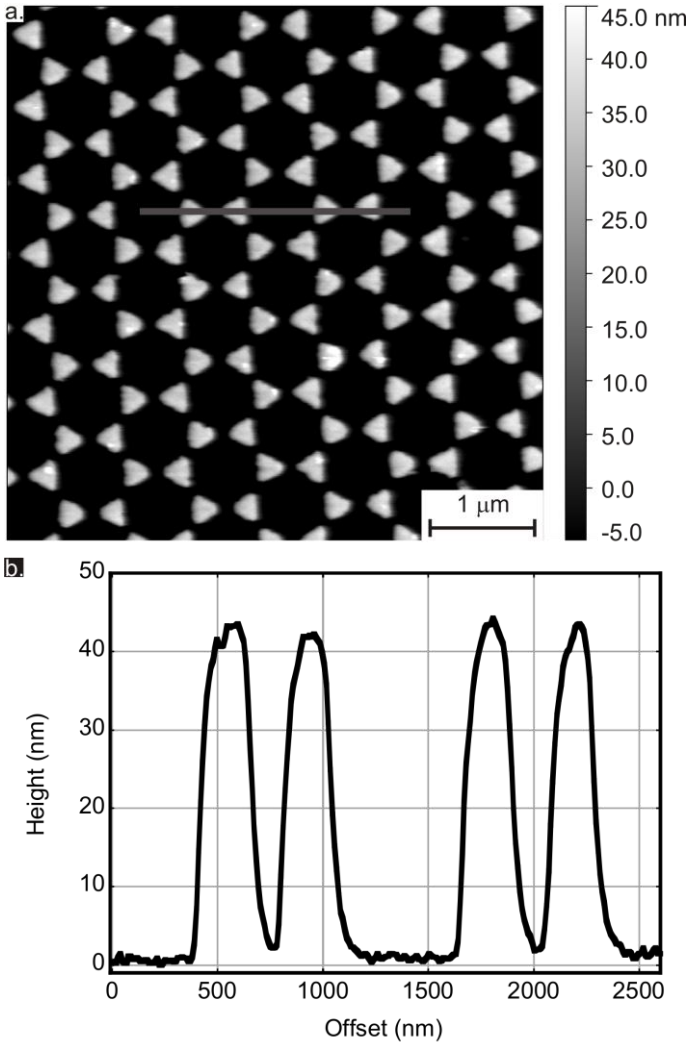

Figure 2.10. Atomic force micrograph of an array of Fischer's pattern made of gold over a microscope coverslip (a), and its cross section image (b).

Additionally, the SEM was used to determine the length size and gap distance of the patterns fabricated at different area dose exposures. SEM measurements were conducted

on six of the sixteen patterns present on the array. The average values with their standard deviation bars can be seen in **Figures 2.9.c, d**. From the plots, it is possible to visualize how an increase in the area dose exposure of the e-beam system increases the length size of the nanotriangles and reduces the gap distance in the pattern. However, in some of the cases, a higher dose exposure also reduces the resolution of the features.

The sixteen individual patterns were analyzed in transmission mode and their extinction spectra were plotted in **Figure 2.11.a**. Two main LSPR peaks (λ_{max}) can be seen in the 550-750 nm region for all the patterns, but it is less perceptible on those patterns fabricated with the lowest area dose exposure. The collection of the different spectra suggests bigger features with smaller gap distances have red-shifted LSPR peaks, in agreement with previous studies.[4,43,48] These physical changes have a stronger effect on the peak around 596 ± 19 nm than on the peak around 726 ± 9 nm, as summarized in **Figure 2.11.b**. As a result, these trends suggest that changing the area dose exposure not only controls the gap and the feature resolution, but also allows one to tune the LSPR peaks.

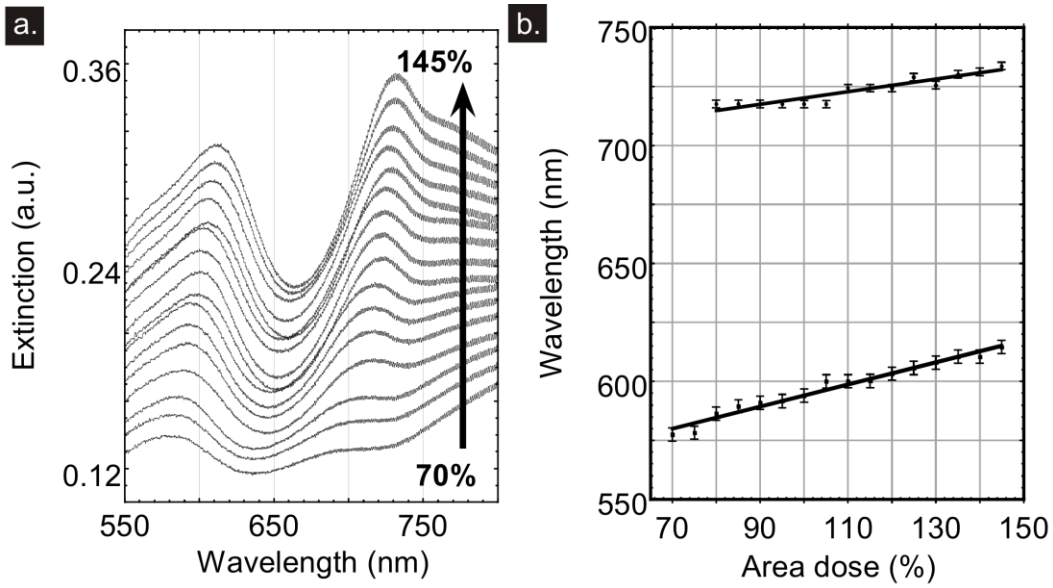

Figure 2.11. Extinction spectra of Fischer's pattern made at different area dose exposure percentage with respect to the nominal area dose -100 μC/cm^2- (a), and summary of the peaks trends (b).

The extinction spectra for small features of gold Fischer's patterns has been reported in the literature,[49,50] and the number of plasmon peaks are in agreement with the present results. The peaks obtained can be compared with some of the LSPR peaks obtained with the study of triangular nanoprisms in solution. The first peak present in the 580-620 nm region has been attributed to multipolar excitations, such as the in-plane quadrupole term.[4,43] In addition, peaks around 750 nm wavelength might be related to the dipole resonance mode detected on 150 nm length and 10 nm gold film triangular nanoprisms in solution.[51,52]

2.6.2. Polarized LSPR spectral contributions

The extinction spectra of one of the arrays of Fischer's patterns (Fischer's pattern-A: 357 nm length size and 184 nm gap distance) was also measured using linearly polarized light. **Figure 2.12** shows the extinction spectra using a non-polarized light source (●), a

linearly polarized source along the X axis (■), and a linearly polarized source along the Y axis (▲) where X and Y are referenced in the inset. The peak around 750 nm, is more sensitive to the polarization of the light and exhibits a larger intensity when the polarization of the source is along the Y axis. Previous studies have reported the effect of the polarization on the extinction spectra of nanotriangles,[4,44,53,54] or bow tie assembly,[44,55,56] but none of the authors have considered this effect when the nanotriangles are in a hexagonal array. The extinction spectra experiments of Fischer's patterns reported in the literature do not consider the polarization conditions.

The spectra for the X and Y polarization suggest similar intensity values at around 582 nm. This implies that this plasmon resonance wavelength of the Fischer's pattern is independent of the polarization of the incoming light. However, in the case of the 680-720 nm region, the LSPR mode is polarization-dependent. This second band must be related to the interaction of the two facing triangles, or bow tie assembly. Thus, when the polarization is parallel to the Y axis, the resonance electric field of triangular dimers couples with each other and generates a stronger LSPR field enhancement, than when the incoming polarization is parallel to the X axis.

To correlate the extinction spectrum of this array with their associated plasmon modes, and to understand the effect of the input polarization, it is necessary to make use of some numerical methods. Chapter 3 will focus on such calculations and will correlate the results obtained for hexagonal array of nanotriangles with the experimental results obtained in Chapter 2.

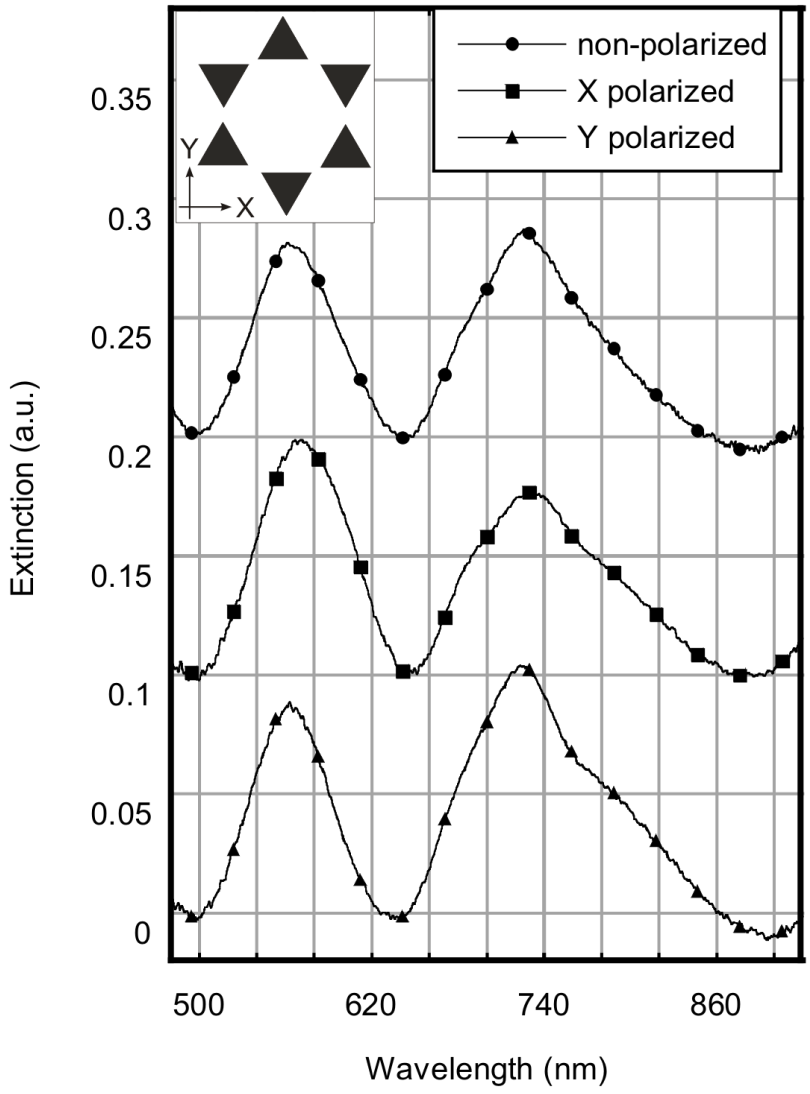

Figure 2.12. Extinction spectra of an array of Fischer's pattern-A (357 nm length size and 184 nm gap distance).

2.7. Conclusions

Metallic Fischer's patterns on glass slides were fabricated using electron beam lithography. By changing the area dose exposure of the electron beam system, it is possible to tailor the size and the gap distance of the nanostructures. Most importantly, it opens up the possibility of tuning very finely the LSPR of this hexagonal array of triangular nanofeatures. In addition, we reported for the first time, that a change in the

polarization of the incoming light on a Fischer's pattern will modify the intensity of some of the plasmon resonances.

In addition, these results suggest that in the case of the Fischer's patterns, the strong electric field enhancement is confined to the pairs of bowtie nanotriangles oriented along the input polarization direction. This type of structure, although widely reported in the literature is therefore not optimal when linearly polarized light is used. This suggests that using a non-polarized light, a scrambler source for instance, would result in a homogeneous enhancement for all the bow tie assemblies, and therefore a higher overall enhancement around the whole structure.

2.8. References

(1) Li, K.; Clime, L.; Cui, B.; Veres, T.; *Nanotechnology,* **(2008)**, *19*, 145305.

(2) Liu, G. L.; Lee, L. P.; *Appl. Phys. Lett.*, **(2005)**, *87*, 074101.

(3) Haynes, C. L.; McFarland, A. D.; Zhao, L.; Van Duyne, R. P.; Schatz, G. C.; Gunnarsson, L.; Prikulis, J.; Kasemo, B.; Kall, M.; *J. Phys. Chem. B,* **(2003)**, *107*, 7337.

(4) Kelly, K. L.; Coronado, E.; Zhao, L. L.; Schatz, G. C.; *J. Phys. Chem. B,* **(2003)**, *107*, 668.

(5) Jensen, T.; Kelly, L.; Lazarides, A.; Schatz, G. C.; *J. Cluster Sci.*, **(1999)**, *10*, 295.

(6) Barnes, W. L.; Dereux, A.; Ebbesen, T. W.; *Nature,* **(2003)**, *424*, 824.

(7) Haes, A. J.; Van Duyne, R. P.; *J. Am. Chem. Soc.*, **(2002)**, *124*, 10596.

(8) Kneipp, K.; Kneipp, H.; Itzkan, I.; Dasari, R. R.; Feld, M. S.; *J. Phys.: Condens. Matter,* **(2002)**, *14*, R597.

(9) Willets, K. A.; Van Duyne, R. P.; *Annu. Rev. Phys. Chem.*, **(2007)**, *58*, 267.

(10) Domke, K. F.; Pettinger, B.; *J. Raman Spectrosc.,* **(2009)**, *40*, 1427.

(11) Hartschuh, A.; Beversluis, M. R.; Bouhelier, A.; Novotny, L.; *Philos. Trans. R. Soc. London, Ser. A,* **(2004)**, *362*, 807.

(12) Aroca, R. F.; Ross, D. J.; *Appl. Spectrosc.*, **(2004)**, *58*, 324A.

(13) Johnson, S. A.; Pham, N. H.; Novick, V. J.; Maroni, V. A.; *Appl. Spectrosc.*, **(1997)**, *51*, 1423.

(14) Levin, C. S.; Kundu, J.; Barhoumi, A.; Halas, N. J.; *Analyst*, **(2009)**, *134*, 1745.

(15) Nakata, K.; Okubo, A.; Shimazu, K.; Yamakata, A.; Ye, S.; Osawa, M.; *Langmuir*, **(2008)**, *24*, 4352.

(16) Banholzer, M. J.; Millstone, J. E.; Qin, L. D.; Mirkin, C. A.; *Chem. Soc. Rev.*, **(2008)**, *37*, 885.

(17) Hulteen, J. C.; Treichel, D. A.; Smith, M. T.; Duval, M. L.; Jensen, T. R.; Van Duyne, R. P.; *J. Phys. Chem. B*, **(1999)**, *103*, 3854.

(18) Le Ru, E. C.; Etchegoin, P. G.; Grand, J.; Félidj, N.; Aubard, J.; Lévi, G.; Hohenau, A.; Krenn, J. R.; *Curr. Appl. Phys.*, **(2008)**, *8*, 467.

(19) Lee, S.; Kim, S.; Choo, J.; Shin, S. Y.; Lee, Y. H.; Choi, H. Y.; Ha, S.; Kang, K.; Ohs, C. H.; *Anal. Chem.*, **(2007)**, *79*, 916.

(20) Abell, J. L.; Driskell, J. D.; Dluhy, R. A.; Tripp, R. A.; Zhao, Y. P.; *Biosens. Bioelectron.*, **(2009)**, *24*, 3663.

(21) Cho, H.; Lee, B.; Liu, G. L.; Agarwal, A.; Lee, L. P.; *Lab Chip*, **(2009)**, *9*, 3360.

(22) Geiman, I.; Leona, M.; Lombardi, J. R.; *J. Forensic Sci.*, **(2009)**, *54*, 947.

(23) Hering, K.; Cialla, D.; Ackermann, K.; Dorfer, T.; Moller, R.; Schneidewind, H.; Mattheis, R.; Fritzsche, W.; Rosch, P.; Popp, J.; *Anal. Bioanal. Chem.*, **(2008)**, *390*, 113.

(24) Lefrant, S.; Baibarac, M.; Baltog, I.; *J. Mater. Chem.*, **(2009)**, *19*, 5690.

(25) MacAskill, A.; Crawford, D.; Graham, D.; Faulds, K.; *Anal. Chem.*, **(2009)**, *81*, 8134.

(26) Wachsmann-Hogiu, S.; Weeks, T.; Huser, T.; *Curr. Opin. Biotechnol.*, **(2009)**, *20*, 63.

(27) Wustholz, K. L.; Brosseau, C. L.; Casadio, F.; Van Duyne, R. P.; *Phys. Chem. Chem. Phys.*, **(2009)**, *11*, 7350.

(28) Wang, H.; Levin, C. S.; Halas, N. J.; *J. Am. Chem. Soc.*, **(2005)**, *127*, 14992.

(29) Cui, B.; Clime, L.; Li, K.; Veres, T.; *Nanotechnology*, **(2008)**, *19*, 145302.

(30) Qin, L.; Zou, S.; Xue, C.; Atkinson, A.; Schatz, G. C.; Mirkin, C. A.; *Proc. Natl. Acad. Sci. U. S. A.*, **(2006)**, *103*, 13300.

(31) Guieu, V.; Lagugné-Labarthet, F.; Servant, L.; Talaga, D.; Sojic, N.; *Small*, **(2008)**, *4*, 96.

(32) Marquestaut, N.; Martin, A.; Talaga, D.; Servant, L.; Ravaine, S.; Reculusa, S.; Bassani, D. M.; Gillies, E.; Lagugné-Labarthet, F.; *Langmuir*, **(2008)**, *24*, 11313.

(33) Bolduc, O. R.; Live, L. S.; Masson, J.-F.; *Talanta*, **(2009)**, *77*, 1680.

(34) Lee, S. J.; MMorrill, A. R.; Moskovits, M.; *J. Am. Chem. Soc.*, **(2006)**, *128*, 2200.

(35) Mayer, K. M.; Hafner, J. H.; *Chem. Rev.*, **(2011)**, *111*, 3828.

(36) Zhang, X.; Young, M. A.; Lyandres, O.; Van Duyne, R. P.; *J. Am. Chem. Soc.*, **(2005)**, *127*, 4484.

(37) Tay, L.-L.; Hulse, J.; Kennedy, D.; Pezacki, J. P.; *J. Phys. Chem. C*, *114*, 7356.

(38) Payne, E. K.; Shuford, K. L.; Park, S.; Schatz, G. C.; Mirkin, C. A.; *J. Phys. Chem. B*, **(2006)**, *110*, 2150.

(39) Aden, A. L.; Kerker, M.; *J. Appl. Phys.*, **(1951)**, *22*, 1242.

(40) Foteinopoulou, S.; Vigneron, J. P.; Vandenbem, C.; *Opt. Express*, **(2007)**, *15*, 4253.

(41) Mie, G.; *Ann. Phys. (Weinheim, Ger.)*, **(1908)**, *330*, 377.

(42) Lal, S.; Link, S.; Halas, N. J.; *Nat. Photonics*, **(2007)**, *1*, 641.

(43) Shuford, K. L.; Ratner, M. A.; Schatz, G. C.; *J. Chem. Phys.*, **(2005)**, *123*, 114713.

(44) Hao, E.; Schatz, G. C.; *J. Chem. Phys.*, **(2004)**, *120*, 357.

(45) Fischer, U. C.; Zingsheim, H. P.; *J. Vac. Sci. Technol.*, **(1981)**, *19*, 881.

(46) Lu, Y.; Liu, G. L.; Kim, J.; Mejia, Y.; Lee, L. P.; *Nano Lett.*, **(2005)**, *5*, 119.

(47) Zou, S.; Schatz, G. C.; *Chem. Phys. Lett.*, **(2005)**, *403*, 62.

(48) Atkinson, A. L.; McMahon, J. M.; Schatz, G. C. FDTD Studies of Metallic Nanoparticle Systems. In *Self-Organization of Molecular Systems*; Russo, N., Antonchenko, V. Y., Kryachko, E. S., Eds.; Springer Netherlands: Dordrecht, 2009; pp 11.

(49) Chan, G. H.; Zhao, J.; Schatz, G. C.; Van Duyne, R. P.; *J. Phys. Chem. C*, **(2008)**, *112*, 13958.

(50) Haes, A. J.; Zou, S.; Schatz, G. C.; Van Duyne, R. P.; *J. Phys. Chem. B*, **(2004)**, *108*, 6961.

(51) Acker, W. P.; Schlicht, B.; Chang, R. K.; Barber, P. W.; *Opt. Lett.*, **(1987)**, *12*, 465.

(52) Millstone, J. E.; Park, S.; Shuford, K. L.; Qin, L.; Schatz, G. C.; Mirkin, C. A.; *J. Am. Chem. Soc.*, **(2005)**, *127*, 5312.

(53) Etchegoin, P. G.; Galloway, C.; Le Ru, E. C.; *Phys. Chem. Chem. Phys.,* **(2006)**, *8*, 2624.

(54) Félidj, N.; Grand, J.; Laurent, G.; Aubard, J.; Levi, G.; Hohenau, A.; Galler, N.; Aussenegg, F. R.; Krenn, J. R.; *J. Chem. Phys.*, **(2008)**, *128*, 094702.

(55) Marty, R.; Baffou, G.; Arbouet, A.; Girard, C.; Quidant, R.; *Opt. Express,* **(2010)**, *18*, 3035.

(56) Pastoriza-Santos, I.; Liz-Marzan, L. M.; *J. Mater. Chem.*, **(2008)**, *18*, 1724.

Chapter 3: Modeling the Electric Field Distribution around a Hexagonal Array of Gold Nanotriangles[℘]

3.1. Introduction

The full control of the optical properties of metallic nanostructures that can be applied to the development of new molecular sensors has attracted the attention of researchers in different fields of science.[1-6] By modifying different physical parameters, such as the nature of the metallic material,[7,8] the architecture of the structured surface,[7-10] the dimensions of the nanostructures,[9] or the interparticle distance between features,[7,9] the plasmonic properties of these metallic nanostructures can be finely tailored. This opens a wide range of possibilities, not only to engineer specific nanostructures with a complete control of the different parameters responsible for such a phenomena;[5,6,10-13] but also to develop methods that can predict and explain the optical behavior of these structures.[14,15]

A description of the principles behind the plasmonic effect in nanoparticles was given in the previous chapters. As it was proposed, the traditional analytical methods based on Maxwell's equations, such as Mie's or Gans's theories,[14,16,17] only explain the optical behavior of spherical structures; and different approximation methods are required in order to understand the plasmonic properties of more complex designs, like a hexagonal array of metallic nanotriangles.

In this context, computational electrodynamic studies are very useful to calculate some of the optical properties of the different designs and support some of the experimental results. There are different methods for modeling the optical response based on various

---

[℘] A version of this chapter has been published elsewhere: [*Phys. Chem. Chem. Phys.* (**2010**), *12*, 6810] , Reproduced by permission of the PCCP Owner Societies. Reproduced with permission from [*J. Phys. Chem. C* (**2010**), *114*, 19952.] Copyright 2011 American Chemical Society.

forms, to solve Maxwell's equations. The most popular numerical methods are the discrete dipole approximation (DDA),[15,18,19] the finite element method (FEM),[20,21] and the finite-difference time domain (FDTD) method,[15,19] which is used in this work.

The scope of this chapter is to present numerical calculations that explain the optical behavior of Fischer's patterns[22] positioned over glass slides. As it was described in the previous chapter, this design has been extensively used for surface-enhanced spectroscopy;[4,7,10,13,23-25] however, their plasmonic properties have not been thoroughly studied. Herein the experimental extinction spectra of an array of Fischer's pattern are compared with the results obtained by using FDTD methods, used to model both the extinction spectra, and the electric field intensity spectra of a Fischer's pattern unit lattice. In addition, the effect of changing the input polarization, the size of the triangles, and the wavelength of irradiation on the electric field distribution around Fischer's patterns is investigated. Therefore, this chapter compares the far-field experiments done on Fischer's patterns with a numerical method; and in addition it predicts the interaction of this the incoming field with these arrays in the near-field.

3.2. Experimental methods to detect the LSPR in nanostructures

3.2.1. In the far-field

Experimentally, the determination of the plasmonic properties of metallic nanostructures is mostly performed as a function of the angle of incidence of incoming light (photon), the impinging wavelength, or as a function of the position of the area irradiated.[13,26] Thus in the extinction/absorption spectra, the LSPR bands (λ_{max}) indicate the strongest interactions of the electron cloud at specific wavelengths of irradiation.[11] A more detailed explanation of the different practical considerations and interpretation of the bands in the spectrum is given in Chapter 2. In short, the different bands detected in the LSPR spectrum represent the different distribution of the resonant electron cloud.

3.2.2. In the near-field

Several research groups have explained these plasmon properties by studying the confinement of the near field around nanostructured materials using various techniques. It has been reported that electron-based spectroscopy can be used to study the electric field distribution around nanostructures with sub-nanometer resolution. This was performed using electron microscopy to spatially resolve, and correlate with topography, the localized and extended excitations in any material.[27,28] Some of the approaches involve scanning transmission electron microscopy (STEM) to collect the energy distribution of a thin sample, scanning electron microscopy (SEM) to provide information from the collection of secondary electrons and cathodoluminescence emission, and finally photoemission electron microscopy (PEEM) to map the photo-excitation process in illuminated nanostructures.[27]

Optical methods such as near-field scanning optical microscopy (NSOM) and scanning tunneling microscopy (STM) have also been used, with the aim to probe the evanescent field localized around nanostructures.[27] Even though these methods allow a spatial resolution down to the angstrom scale, these techniques generally require a conductive material, and the probe needs to be extremely close to the sample. This can lead to an interaction that would alter theoptical properties of the sample.[27,29,30]

Recently, an elegant approach to indirectly image the near-field distribution was performed with the use of a photosensitive azo-dye polymer as a thin-film on top of a nanostructured surface. After irradiation, a change in topography provides information related to the electric field distribution of the sample.[31-34] This technique provides a convenient method to study the near-field distribution over surfaces; however, the interaction of the nanostructures with the electromagnetic field is limited to the range of wavelengths that is compatible with both the photosensitive dye and the plasmon band of

the metallic structure. A more detailed description of this approach is given in Chapter 4, where a polymer functionalized with an azobenzene dye is used to study the near-field distribution on arrays of Fischer's pattern.

The different experimental methodologies described, provide important insights into the interpretation of the plasmonic properties of nanomaterials. Nevertheless, as the design of the nanostructures becomes more complex, i.e. a non-spherical structure with a large number of collective resonances and more spatial averaging, the connection between the extinction/absorption spectra and the electric field enhancement is less direct.[35] On top of this mismatch, the optical spectrum of nanostructures larger than the 100 nm range can be even more complex. When the size of the nanostructures increases, it induces a retardation effect inside the plasmonic particles, leading to the presence of higher multipolar plasmon bands.[36-39] Therefore, the study of the plasmonic properties of non-spherical structures as part of an array, whose size is on the order of hundreds of nanometers, requires a careful analysis, and the use of numerical methods to better understand the optical behavior of these nanostructures.

3.3. Numerical approximations to model the LSPR in nanostructures

Computational electrodynamic studies are commonly used to model optical properties such as the extinction and absorption spectra or the near field/far field distribution of the different designs, and corroborate with experimental results. Several approaches are used to model the optical response, based on various forms in order to solve Maxwell's equations. The most popular numerical methods are the discrete dipole approximation (DDA),[15,18,19] the finite element method (FEM),[20,21] and the finite-difference time domain (FDTD) method,[15,19] This section provides a brief description and comparison of these three numerical methods.

3.3.1. Discrete dipole approximation (DDA)

The discrete dipole approximation, also referred as coupled dipole approximation, is an adapted version of a method initially proposed to describe light scattering from interstellar grains, that is used in the study of metal nanoparticles.[15] The DDA method simplifies the nanostructures by an assembly of *N* cubic elements whose polarizabilities α_i *(i = 1, 2, ... N)* are determined by the dielectric function of the metal (ε_m). The size of each lattice point in the cubic array is sufficiently reduced that the polarization induced (P_i) in each element only considers the interaction with the incident electromagnetic field ($E_{inc,\,i}$) and with the induced fields from the neighbor dipoles ($E_{dipole,\,i}$).[15,18,40] As a result, Maxwell's equation gets simplified to an algebraic problem involving several coupled dipoles, where the local field ($E_{loc,i}$) at r_i is the sum of the incident and retarded fields of the order of *N*-1 dipoles, as expressed in **(1)** and **(2)**.[8,15]

$$P_i = \alpha_i \cdot E_{loc.i} \tag{1}$$

$$E_{loc,i} = E_{inc,i} + E_{dipole,i} = E_o \exp(ik \cdot r_i) - \sum_{\substack{j=1 \\ j \neq i}}^{N} A_{ij} \cdot P_j \tag{2}$$

Where E_o and $k = 2\pi/\lambda$ represent the amplitude and wave vector of the incident electromagnetic field, respectively; and the interaction matrix (A) with the vector from dipole i to dipole j (r_{ij}) is described in **(3)**.

$$A_{ij} \cdot P_j = \frac{\exp(ikr_{ij})}{{r_{ij}}^3} \times \left\{ k^2 r_{ij} \times \left(r_{ij} \times P_j \right) + \frac{(1 - ikr_{ij})}{{r_{ij}}^2} \left[{r_{ij}}^2 P_j - 3 r_{ij} (r_{ij} \cdot P_j) \right] \right\} \tag{3}$$

One of the limitations of this method is the coupling between dipoles generates a large number of elements in the matrix. However, other complementary methods based on Fourier transforms and complex conjugate gradients,[8,15,18] allow one to overcome these problems and to use thousands of dipoles for routine calculations. Thus, DDA is usually the selected method to study isolated nanoparticles of arbitrary shape, whose size is not bigger than a hundred nanometers, and that are surrounded by complex surroundings.[8,15]

To calculate the plasmonic properties of metallic nanostructures and dielectrics using DDA method one can make use of DDSCAT,[41] an open-source-Fortran-based code.

3.3.2. Finite element method (FEM)

A different option to compute the optical properties of nanostructures is the finite element method, which divides the domain into several smaller regions, usually with a tetrahedral geometry, to overcome the overall problem space.[40] Each element in the domain has a local function, and the value of their vector fields ($\bar{E}$) corresponds to the sum over n interpolation points, of chosen basis functions (N_j) and a column vector of unknown coefficients (ϕ_j), expressed in **(4)**.

$$\bar{E} = \sum_{j=1}^{n} N_j \phi_j \qquad \textbf{(4)}$$

In order to obtain a meaningful solution of N_j in **(4)**, Gauss's law must be satisfied and a boundary condition, which considers that the tangential field components are continuous across the surface of the particle.[15,40] One example of such a vector function is the Whitney tetrahedral form, and is mathematically defined along the edges of the tetrahedral element as **(5)**.

$$N_j = l_j(\zeta_{i1}\bar{\Delta}\zeta_{i2} - \zeta_{i2}\bar{\Delta}\zeta_{i1}) \qquad \textbf{(5)}$$

In this equation l_j represents the length of edge *j*, and ζ_i are the simplex coordinates of node *i*, where *i1* and *i2* are the end point of edge *j*.[15] Then, the results can be reintroduced in Maxwell's equations and solved by using matrix algebra.[40] A more detailed explanation of this method and its optimization techniques goes beyond the scope of this chapter, but more information can be found elsewhere.[15,21,40]

The advantage of FEM over other methods relies on the possibility to selectively refine the unit elements. Therefore, irregular geometries as well as large regions containing fine

details are ideal study cases. Thus, it is possible to resize the mesh in those areas containing a high electric field gradient, where a higher level of accuracy might be required. Examples of commercial software based on FEM are Comsol™,[42] and Ansoft' s High Frequency Structure Simulator (HFSS™).[43]

3.3.3. Finite-difference time domain (FDTD)

FDTD method solves the Maxwell's equations by using a series of finite-difference algorithms that discretize the space and time. The spatial domain is simplified by the use of a uniform Cartesian grid. The best known discretisation method is based on Yee's algorithm.[14,15] This unit cell contains individual electric and magnetic pointing vector components, shifted by half-grid points relative to each other (**Figure 3.1**).[19] In addition the range of time is also simplified with discrete values. Thus, the excitation wavelength is not consider as a plane wave, instead as a pulse that computes the difference in the field components before and after being applied, and the process continues repetitively until the field converges and reaches a steady-state solution.[40] Although this is a time-domain based method, it can be used to calculate the frequency domain spectra of different designs, using Fourier transformations.[14,15]

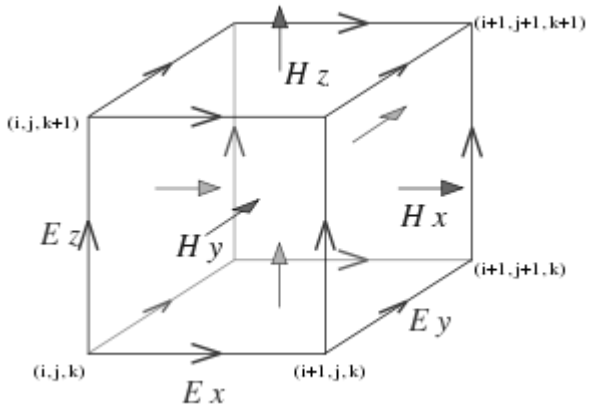

Figure 3.1. Yee cell.

FDTD being a time-dependent method, the dielectric function values of the metals studied must have a broader range than the frequency range of interest. This comes from the fact that the pulse of light used as the source generates a broadband frequency output, requiring broader dispersion information.[40] Although, this might represent a disadvantage of the method, overall FDTD allows the study on non-spherical structures, and in a similar way as FEM, large structures. Some commercial software based in FDTD are Remcom Xfdtd™,[44] and FDTD Solutions from Lumerical.[45]

From the different numerical methods described above, FDTD was selected to determine the plasmonic properties of a periodic hexagonal array of gold nanotriangles. First the calculated results are compared with the extinction spectra of a specific array of triangles, with 357-nm-length size and a 184-nm-interparticle-distance, reported in Chapter 2. Then a calculated extinction spectrum obtained from the FDTD simulations is compared with the experimental spectrum, to demonstrate the correlation between both results. The electric field distribution calculated for such an array is analyzed under the effect of two different linear parallel and orthogonal polarizations. Finally, this chapter investigates how the change in the polarization, the size of the triangles, and the wavelength of irradiation alters the electric field distribution on Fischer's patterns. Similar studies in the field have been performed for isolated nanotriangles or for their dimers.[8,9,37,39,46] It is noteworthy to mention that, in these studies, the collective interaction between multiple triangle pairs with different orientations in the array were considered. Therefore, this study provides additional information for the design of surface-enhanced spectroscopy platforms and experiments.

3.4. Theoretical calculations

The extinction spectrum for one of the Fischer's patterns was calculated using a computational method, FDTD Solutions software from Lumerical. The calculations were

set up as a three dimensional system with a 5 nm resolution grid, for 500 femtoseconds, and including the appropriate boundary conditions. A plane wave source was chosen at a 400-1100 nm working wavelength range, with a propagation axis perpendicular to the plane of the platform, and with a polarization parallel either along the X or Y axis, as shown in **Figure 3.2**. The dielectric constant of the glass (silicon dioxide) and gold were described by Palik[47] and the CRC[48] values, respectively, provided in the material database of the software. The sum of the total electric field intensity ratio per area ($(\sum|E|^2)$/area) as a function of the wavelength (λ: 400-1100 nm) and the length of the triangles (L100-300 nm), was calculated for a group of arrays of Fischer's pattern under described polarized inputs (Px and Py). The calculation of the relative total electric field intensity ($|E|^2$) and its image plot was obtained from the sum of its components ($|E_x|^2 + |E_y|^2 + |E_z|^2$) and it was calculated 10 nm above the surface. In addition, specific points on the arrays were studied to determine the localized electric field intensity. The size of each point is determined by the 5 nm resolution grid. In the case of the comparison study between the experimental and numerical results, the physical parameters, such as size and thickness of the nanotriangles, used in the calculations of the extinction spectrum and were obtained from the AFM data, obtained in Chapter 2.

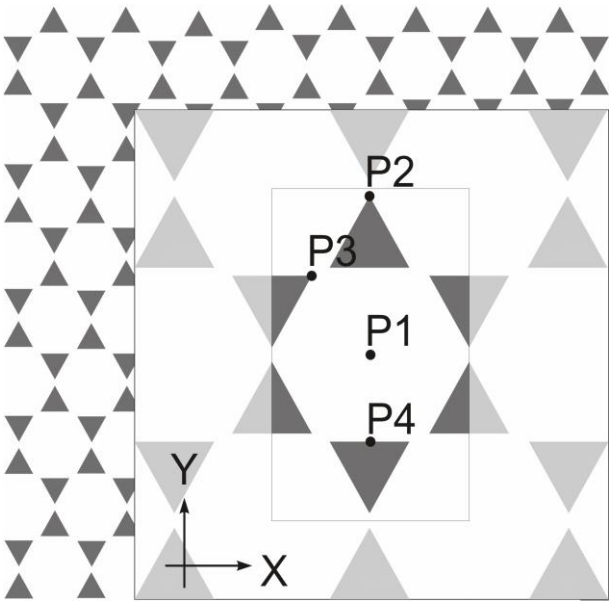

Figure 3.2. Schematic representation of a periodic array of Fischer's pattern where the lattice unit has been highlighted and the points studied have been labeled.

3.5. Results and discussion

3.5.1. Polarized LSPR spectral contributions

The extinction spectra of a Fischer's pattern-A (length: 357 nm, interparticle distance: 184 nm, gold thickness: 40 nm) under the exposure of a non-polarized and linearly polarized light source (**Figure 3.3.a**), obtained in Chapter 2, were used to form a basis of comparison with the computed results obtained with FDTD. Herein, the simulations considered an incoming light linearly polarized along the X and Y axes, **Figure 3.3.b**. Due to the high memory requirements, the calculation was performed for one lattice unit, with a mesh accuracy of 5 nm.

The results show a good agreement with the experimental values for the peak at around 580 nm, shown in **Figures 3.3.a,b**, specifically for the spectra obtained with a Y-polarized source. However, there is a mismatch for the peak at higher wavelength when

the incoming light is linearly polarized along the X axis. These differences might be due to the limitations of the calculations. We are considering just one lattice unit, and the role of the sharpness of the nanotriangular vertices was not taken into consideration. Other groups have reported similar sharpness issues in the study of a single bow tie assembly,[49] and a small modification to the shape of the triangles.[8,39] It is noteworthy that in addition to the main LSPR bands, the simulations show the presence of a shoulder around 540 nm, not experimentally detected, which was assigned to a higher order multipole mode.[39,50,51]

In addition, **Figure 3.3.c** shows the calculation of the total near-field intensity at each wavelength for Fischer's pattern-A lattice unit, and its relationship with the incoming polarized light. Each point in the spectra is the sum of the total electric field intensity value at each grid point in the unit lattice as a function of the wavelength of light. The spectra for the X and Y polarization suggest similar intensity values at around 582 nm. This implies that the averaged enhancement on a lattice unit of a Fischer's pattern is independent of the polarization of the incoming light. However, in the case of the 680-720 nm region, the average enhancement value per unit lattice is polarization-dependent. The calculated spectra describe higher intensity values when the incoming light is polarized along the X axis. These differences in the extinction spectra and the near-field intensity spectra have been previously discussed for two spherical colloids.[52] In that study, the authors showed that there is no simple connection between the extinction and the intensity spectra, and that each case must be studied carefully.[35] There have been a few studies reported where the extinction spectrum of Fischer's patterns was related to the enhancement factor.[53,54] In all those cases, the connection was established by the detection of the surface-enhanced Raman spectra, but the effect of the polarization of the incoming light and its relationship with the intensity of the near-field was not considered.

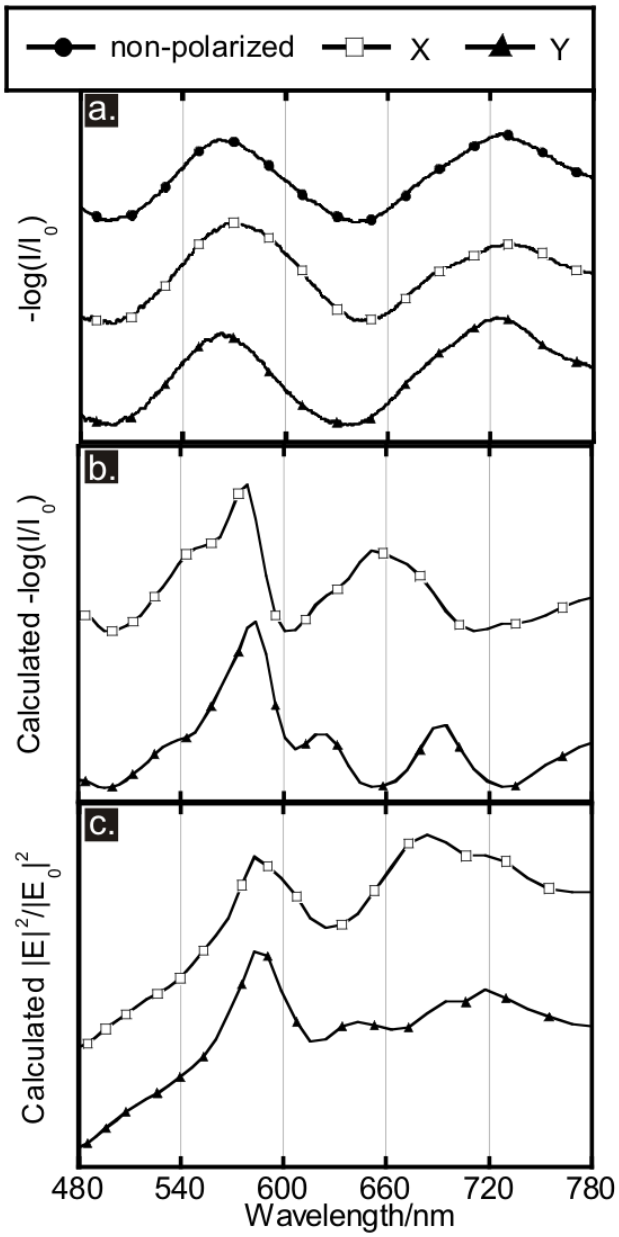

Figure 3.3. Experimental extinction spectra of Fischer's pattern-A (357 nm length size, 184 nm gap distance and 40 nm gold thickness) (a), calculated extinction spectra (b), calculated near-field intensity spectra for one unit lattice of Fischer's pattern-A (c). All the spectra shown here were spatially correlated.

3.5.2. Total near-field enhancement spectra of Fischer's pattern: length and polarization effect

Similarly to the calculation of the total near-field intensity spectra for Fischer's pattern-A, the sum of the total near-field intensity ratio per area ($(\sum|E|^2)$/area) as a function of the wavelength (λ: 400-1100 nm) and the length of the triangles (L100-300 nm), was calculated for a periodic array of Fischer's pattern under two different linearly polarized inputs along the X and Y axis (**Figure 3.4**). From these results, it is possible to detect a change in the total surface near-field intensity spectrum when the length of the triangles is modified. Most importantly, in all of the studied cases, there is a larger enhancement of the electric field intensity values when the incoming beam is linearly polarized along the Y axis, as summarized in **Figure 3.4.c**.

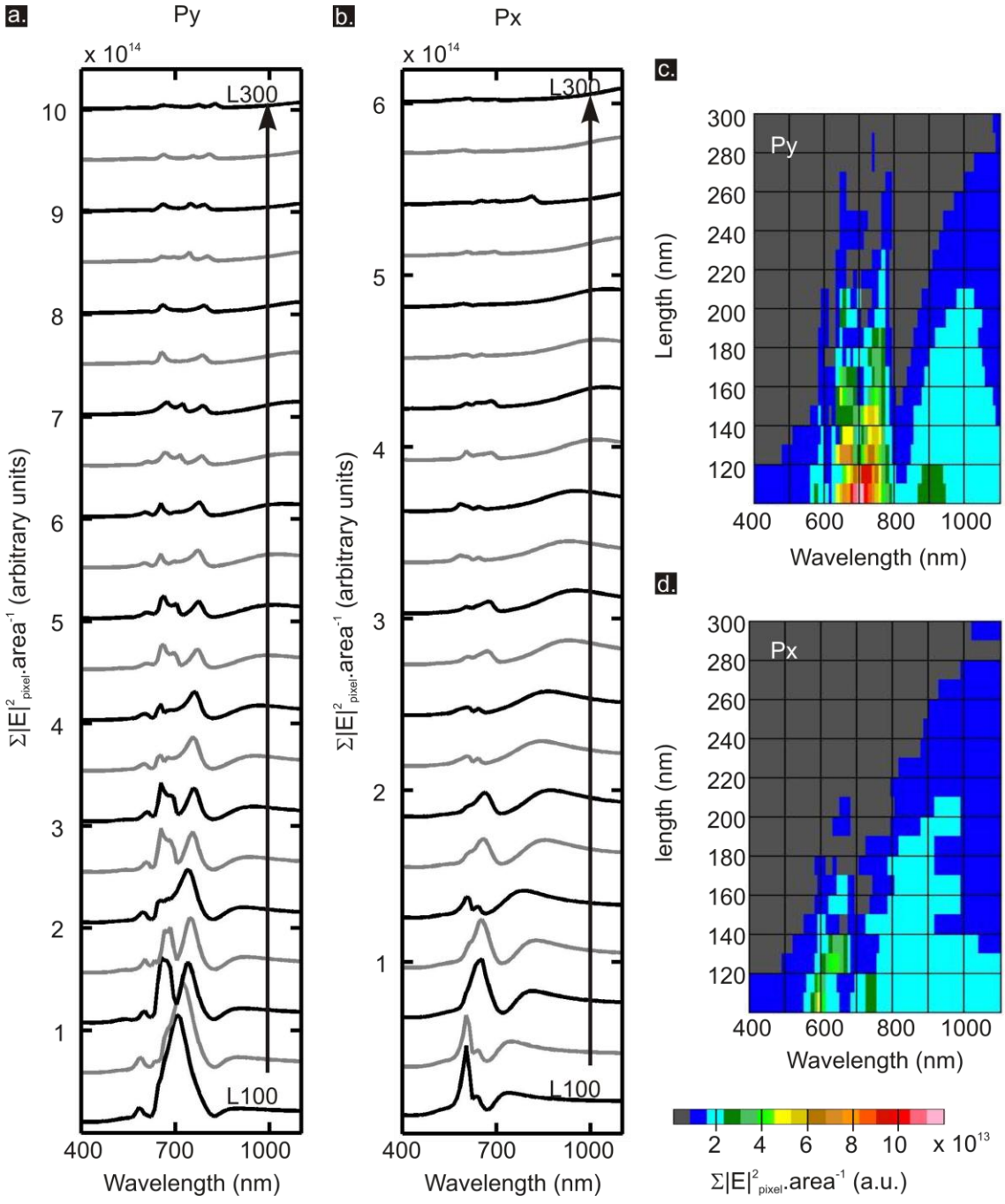

Figure 3.4. Calculated sum of the total near-field per area irradiated for the arrays of Fischer's patterns, when the length size of the triangles is modified (L: 100-300 nm), and when the incoming polarization is along the Y (a,c) or X (b, d) axes. Spectra in (a) and (b) have been spatially correlated.

More specifically, when the arrays of Fischer's patterns are irradiated with a linearly polarized light parallel to the Y axis (Py), the total surface electric field intensity spectrum presents two main regions, as shown in **Figures 3.4.a,c**. A spectral domain is presented between 550-800 nm, where the intensity, shape, and position in the spectrum is altered when the length of the triangle is modified. As the length sides of the triangles increases, the main band resolves into a group of superimposed bands, but with reduced intensity. A second spectral domain, less intense, appears at around 825-1100 nm, that broadens and red-shifts as the length of the triangles increases. When the linearly polarized input is parallel to the X axis (Px), it is also possible to detect two spectral domains (**Figures 3.4.b,d**). The first domain is in the range of 550-700 nm; here, as well as in all the cases for Py, the intensity of the band is reduced as the length of the triangles increases. The second domain is detected at 720-1100 nm, with a similar trend as in the case of the Py-input. From these two sets of spectra, it is possible to estimate the wavelength of irradiation with the highest electromagnetic field enhancement. More importantly, these results show that the array interacts differently with the incoming beam, depending on its orientation with respect to the input polarization of the impinging field. Such a polarization effect has been studied before for less complex designs,[8,15,39,52,55,56] and it will be analyzed in more detail in the following sections.

3.5.3. Contribution of the electric field components

Since the polarization of the incoming light source does alter the average near-field enhancement spectrum, it is important to determine the contribution of the individual components of the local field to the total intensity. **Figure 3.5** shows the total near-field intensity spectra and its different components for a lattice unit of Fischer's pattern-A, when the incoming light is linearly polarized along the X axis (**Figure 3.5.a**) and along the Y axis (**Figure 3.5.b**). Shown in **Figure 3.5**, the main contribution to the total intensity is coming from the component parallel to the incoming polarization of the light, but at certain wavelengths, the light is depolarized. In other words, the incoming beam changes its polarization and has substantial contributions along the other axes. As a result, a peak is observed for the overall average near-field spectrum. Previous studies have

observed this depolarization effect on specific regions on spherical nanoparticles,[52,55] and on isolated triangular nanoparticles;[31,57] and identify these regions with near-field intensity images at specific wavelengths.

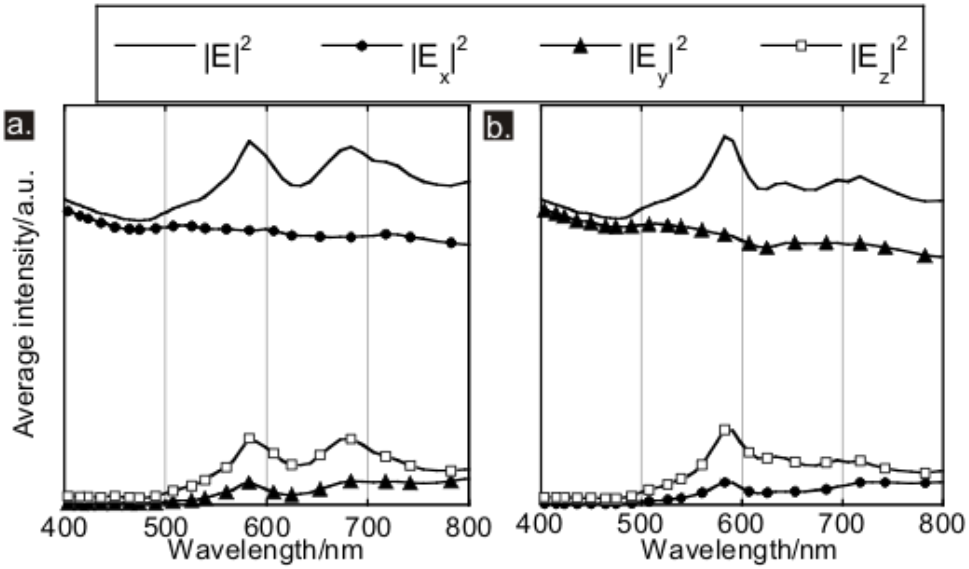

Figure 3.5. Intensity spectra of the total electric field of Fischer's pattern-A lattice unit as well as the contribution to the intensity of each component when the incoming light is X polarized (a) and Y polarized (b).

3.5.4. Near-field distribution

To determine how the electric field-nanoparticle interaction occurs, or where the hot-spots are present on the lattice unit area, it is necessary to map the localized electric field intensity on the lattice unit. The calculation of the hot-spots for the L-100-nm hexagonal array of gold nanotriangles was estimated from the electric field distribution. **Figure 3.6** shows how the total ($|E|^2$) and the individual ($|E_x|^2$, $|E_y|^2$, $|E_z|^2$) electric field components are enhanced for this array when irradiated with an input polarization parallel to the Y and X axes (Py and Px respectively). Selected wavelengths (704 nm for Py-input and 603

nm for Px-input) were used in this array since they correspond to the most intense plasmon bands for a specific input polarization, as shown in **Figure 3.4**.

In all cases, the high electric field intensity is localized at the vertices of the triangles. However, for these two different conditions, the hot-spots are not present at the same position, which proves that the electric field distribution is dependent on the irradiation wavelength, and/or the polarization direction of the incoming beam with respect to the sample. In order to prove that the combination of the polarization and the irradiation wavelength are crucial parameters for the activation of hot-spots, the total electric field distributions for the ninety degree counterparts was calculated, i.e.: Px at 704 nm (**Figure 3.6.a, row 2**) and Py at 603 nm (**Figure 3.6.b, row 1**). In both situations, the total electric field distribution is different and presents a reduced intensity. Therefore, both the polarization and the irradiation wavelength must be considered in order to optimize the electric field enhancement on the array.

Section 3.3.3 showed that the near-field intensity spectrum of the different X, Y and Z components is affected by a change in the polarization irradiation conditions. This effect is also illustrated in **Figure 3.6** by showing the electric field distribution of the different electric field components: $|E_x|^2$ (**Figure 3.6, column 2**), $|E_y|^2$ (**Figure 3.6, column 3**) and $|E_z|^2$ (**Figure 3.6, column 4**). From the analysis of these electric field distribution maps, it is possible to see that in all cases, the in-plane component has a small contribution to the total electric field. The largest electric field intensity comes from the out-of-plane Z component as part of a depolarization effect, previously studied with nanospheres dimers and tetramers.[55] Although the electric field intensity was measured on a plane 10 nm above the gold surface, tridimensional studies performed on bow ties[37] suggest a similar behavior, which confirms the analysis done on the L100-nm lattice unit.

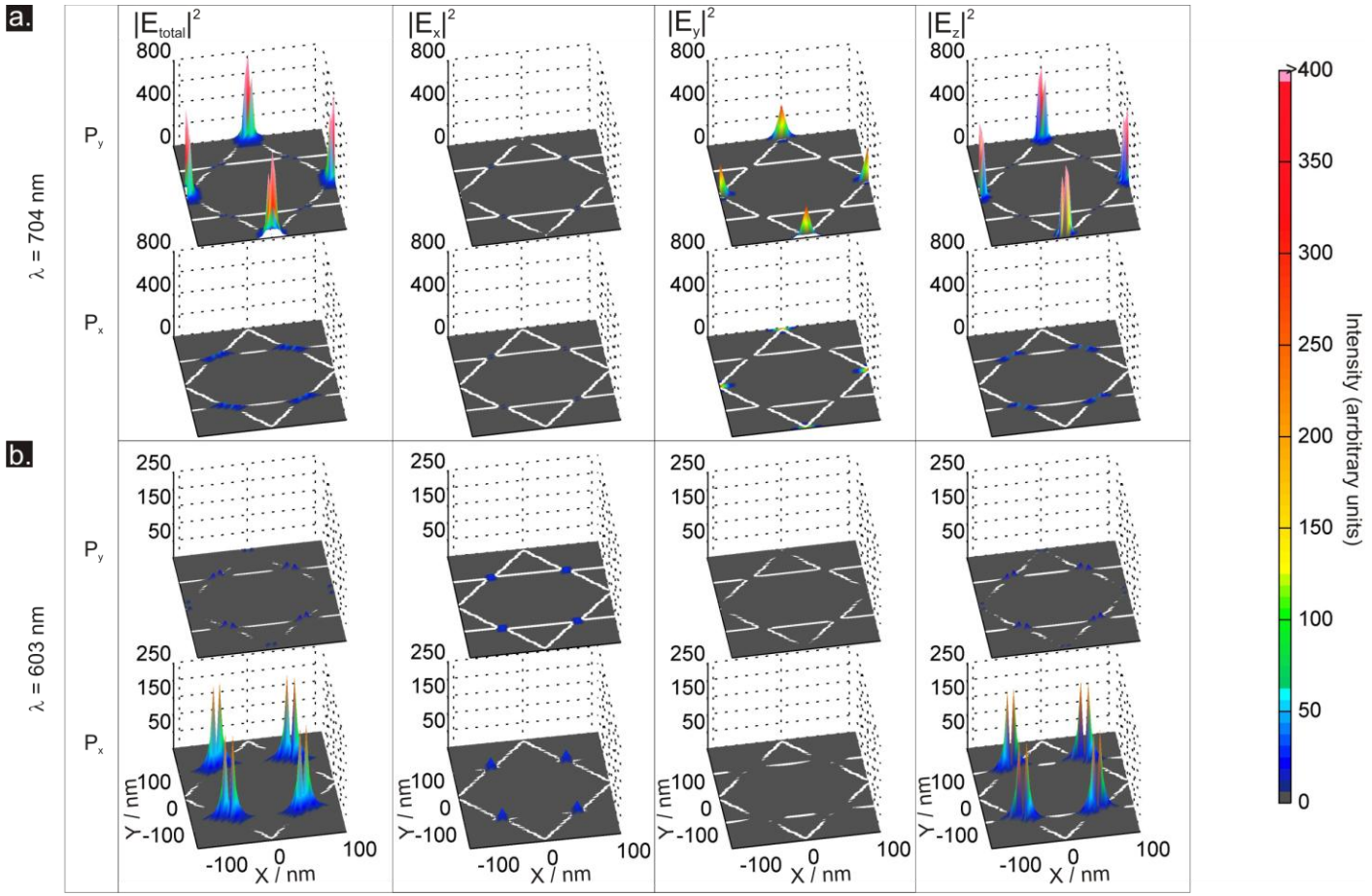

Figure 3.6. Calculated electric field distribution of a L100-nm unit lattice at 704 nm wavelength (a) and at 603 nm wavelength (b), when irradiated with a Py-input (row 1 and 3) and a Px-input (row 2 and 4): total electric field (column 1), in-plane X component (column 2), in-plane Y component (column 3), and out-of-plane Z component (column 4).

The effect of the polarization on the near-field distribution of Fischer's pattern-A presents a similar behavior than the one explained above for the L100-nm array. Although the structures are bigger and the interparticle distance is larger, than the array described, the effect on the input polarization is observed. The most intense hot-spots when irradiated at 582 nm (the most intense band in the total near-field intensity spectra) are detected when light is polarized parallel to the Y-axis, and localized at the vertex of the triangles.

3.5.5. Localized electric field

The electric-field-intensity spectrum was calculated at four different points on the Fischer's pattern lattice unit (P1-P4 on **Figure 3.2**) for the different arrays studied L100-300-nm. These points represent different regions on the array and their results are equivalent with other symmetric points in the periodic array. The effect of changing the length of the nanotriangles and the polarization of the incoming beam was also studied on all these points. From this analysis, it is possible to identify the localized electric field enhancement, and how these points are modified when the polarization and the wavelength of the incoming beam are altered. **Table 3.1** and **Figures 3.7-10** summarize the electric field intensity spectra for the four different points studied. In addition, the table also shows the main component ($|E_i|^2$) responsible for the electric field enhancement at each point. The results are discussed in the following paragraphs.

Table 3.1. Summary of the localized electric field enhancement of Fischer's pattern lattice unit irradiated with Py and Px-beam.

Py							
	$\|E_i\|^2$	$\Delta\lambda_{1y}$ = 750-1100 nm			$\Delta\lambda_{2y}$ = 500-860 nm		
		$\|E\|^2/\|E_0\|^2$	L (nm)	λ	$\|E\|^2/\|E_0\|^2$	L (nm)	λ
P1	$\|E_y\|^2$	1-3	100-300	780- >1100	1-3	100-300	520-825
P2	$\|E_z\|^2$	76-1044	100-250	880- >1100	766-3536 111-1619	120-300 100-300	600-780 700-860
P3	$\|E_z\|^2$	19-150	100-240	800- >1100	6-559 10-680	100-300 100-300	700-850 500-800
P4	$\|E_y\|^2$	1-16	100-300	750-900	5-15 1-10	120-300 100-300	680-780 500-700
Px							
	$\|E_i\|^2$	$\Delta\lambda_{1x}$ = 650-1100 nm			$\Delta\lambda_{2x}$ = 500-700 nm		
		$\|E\|^2/\|E_0\|^2$	L (nm)	λ	$\|E\|^2/\|E_0\|^2$	L (nm)	λ
P1	$\|E_x\|^2$	1-3	100-300	650- >1100	2-2	100-300	500-700
P2	$\|E_x\|^2$	1-1	220-300	850- >1100	1-1	100-300	550-700
P3	$\|E_z\|^2$	54-665	100-260	700- >1100	62-515	100-300	580-700
P4	$\|E_x\|^2$	2-3	100-300	700- >1100	1-3	100-300	500-700

Points 1-4 are defined in Figure 3.2. Δλ: plasmon band region; $|E|^2/|E_0|^2$: ratio of the total electric field intensity with the incident electric field intensity, defined as electric field enhancement; L: length of the triangles in the array; λ: wavelength range where the plasmon peak is present (All the spectra are shown on Figure 3.7); $|E_i|^2$: electric field component that contributes the most to the total electric field, the values can be the in-plane X component ($|E_x|^2$), the in-plane Y component ($|E_y|^2$) , or the out-of-plane Z component ($|E_z|^2$).

P1: center of the lattice unit. The electric field enhancement ratio at this point is almost negligible when there is a Px or Py-input ($|E|^2/|E_0|^2 < 3$). However, two spectral domains can be detected for all the different arrays irradiated with a linearly polarized input, $\Delta\lambda_{1y}$ = 780-1100 nm and $\Delta\lambda_{2y}$ = 520-825 nm when irradiated with a Py-input (**Figure 3.7.a,c**), and $\Delta\lambda_{1x}$ = 650-1100 nm and $\Delta\lambda_{2x}$ = 500-700 nm when irradiated with a Px-input (**Figure 3.7.b,d**). A subtle change in the localized electric field enhancement and a slight increase in the intensity of the λ_{max} is detected when the length of the triangles increases. These

values primarily come from the electric field in-plane component parallel the polarized input. The spectral bands at this point might be the result of a collective interaction between the triangles present in the array.

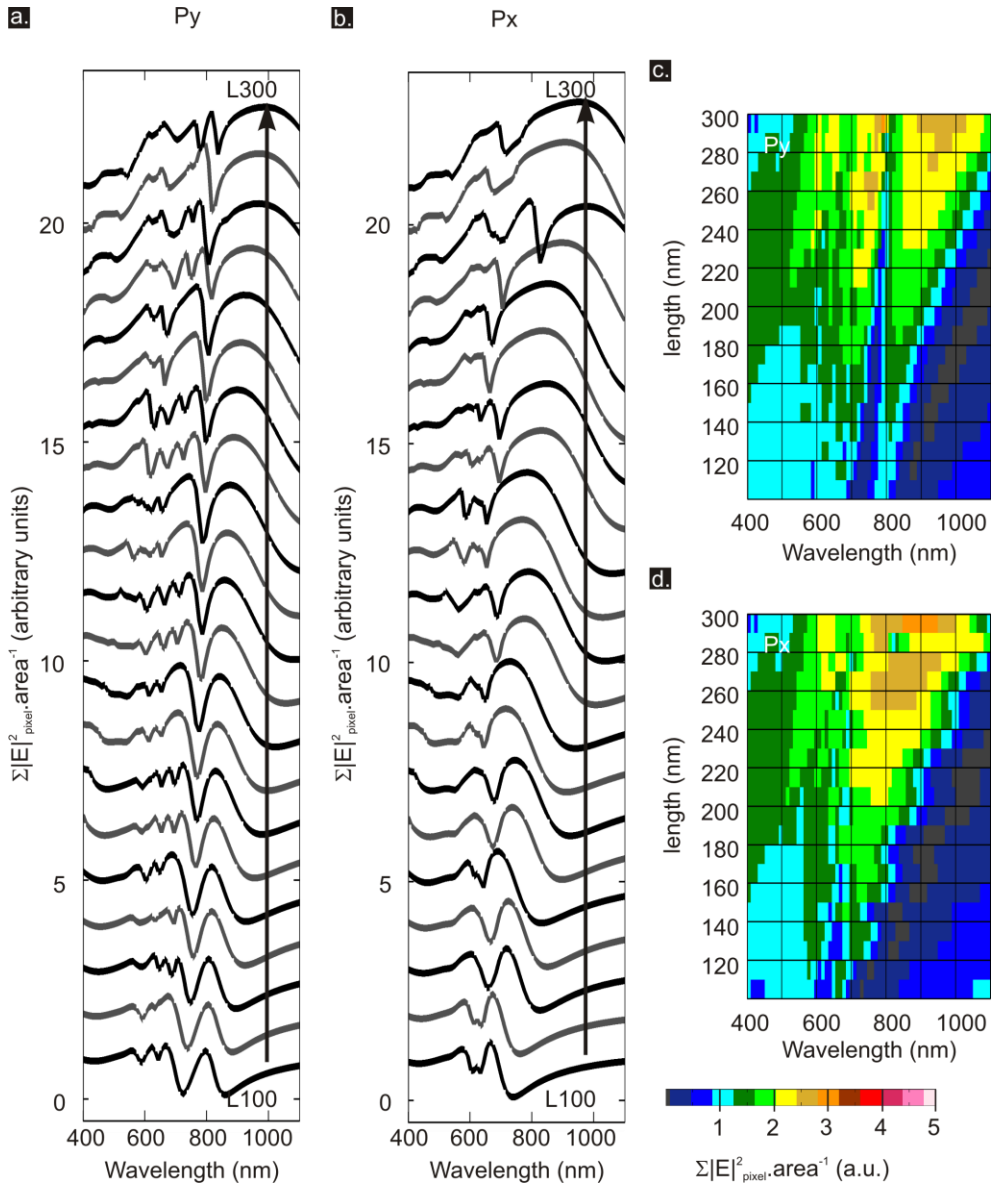

Figure 3.7. Calculated localized electric field spectra ($|E|^2/|E_0|^2$) for P1 when irradiated with a Py (a, c) and Px input (b, d). Spectra on A and B have been spatially correlated and the direction of the arrows indicates the increase on the length of the triangles in the array (L100-300 nm)

P2: vertex along the perpendicular bisector of the triangular base. This point is the area with the highest electric field intensity values when the incoming beam is Py, whereas there is almost a non-detectable enhancement when irradiated with a Px-input. Similar to P1, two spectral domains are identified at this position for all the arrays. The first spectral domain ($\Delta\lambda_{1y}$) is detected on the 880-1100 nm wavelength region, where a modulation of the electric field band is observed when the length of nanotriangles increases. Thus, when the nanotriangles become bigger, a plasmon band gets red-shifted and becomes more intense. The highest enhancement in this domain is detected for the L-250-nm array when irradiated with a Py-input at λ~1100 nm ($|E|^2/|E_0|^2$ = 1044), **Figures 3.8.a, c**. However, the calculations suggest that the arrays of bigger features might have a λ_{max} at higher wavelength. The second domain corresponds to $\Delta\lambda_{2y}$= 600-860 nm, and it presents a set of two superimposed bands, that become more resolved and more intense as the length of nanotriangles increases (L-120-300-nm arrays). Herein, the highest enhancement at P2 is detected for the L-250-nm arrays at λ = 654 nm. In the case of the arrays that are irradiated with a Px-input (**Figures. 3.8.b,d**), the electric field enhancement is approximately 10^3 times less intense. However, it is still possible to detect the two spectral domains, $\Delta\lambda_{1x}$= 850-1100 nm and $\Delta\lambda_{2x}$= 550-700 nm, where the main band gets red-shifted as the triangle edges on the arrays become longer. The main electric field contribution for all these bands comes from the out-of-plane Z component when irradiated with a Py-input, and from the in-plane X component when irradiated with a Px-input. The strong intensity values at P2 has been studied on bow ties, where the hot-spots are more intense when irradiated with an incoming light polarized parallel to the interparticle distance axes,[49] which is in agreement with the calculations performed for P2.

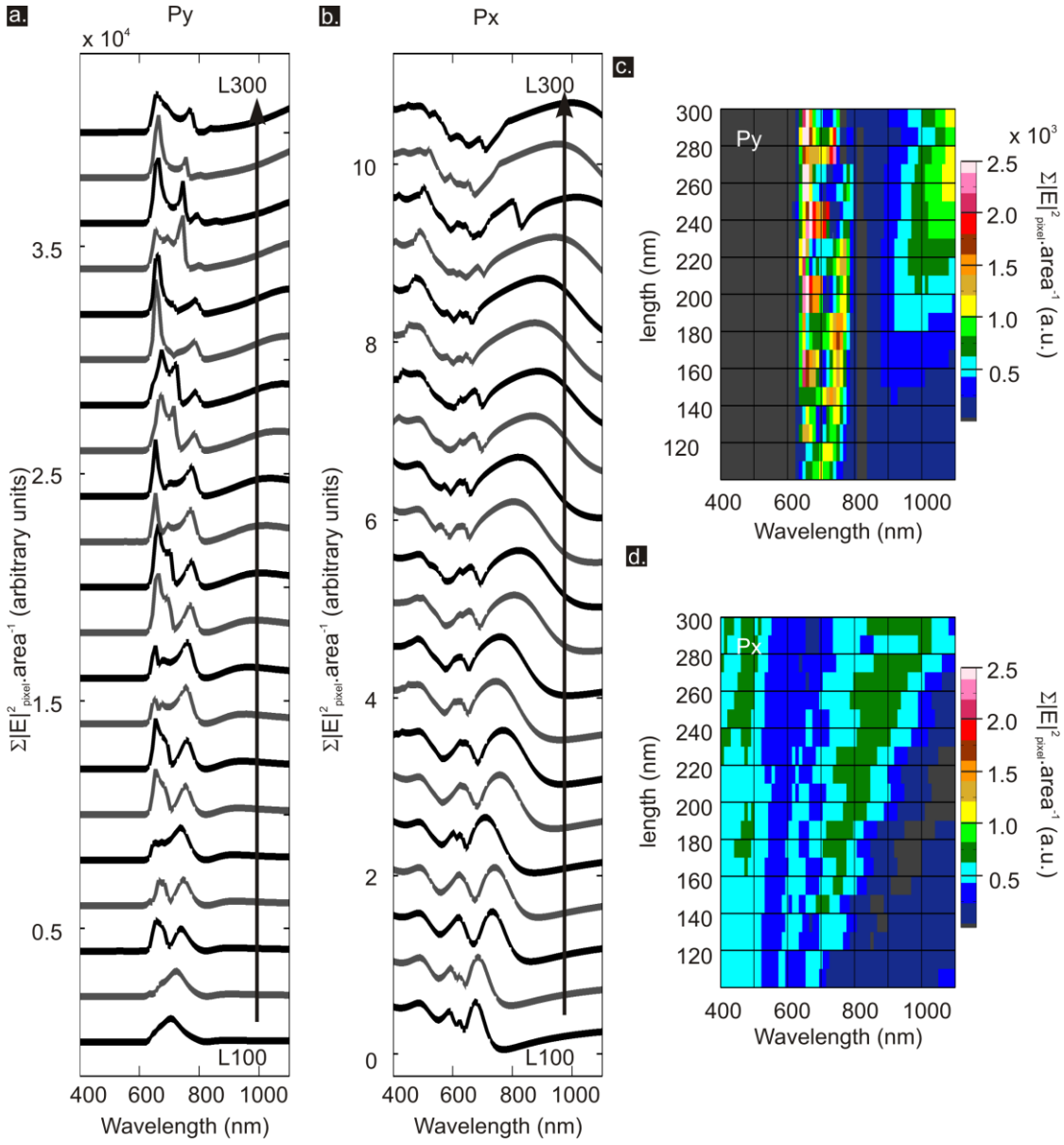

Figure 3.8. Calculated localized electric field spectra ($|E|^2/|E_0|^2$) for P2 when irradiated with a Py (a, c) and Px input (b, d). Spectra on A and B have been spatially correlated and the direction of the arrows indicates the increase on the length of the triangles in the array (L100-300 nm)

P3: vertex along the edge parallel to the X axis. When the arrays are irradiated with a Py-input, two spectral domains can be detected ($\Delta\lambda_{1y}$: 800-1100 nm and $\Delta\lambda_{2y}$: 500-850 nm).The first domain presents a relatively broad plasmon band that follows a similar trend as described for P1 and P2; when the length of the triangles increases, the main plasmon band red-shifts and becomes more intense. The biggest electric field intensity ratio ($|E|^2/|E_0|^2$= 150) in this domain is detected on the L220-nm array when irradiated at λ= 1039 nm. The second spectral domain appears as a group of bands with two main peaks. The L-280-nm array presents the highest enhancement in this spectral domain when irradiated with a Py-input at 755 nm wavelength ($|E|^2/|E_0|^2$ = 680), **Figures 3.9.a,c**. Contrary to P2, when the arrays are irradiated with a Px-input (**Figures 3.9.b,d**), the localized electric field intensity at P3 gets significantly enhanced. The first spectral domain ($\Delta\lambda_{1x}$: 700-1100 nm) presents a broad band with a similar trend as described for $\Delta\lambda_{1y}$. The highest enhancement is detected for the L-260-nm array irradiated at λ = 1049 nm ($|E|^2/|E_0|^2$= 665). A second spectral domain can also be detected for all the arrays ($\Delta\lambda_{2x}$: 580-700 nm) as a group of superimposed bands. The L-220-nm array irradiated with a Px-input at λ = 583 nm presents the largest enhancement in this domain ($|E|^2/|E_0|^2$= 515). The highest electric field contribution at this point comes from the out-of-plane Z component independent of the polarization of the incoming beam. Such an enhancement of the electric field intensity has been observed on isolated nanotriangles when irradiated with a linearly polarized light parallel to the base of the triangle.[37]

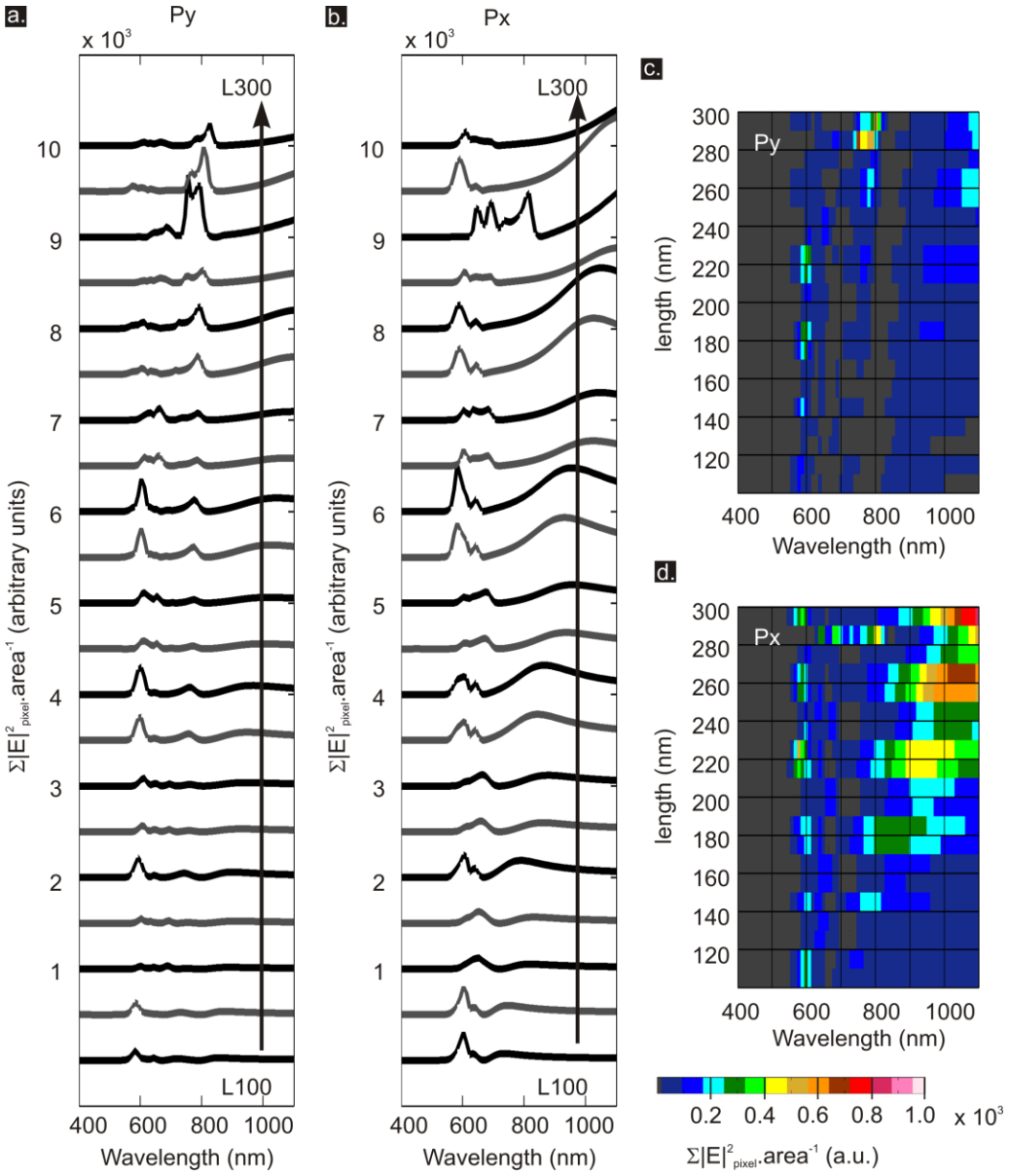

Figure 3.9. Calculated localized electric field spectra ($|E|^2/|E_0|^2$) for P3 when irradiated with a Py (a, c) and Px input (b, d). Spectra on A and B have been spatially correlated and the direction of the arrows indicates the increase on the length of the triangles in the array (L100-300 nm)

P4: midpoint of the edge parallel to the X axis. Two spectral domains are detected when the arrays are irradiated with a Py- or a Px-input ($\Delta\lambda_{1y}$: 750-900 nm, $\Delta\lambda_{2y}$: 500-780 nm, $\Delta\lambda_{1x}$: 700-1100 nm and $\Delta\lambda_{2x}$: 500-700 nm). The electric field enhancement values are less intense at this point than at the vertices of the triangles. When compared, the effect of changing the polarization of the incoming light, the enhancement is approximately five times stronger under the effect of a Py-input (**Figure 3.10.a,c**) than of a Px-input (**Figure 3.10.b,d**), where there is an almost negligible enhancement. A broad band can be detected in the first spectral domain, and a set of overlapping bands is present on the second spectral domain. In all the cases, the bands follow the trend described before; as the triangles on the arrays become bigger, the λ_{max} red-shifts and are slightly enhanced. Similar to P1, where there is almost no enhancement, the main electric field contribution comes from the in-plane component parallel to the incoming input.

The analysis of these four points on the different arrays of nanotriangles explains the results shown on the $\Sigma|E|^2$/area spectra under the effect of two linearly polarized inputs. The most intense areas are at the vertices of the triangles. When irradiated with a Py-input, P2 is the most intense region, and in the case of a Px-input, the enhancement primarily comes from P3. In all the cases, the spectra of the four points and the sum of the total electric field intensity show two spectral domains. Thus, a broad band is detected at higher wavelengths, while a set of superimposed bands is present on the second spectral domain ($\Delta\lambda < 800$ nm). For all the studied points, a trend can be detected, whereby increasing the length of the triangles on the arrays, the plasmon bands gets red-shifted and tend to be more intense. The results shown here are in agreement with previous studies reported for different designs,[14,23,39,46,58] where an increase on the size of the nanostructures tunes their optical properties to higher wavelengths.

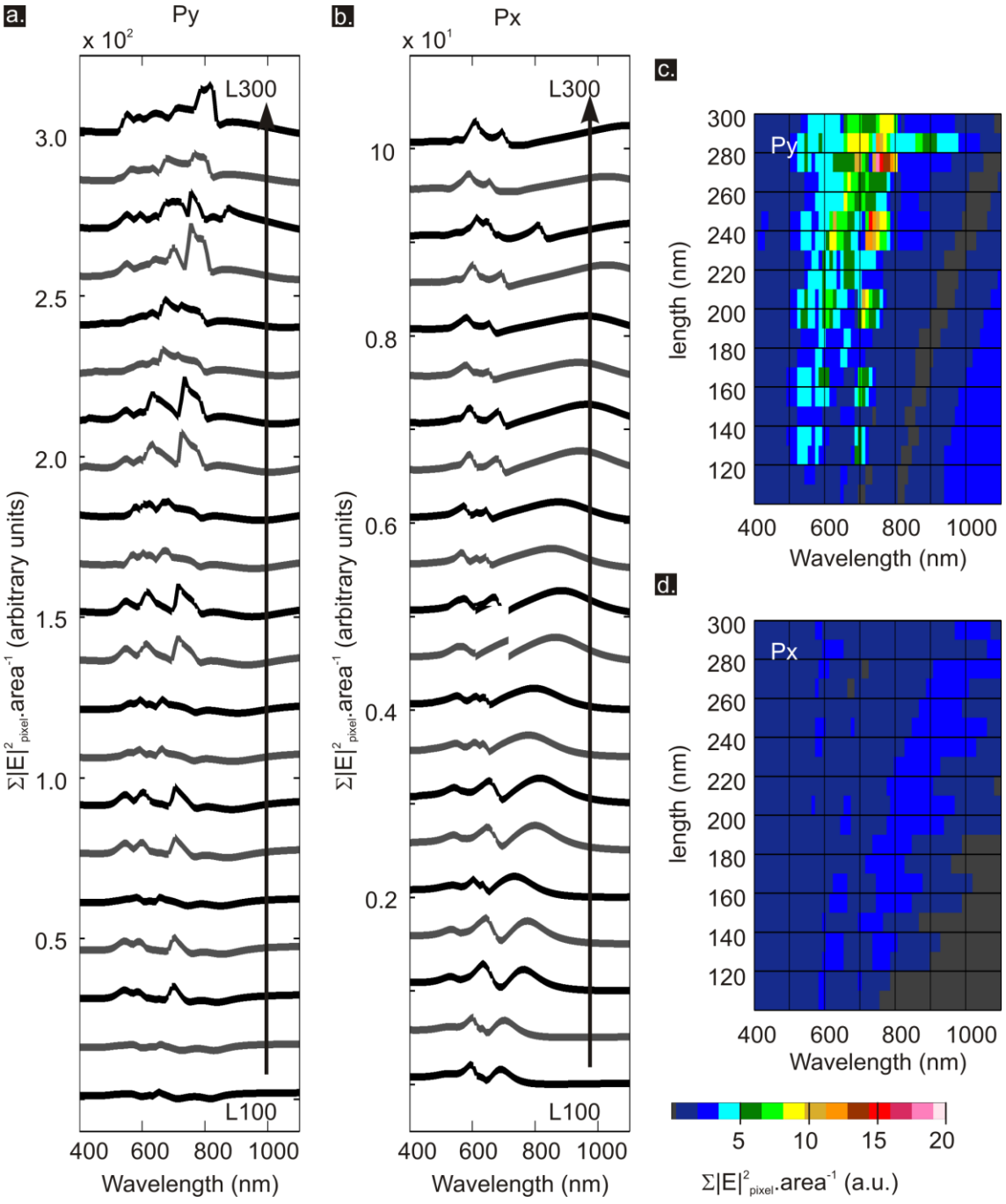

Figure 3.10. Calculated localized electric field spectra ($|E|^2/|E_0|^2$) for P4 when irradiated with a Py (a, c) and Px input (b, d). Spectra on A and B have been spatially correlated and the direction of the arrows indicates the increase on the length of the triangles in the array (L100-300 nm)

3.6. Conclusion

A comparison of the experimental and calculated extinction spectra of Fischer's patterns irradiated with a linearly polarized input was made, and the results showed a good agreement between both methods, as well as with the calculated total near-field intensity spectra.

The near-field intensity distribution of hexagonal arrays of gold nanotriangles on glass slides was calculated as a function of the triangle-length size, the irradiation wavelength and the direction of the linear polarization input, using FDTD simulations. The results obtained suggest that the localized electric field enhancement can be altered by modification of any of these parameters. In addition, the electric field components were also analyzed for one of the arrays and a depolarization effect was detected on the near-field intensity spectra as well as at the hot-spot regions.

The study of four specific areas on the hexagonal array lattice unit proves that the electric field enhancement is constricted to specific regions. More importantly, it suggests that this particular design, although highly used in surface-enhanced spectroscopy, is not necessarily the array with the highest electric field enhancement per unit area. Furthermore, the analysis of all the different arrays show that the strongest enhancement would be obtained when the sample is irradiated with a polarization parallel to the interparticle distance axis. The plasmon band regions can be modulated to higher wavelengths by making the length of the triangles longer.

Finally, even though the study of isolated triangles and their dimers has been reported before, those results are limited and not necessarily useful to correlate with other optical experiments performed on more complex arrays of triangles. The novelty of this work is

to emphasize the relation between the geometry, the size, and the polarization direction of a commonly used nanostructure, such as hexagonal arrays of nanotriangles.

3.7. References

(1) Cui, B.; Clime, L.; Li, K.; Veres, T.; *Nanotechnology,* **(2008)**, *19*, 145302.

(2) Banholzer, M. J.; Millstone, J. E.; Qin, L. D.; Mirkin, C. A.; *Chem. Soc. Rev.,* **(2008)**, *37*, 885.

(3) Gellini, C.; Muniz-Miranda, M.; Innocenti, M.; Carlà, F.; Loglio, F.; Foresti, M. L.; Salvi, P. R.; *Phys. Chem. Chem. Phys.,* **(2008)**, *10*, 4555.

(4) Hulteen, J. C.; Treichel, D. A.; Smith, M. T.; Duval, M. L.; Jensen, T. R.; Van Duyne, R. P.; *J. Phys. Chem. B,* **(1999)**, *103*, 3854.

(5) Le Ru, E. C.; Etchegoin, P. G.; Grand, J.; Félidj, N.; Aubard, J.; Lévi, G.; Hohenau, A.; Krenn, J. R.; *Curr. Appl. Phys.,* **(2008)**, *8*, 467.

(6) Liu, G. L.; Lee, L. P.; *Appl. Phys. Lett.,* **(2005)**, *87*, 074101.

(7) Haynes, C. L.; McFarland, A. D.; Zhao, L.; Van Duyne, R. P.; Schatz, G. C.; Gunnarsson, L.; Prikulis, J.; Kasemo, B.; Kall, M.; *J. Phys. Chem. B,* **(2003)**, *107*, 7337.

(8) Kelly, K. L.; Coronado, E.; Zhao, L. L.; Schatz, G. C.; *J. Phys. Chem. B,* **(2003)**, *107*, 668.

(9) Jensen, T.; Kelly, L.; Lazarides, A.; Schatz, G. C.; *J. Cluster Sci. ,* **(1999)**, *10*, 295.

(10) Tay, L.-L.; Hulse, J.; Kennedy, D.; Pezacki, J. P.; *J. Phys. Chem. C,* **(2010)**, *114*, 7356.

(11) Haes, A. J.; Van Duyne, R. P.; *J. Am. Chem. Soc.,* **(2002)**, *124*, 10596.

(12) Kneipp, K.; Kneipp, H.; Itzkan, I.; Dasari, R. R.; Feld, M. S.; *J. Phys.: Condens. Matter,* **(2002)**, *14*, R597.

(13) Willets, K. A.; Van Duyne, R. P.; *Annu. Rev. Phys. Chem.,* **(2007)**, *58*, 267.

(14) Atkinson, A. L.; McMahon, J. M.; Schatz, G. C. FDTD Studies of Metallic Nanoparticle Systems. In *Self-Organization of Molecular Systems*; Russo, N., Antonchenko, V. Y., Kryachko, E. S., Eds.; Springer Netherlands: Dordrecht, 2009; pp 11.

(15) Zhao, J.; Pinchuk, A. O.; McMahon, J. M.; Li, S.; Ausman, L. K.; Atkinson, A. L.; Schatz, G. C.; *Acc. Chem. Res. ,* **(2008)**, *41*, 1710.

(16) Mayer, K. M.; Hafner, J. H.; *Chem. Rev.,* **(2011)**, *111*, 3828.

(17) Mie, G.; *Annalen der Physik,* **(1908)**, *330*, 377.

(18) Yang, W. H.; Schatz, G. C.; Van Duyne, R. P.; *J. Chem. Phys.*, **(1995)**, *103*, 869.

(19) Zhao, L.; Zou, S.; Hao, E.; Schatz, G. C. Electrodynamics in computational chemistry. In *Theory and Applications of Computational Chemistry, the First Forty Years*; C. Dykstra, G. F., K. Kim, G. Scuseria, Ed.; Elsevier Science: Amsterdam, 2005; pp 47.

(20) McMahon, J. M.; Henry, A.-I.; Wustholz, K. L.; Natan, M. J.; Freeman, R. G.; Van Duyne, R. P.; Schatz, G. C.; *Anal. Bioanal. Chem.*, **(2009)**, *394*, 1819.

(21) Wong, M. F.; Picon, O.; Fouad Hanna, V.; *IEEE Transactions on Magnetics*, **(1995)**, *31*, 1618.

(22) Fischer, U. C.; Zingsheim, H. P.; *J. Vac. Sci. Technol.*, **(1981)**, *19*, 881.

(23) Chan, G. H.; Zhao, J.; Schatz, G. C.; Van Duyne, R. P.; *J. Phys. Chem. C*, **(2008)**, *112*, 13958.

(24) Haes, A. J.; Zou, S.; Schatz, G. C.; Van Duyne, R. P.; *J. Phys. Chem. B*, **(2004)**, *108*, 6961.

(25) Marquestaut, N.; Martin, A.; Talaga, D.; Servant, L.; Ravaine, S.; Reculusa, S.; Bassani, D. M.; Gillies, E.; Lagugné-Labarthet, F.; *Langmuir*, **(2008)**, *24*, 11313.

(26) Brockman, J. M.; Nelson, B. P.; Corn, R. M.; *Annu. Rev. Phys. Chem.*, **(2000)**, *51*, 41.

(27) Garcia de Abajo, F. J.; *Rev. Mod. Phys.*, **(2010)**, *82*, 209.

(28) Lazar, S.; Botton, G. A.; Zandbergen, H. W.; *Ultramicroscopy*, **(2006)**, *106*, 1091.

(29) Cinchetti, M.; Gloskovskii, A.; Nepjiko, S. A.; Schonhense, G.; Rochholz, H.; Kreiter, M.; *Phys. Rev. Lett.*, **(2005)**, *95*, 047601.

(30) Hartschuh, A.; *Angew. Chem., Int. Ed.*, **(2008)**, *47*, 8178.

(31) Hubert, C.; Bachelot, R.; Plain, J.; Kostcheev, S.; Lerondel, G.; Juan, M.; Royer, P.; Zou, S.; Schatz, G. C.; Wiederrecht, G. P.; *J. Phys. Chem. C*, **(2008)**, *112*, 4111.

(32) Hubert, C.; Rumyantseva, A.; Lerondel, G.; Grand, J.; Kostcheev, S.; Billot, L.; Vial, A.; Bachelot, R.; Royer, P.; Chang, S.; *Nano Lett.*, **(2005)**, *5*, 615.

(33) Juan, M. L.; Plain, J.; Bachelot, R.; Royer, P.; Gray, S. K.; Wiederrecht, G. P.; *ACS Nano*, **(2009)**, *3*, 1573.

(34) Juan, M. L.; Plain, J.; Bachelot, R.; Vial, A.; Royer, P.; Gray, S. K.; Montgomery, J. M.; Wiederrecht, G. P.; *J. Phys. Chem. A*, **(2009)**, *113*, 4647.

(35) Le Ru, E. C.; Galloway, C.; Etchegoin, P. G.; *Phys. Chem. Chem. Phys.*, **(2006)**, *8*, 3083.

(36) Dhawan, A.; Norton, S. J.; Gerhold, M. D.; Vo-Dinh, T.; *Opt. Express*, **(2009)**, *17*, 9688.

(37) Marty, R.; Baffou, G.; Arbouet, A.; Girard, C.; Quidant, R.; *Opt. Express*, **(2010)**, *18*, 3035.

(38) Payne, E. K.; Shuford, K. L.; Park, S.; Schatz, G. C.; Mirkin, C. A.; *J. Phys. Chem. B*, **(2006)**, *110*, 2150.

(39) Shuford, K. L.; Ratner, M. A.; Schatz, G. C.; *J. Chem. Phys.*, **(2005)**, *123*, 114713.

(40) Parsons, J.; Burrows, C. P.; Sambles, J. R.; Barnes, W. L.; *Journal of Modern Optics*, **(2010)**, *57*, 356.

(41) Draine, B. T.; Flatau, P. Arxiv 2008, 0809.0337v5.

(42) http://www.comsol.com/.

(43) http://www.ansoft.com/products/hf/hfss/.

(44) http://www.remcom.com/.

(45) http://www.lumerical.com/fdtd.php.

(46) Boneberg, J.; Koenig-Birk, J.; Muenzer, H. J.; Leiderer, P.; Shuford, K. L.; Schatz, G. C.; *Appl. Phys. A: Mater. Sci. Process.*, **(2007)**, *89*, 299.

(47) Palik, E. D. *Handbook of optical constants of solids II*, 2 ed.; Academic press: London, 1998; Vol. I.

(48) Lide, D. R. *Handbook of chemistry and physics*, 90 ed.; CRC Press: New York, 2009.

(49) Hao, E.; Schatz, G. C.; *J. Chem. Phys.*, **(2004)**, *120*, 357.

(50) Acker, W. P.; Schlicht, B.; Chang, R. K.; Barber, P. W.; *Optics Letters*, **(1987)**, *12*, 465.

(51) Félidj, N.; Grand, J.; Laurent, G.; Aubard, J.; Levi, G.; Hohenau, A.; Galler, N.; Aussenegg, F. R.; Krenn, J. R.; *J. Chem. Phys.*, **(2008)**, *128*, 094702.

(52) Etchegoin, P. G.; Galloway, C.; Le Ru, E. C.; *Phys. Chem. Chem. Phys.*, **(2006)**, *8*, 2624.

(53) Haynes, C. L.; Van Duyne, R. P.; *J. Phys. Chem. B*, **(2003)**, *107*, 7426.

(54) McFarland, A. D.; Young, M. A.; Dieringer, J. A.; Van Duyne, R. P.; *J. Phys. Chem. B*, **(2005)**, *109*, 11279.

(55) Foteinopoulou, S.; Vigneron, J. P.; Vandenbem, C.; *Opt. Express*, **(2007)**, *15*, 4253.

(56) Wei, H.; Hao, F.; Huang, Y.; Wang, W.; Nordlander, P.; Xu, H.; *Nano Lett.*, **(2008)**, *8*, 2497.

(57) Rang, M.; Jones, A. C.; Zhou, F.; Li, Z. Y.; Wiley, B. J.; Xia, Y.; Raschke, M. B.; *Nano Lett.*, **(2008)**, *8*, 3357.

(58) Nelayah, J.; Kociak, M.; Stéphan, O.; Geuquet, N.; Henrard, L.; García de Abajo, F. J.; Pastoriza-Santos, I.; Liz-Marzán, L. M.; Colliex, C.; *Nano Lett.*, **(2010)**, *10*, 902.

Chapter 4: Mapping Hot-Spots in Hexagonal Arrays of Metallic Nanotriangles with Azobenzene Polymer Thin Films[℘]

4.1. Introduction

Metallic structures organized at the nanoscale level are of particular interest since they can exhibit localized surface plasmon resonance (LSPR). Such surface plasmons can be used for a variety of applications like nanoscale spectroscopy, where the local electromagnetic field in the vicinity of a single or a pair of metallic particles can be enhanced by several orders of magnitude.[1] This results in platforms can be used for high sensitivity, high reproducibility of spectroscopic measurements, as shown for Raman measurements,[1-4] for the study of coherent vibrational oscillation mechanisms[5,6], for fluorescence enhanced measurements,[7,8] as well as for many other applications.[9]

As it was described in Chapter 2, hexagonal arrays of nanotriangles can be made by a variety of experimental methods such as nanosphere lithography,[10] Langmuir-Blodgett film,[11] or EBL.[12,13] It has been predicted and described in Chapter 3 that arrangements of triangular nanostructures can enhanced the incoming electromagnetic field very efficiently in localized areas defined as hot-spots. In specific regions, often composed of metallic dimers separated by a small gap (1-10 nm), the ideal conditions are met when the surface plasmon is confined to a small volume.[14,15] However, it is generally difficult to have control over the fabrication and the distribution of such near-field enhancement effects.

[℘] Reproduced with permission from [*J. Phys. Chem. C* (**2011**), 115, 15318.] Copyright 2011 American Chemical Society.

As it was described in the previous chapter, the experimental detection of the LSPR properties at the near-field is not an easy task. The nature of these hot-spots is evanescent and its magnitude decays exponentially with distance, requiring most of the time the use of an electron microscope or a near-field optical microscope (NSOM) to study the electric field distribution around the nanostructures. However, both techniques present some limitations. Even though the electron-microscope-based technology has a good spatial resolution,[16] it requires a conductive material; and in the case of NSOM, the probe has to be so close to the surface that it ends up altering the surroundings and altering the optical properties of the sample.[16-18] A convenient and elegant method has been recently suggested ,[19,20] that involves the use of photosensitive azobenzene polymer thin films to observe the near-field distribution over the nanostructure by studying the topographical deformation of the film upon irradiation.

Herein, a similar approach is used to study the electromagnetic coupling effect between nanotriangles organized in a hexagonal array. More specifically, the photoinduced topographical deformation of an azobenzene polymer by either silver or gold platforms made by EBL is reported. The irradiation was set to 532 nm to be resonant with the azobenzene moieties electronic transition ($\lambda_{max} \approx 500$ nm). The surface deformation was probed by AFM, and the topographic changes were compared with the total, $|E|^2$, as well the individual polarized components, $|E_x|^2$, $|E_y|^2$, and $|E_z|^2$, of the field that were calculated in the near-field vicinity of the plasmonic nanostructure. Considering the symmetry of the lattice unit, the near-field components for the different orientation of the bow tie pairs with respect to the polarization of the input light were studied. Finally, this chapter shows the polarized nature of the electric field components responsible of the local enhancement. First, a brief description is given to explain the photochemical behavior of azobenzene polymers and how they can be of interest to detect the near-field intensity distribution in the vicinity of metallic nanostructures.

4.2. Azobenzene polymers

4.2.1. Photochemical process

Functionalized polymers with pendent azobenzene groups, such as poly{4'-[[[2-(methacryloyloxy)ethyl]ethyl]amino]-4nitroazobenzene-co-methyl methacrylate} (p(DR1M-*co*-MMA) with 11% molar azobenzene moieties in **Figure 4.1.a**, are particularly well suited to study the electric field intensity distribution since they are self-developing photopolymers. When irradiated with a linearly polarized light, which wavelength matches the absorption of the azobenzene moiety (**Figure 4.1.b**),[21] a stable surface topography change is observed at room temperature without any developing step.

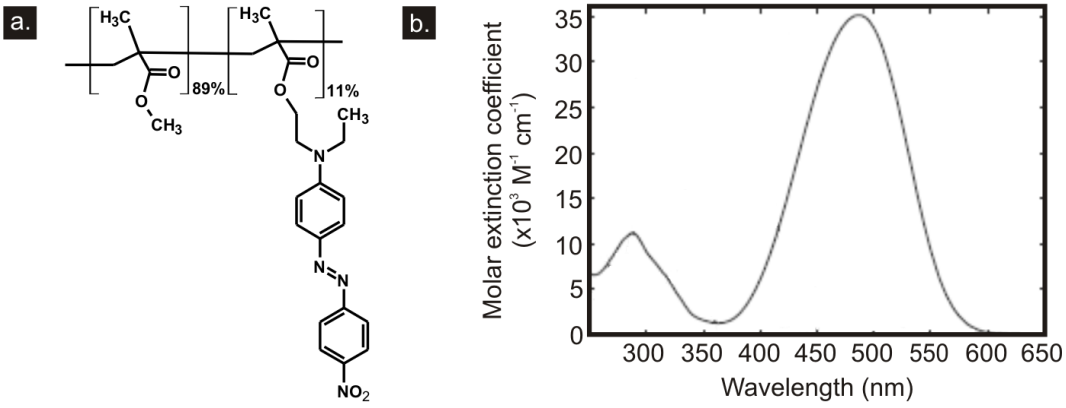

Figure 4.1. Chemical structure of p(DR1M-co-MMA) 11% (a) and absorption spectrum of the azobenzene moiety (b).[21]

Several review articles and theoretical studies have focused on the photo-physical aspects of light driven motion in azobenzene polymers.[22,23] Although the parameters that control efficient mass transport are well defined, the origin of the strong force needed to generate large and stable surface deformation is not fully understood, and all the different models fail in some aspects.[24-30] It is generally admitted that the amplitude of surface deformation in amorphous polymers is regulated by two factors: the intensity of the electromagnetic field and thepolarization of the source. When a flat surface is irradiated by a gradient of

light intensity, a photoinduced deformation of the surface is observed. The polymer migrates in a direction along the polarization vector from area of large intensity towards areas of small intensities as demonstrated in **Figure 4.2** for an irradiation with a linearly polarized focused beam onto a thin film of p(DR1M-*co*-MMA).

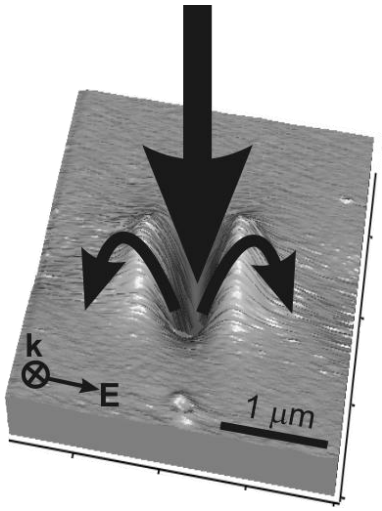

Figure 4.2. Surface Modification of a thin film of p(DR1M-co-MMA) after irradiation at 532 nm with a 100 mW/cm^2 focalized and linearly polarized Gaussian beam (objective used 50x, N.A=0.63).

In addition, such an effect also depends on the nature of the azobenzene derivative matrix, thus showing a different behavior in sol-gels, liquid crystalline or amorphous polymers that contains azobenzene chromophores.[31]

Nevertheless the photochemistry of the azobenzene chromophore is well understood, and is among the cleanest photo-chemically induced reactions. When irradiated by a linearly polarized light, an angular hole burning process due to a trans$_{//}$-cis-trans$_{\perp}$ photo-isomerisation is followed by an angular reorientation of the azobenzene moieties that undergo perpendicular reorientation with respect to the polarization of the impinging field

(**Figure 4.3**).[22,32,33] This leads to large values of linear dichroism or birefringence for polymers functionalized with azobenzene moieties.[34,35]

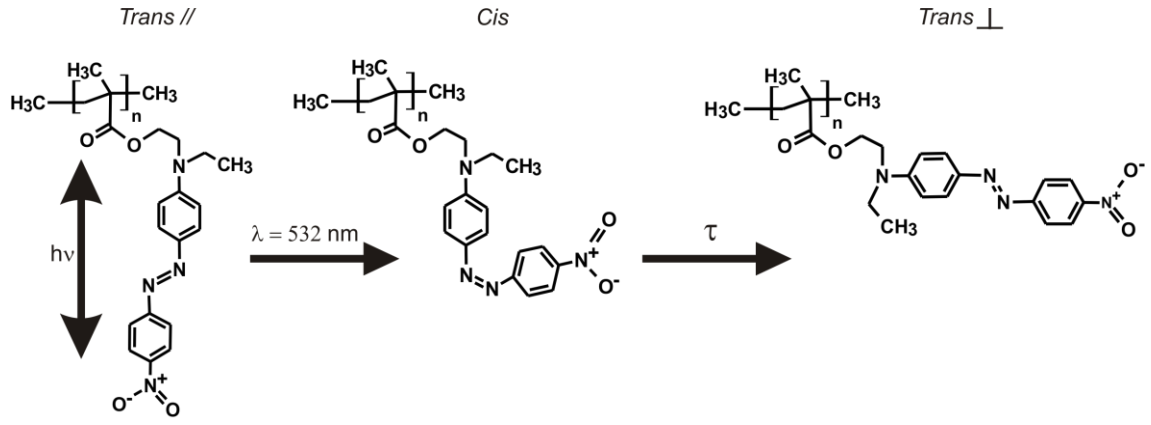

Figure 4.3. Photochemical induced reaction of azobenzene moieties.

Based on this observation, periodic surface relief gratings were successfully inscribed by several groups over the past decade, using a large variety of materials containing azobenzene molecules.[19,31,36-39] Such surface migration can then be probed easily by AFM giving an indication of the intensity distribution of the optical field.

4.2.2. Azobenzene polymer as a tool for near-field detection

In an elegant approach, led by Hubert,[19,40] and later by Juan and coworkers[20,41] the near-field around a variety of metallic nanostructures, including isolated bow tie assemblies (**Figures 4.4.a,b**) was studied. The total field and its components (**Figure 4.4.c,h**) were simulated and correlated with the photo-induced motion of an azobenzene polymer thin film deposited over a metallic nanostructure. The thin film is irradiated with a wavelength that matches both the electronic resonance of the azobenzene moieties and the LSPR band of the nanostructures. In their work they stated that the intensity of the total electric field ($|E_{tot}|^2$) comes just from the sum of these in-plane polarized components parallel to the

polarized input and out-of-plane components (**Figures 4.4.g,h**), with no contribution from the in-plane component perpendicular to the polarized input. Then they were able to detect a topographical deformation around the bow tie that correlates with the areas of high electric field intensity coming from the in-plane electric field component parallel to the polarization of the incoming beam (**Figures 4.4c,d**); while the out-of-plane component ($|E_z|^2$ in **Figures 4.4.e,f**), tends to accumulate the polymer on top of the triangles. This effect that can only be detected by improving the topographical contrast on the AFM scans.

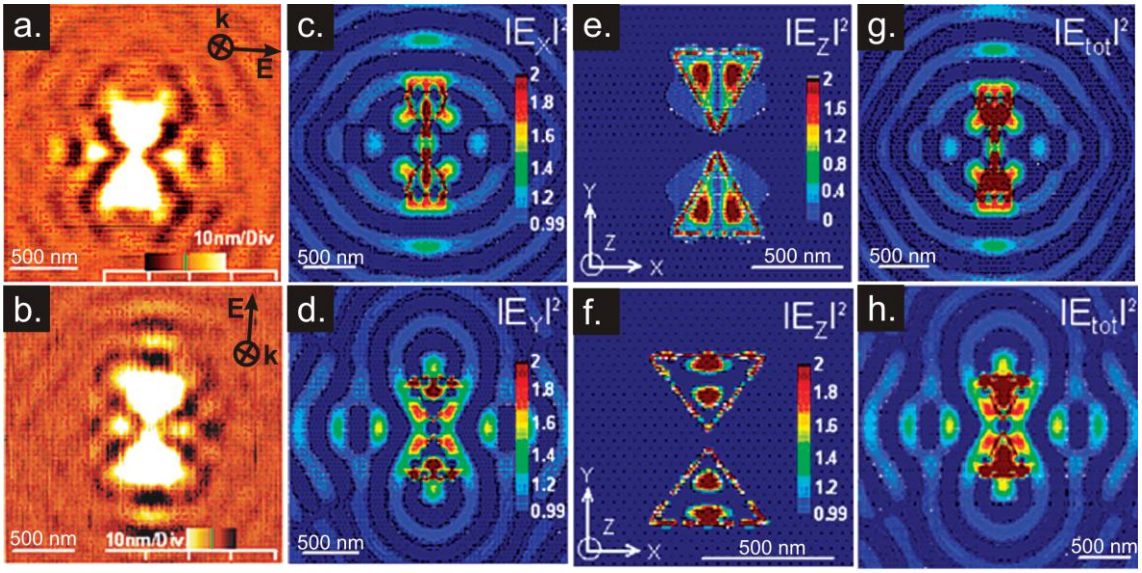

Figure 4.4. AFM image of a silver bow tie assembly coated with an azobenzene polymer thin film after being irradiated at 532 nm with a linearly polarized beam perpendicular (a) and parallel (b) to the interparticle distance axis of the dimer. Their respective calculated near-field intensity distribution ($|E_{x/y}|^2$, $|Ez|^2$, $|Etot|^2$) are also shown in the same row (c-h).[19]

Although the role of the out-of-plane field might be contradictory with the proposed correlation where a topographical minimum represents regions of with intensity maxima, the results can be interpreted by using a schematic representation of the process (**Figures**

4.5.a, b) where depending on the polarization it is possible to have a topographical minima under the effect of an in-plane polarized component (**Figure 4.5.a**) and an elevation in the case of the out of plane component (**Figure 4.5.b**).

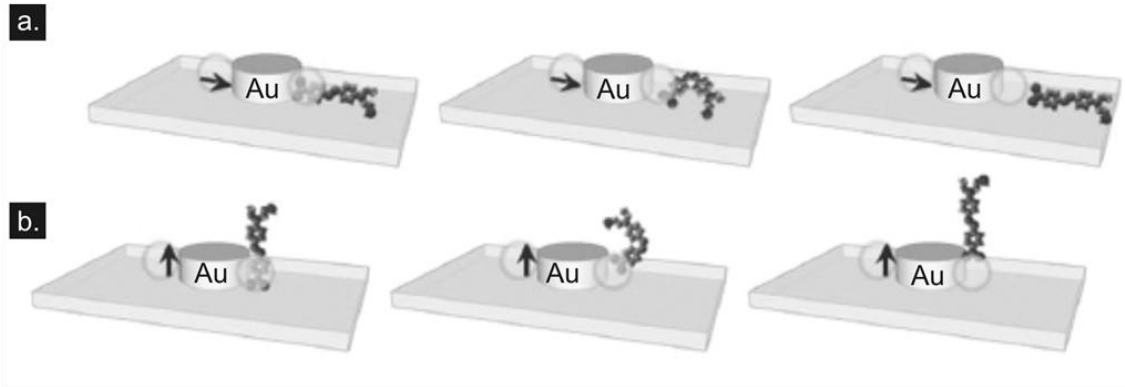

Figure 4.5. Schematic representation of the molecular migration of azobenzene polymer under the effect of an in-plane (a) and an out-of-plane (b) polarized field. [42]

Such topographical deformations can therefore be used to map the near-field properties of metallic nanostructures, specifically the field distribution in the vicinity of the hexagonal array of nanotriangles at the near-field level. Such results can then be correlated with numerical calculations performed on similar structures under the same irradiation conditions.

4.3. Experimental methods

4.3.1. Calculations

The electric field distribution for a hexagonal array of silver and gold nanotriangles of similar dimensions was calculated using the finite-difference time domain method, FDTD Solutions from Lumerical. The calculations were set up as a three dimensional system with a 5 nm resolution grid, for 500 femtoseconds, and including the appropriate

boundary conditions. A plane wave source was chosen at a 532 nm working wavelength, with a propagation axis perpendicular to the plane of the platform, and with a polarization parallel to the bow tie axis. The dielectric constant of the glass (silicon dioxide), silver and gold were described by Palik[43] and the CRC[44] values, provided in the material database from the software. The calculation of the total electric field intensity ($|E|^2$) and its distribution was obtained from the sum of its polarized components ($|E_x|^2 + |E_y|^2 + |E_z|^2$), and the intensity map of the surface was calculated 10 nm above the surface, or at specific regions to get the different cross section intensity maps.

4.3.2. Preparation of nanotriangle arrays

A detailed description of the fabrication process can be found in Chapter 2. In short, samples were fabricated by EBL on VistaVision™ microscope cover glass slides, and the revealing patterns consist of an hexagonal arrangement of metallic nanotriangles with typical dimensions of 320±20nm for the triangle base size, 115±15nm for the distance between facing nanotriangles and with a thickness of Au or Ag of 40 ± 5 nm, as shown in the SEM image of such platform (**Figure 4.6*)***.

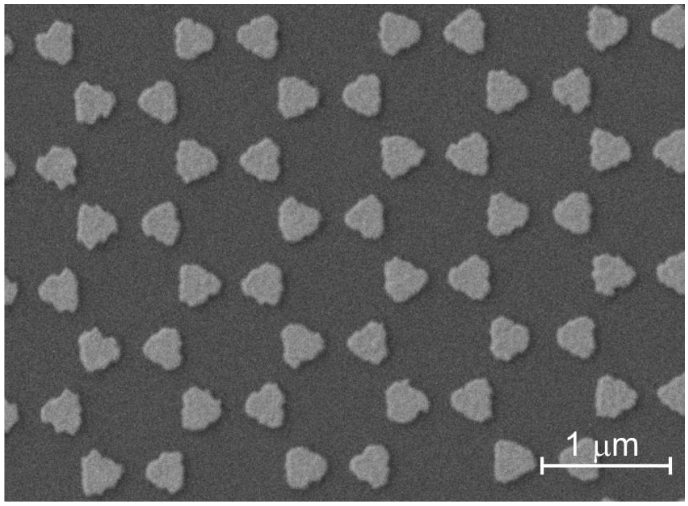

Figure 4.6. SEM image of a hexagonal array of gold nanotriangles (length: 327±20 nm, gap: 116±15 nm, metallic thickness: 40±5 nm).

4.3.3. Azobenzene polymer photoinduced migration

A solution of (p(DR1M-*co*-MMA)) with 11% molar in chromophore was spin coated (2500 rpm) onto the patterned substrates to obtained a film with a 60±2 nm thickness. Then, the sample was irradiated with a parallel Gaussian beam, which was linearly polarized light parallel to a given bow tie axis at 532 nm for 15 minutes and with an intensity of 100±5 mW/cm^2. The beam was facing the interface composed of the azobenzene polymer thin film/ metallic nanostructure.

4.3.4. Surface characterization

AFM scans were collected on a NanoWizard® II Bioscience AFM (JPK Instruments Inc.) in intermittent mode using a NCL cantilever (k=48 N/m, Nano World Inc.) before coating the sample with the azobenzene polymer as well as before and after the sample was irradiated. For each sample, AFM scans were performed on several surface positions to check the surface uniformity.

4.4. Results and discussion

4.4.1. Electric field distribution

The total electric field distribution was calculated for a periodic array of gold and silver nanotriangles. More specifically, the electric field enhancement was calculated around the metallic structures, as shown in the intensity map 10 nm above the metallic structure (**Figure 4.7, left side column**), and along the longitudinal cross sections of the bow tie axis parallel (middle column) and off-axis (60° tilt, right-side column) with respect to the orientation of the polarized beam. The distribution of the total electric field around gold (**Figure 4.7.a**) and silver (**Figure 4.7.b**) nanotriangles highlights hot-spots at the edges of the metallic structures, and more specifically at the vertices of the triangles. It is known[45] that the most intense regions for this periodic array will be predominantly located at the apexes positioned along the bow tie axis parallel to the incoming linearly polarized

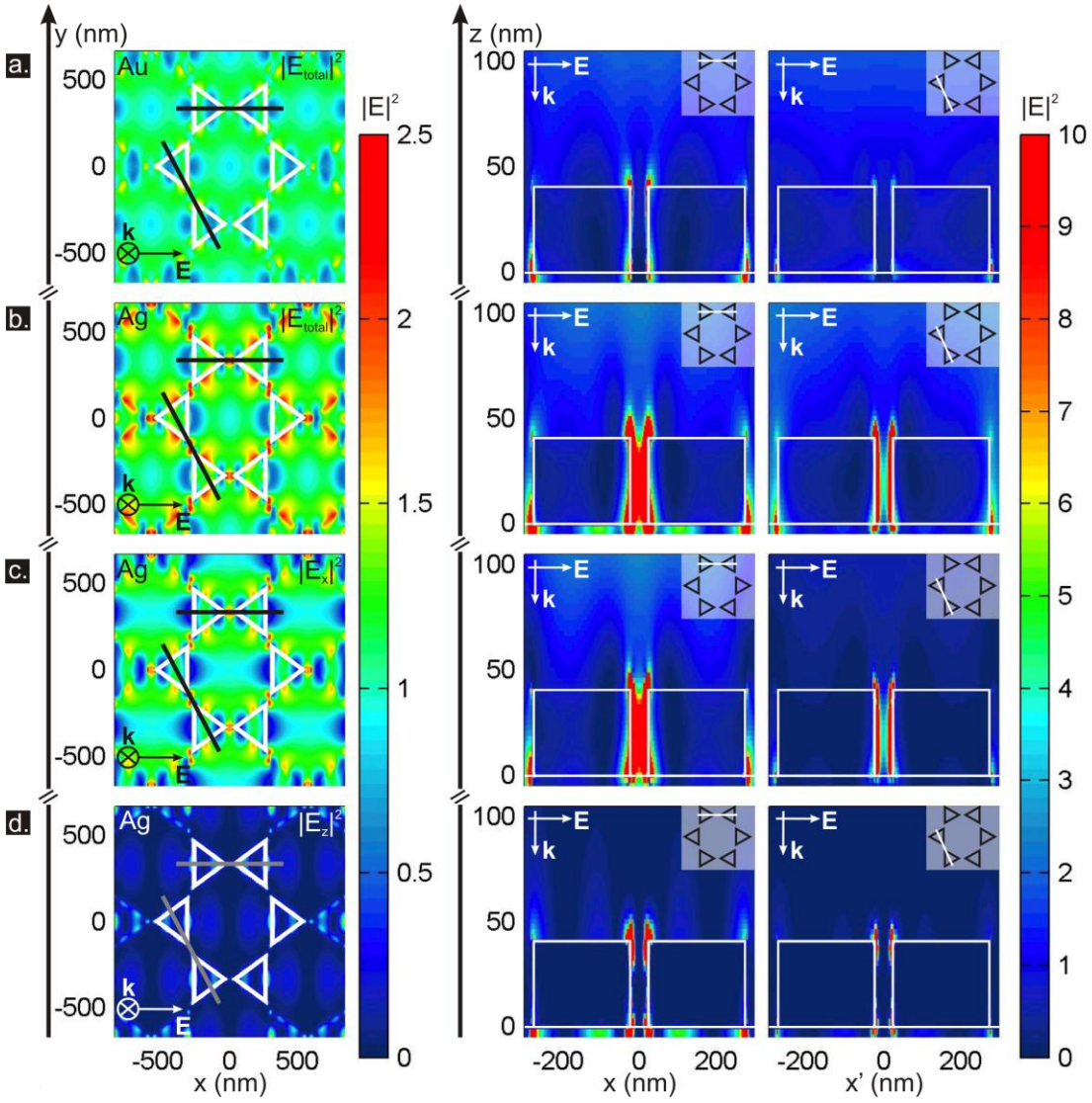

Figure 4.7. Calculated electric field distribution of hexagonal array of gold (a) and silver (b-d) nanotriangles irradiated with a linearly polarized beam parallel to the bow tie axis at 532 nm. The left side column represents the electric field distribution calculated 10 nm above the metallic surface, while the other two columns show the cross section intensity maps of these structures, one parallel to the polarization of the incoming beam (middle column) and another one with a 60 degrees rotation (right side column), as shown on the inset. In the case of silver, the in-plane component parallel to the bow tie axis (c), as well as the out-of-plane electric field component (d) are also illustrated.

electric field. This observation is made for both gold and silver arrays but the silver pattern shows larger intensity distribution at 532 nm confirming that the LSPR of silver is closer to the impinging light frequency than the LSPR of the gold structure.[46] Also, the irradiation wavelength is in resonance with the azobenzene polymer electronic transition.

Furthermore, the calculated electric field distribution was also studied in terms of the different electric field components. The silver nanoarray was used to explain the contribution of the different components as it is the one with higher electric field intensity. The total electric field is the result of the in-plane component parallel to the incoming linearly polarized beam ($|E_x|^2$, **Figure 4.7.c**), as well as an out-of-plane component ($|E_z|^2$, **Figure 4.7.d**). When the electric field distribution of these two components is compared, it is possible to detect that $|E_x|^2$ is more dispersed than $|E_z|^2$. The cross section intensity maps show how the in-plane component of the electric field is distributed along the edges of the nanostructure, while the out-of-plane component is localized just at the corners of these structures.

4.4.2. Topographic analysis

The AFM scans of the samples coated with p(DR1M-*co*-MMA), before and after irradiation at 532 nm are shown in **Figures 4.8.a,b**, respectively. After deposition of the thin film, it was still possible to observe the topographic features of the metallic nanostructures (**Figure 4.8.a**). Topographical differences at specific regions around the pattern are detected after irradiation. To facilitate the observation of these dissimilarities, the color scale in both AFM scans has been normalized within a 20 nm range. Moreover, to confirm that these surface deformations are not the result of artifacts coming from the AFM scan, several areas were analyzed and compared to scans obtained with an orthogonal scan direction of the AFM tip. This topographical change results from a molecular migration of the coated azobenzene polymer, which is sensitive to the electric field distribution around the metallic structures. As it was described earlier, this azobenzene polymer thin film can be used to detect the near-field intensity distribution by

studying the changes in the topography, where the surface minima correspond to the electric field intensity maxima. As a result, it is possible to determine an electric field intensity gradient, where the polymer moves from regions of large electromagnetic field intensity towards regions of lower intensity.

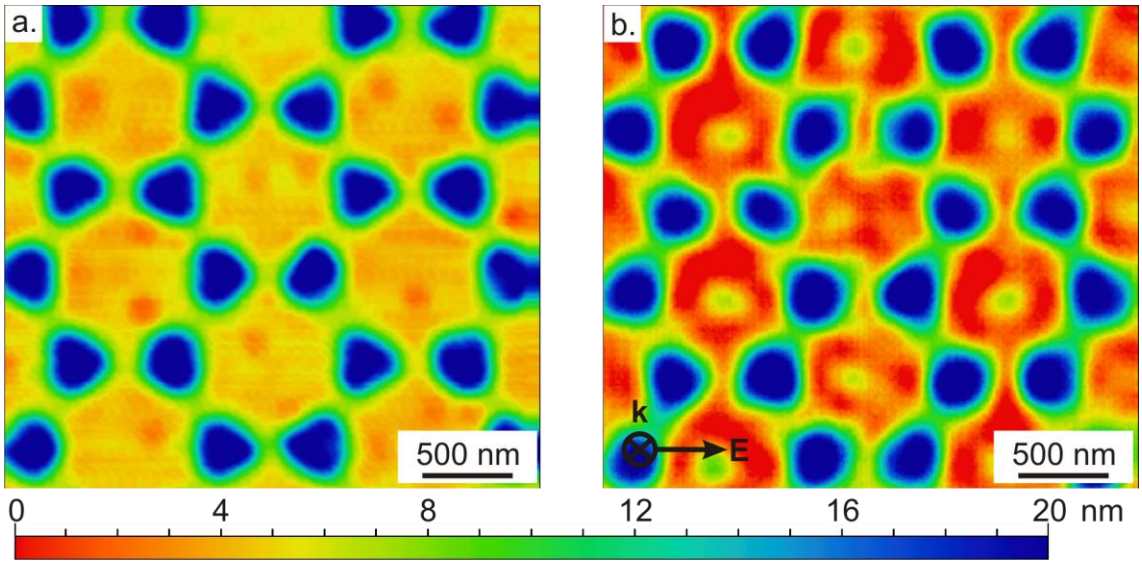

Figure 4.8. AFM images of a periodic array of silver nanotriangles coated with pDR1M thin film before (a) and after (b) being irradiated with a linearly polarized laser beam at 532 nm parallel to the bow tie axis.

These changes were analyzed in detail for both silver (**Figure 4.9**, top set) and gold (**Figure 4.9**, bottom set) coated nanostructures. When the AFM scans before (**Figures 4.9.a,c**) and after (**Figures 4.9b,d**) irradiation were compared, it is possible to detect these topographical minima and maxima described before. The comparison of their cross sections suggests that the topography of the coated array gets mainly modified at the center of the hexagonal lattice (**Figure 4.9.e,f**). Weaker changes in topography were observed in the gaps formed by the bow ties assemblies mainly for the silver nanotriangles oriented along the input polarization direction (**Figure 4.9.g**). This slight increase of the polymer thickness over the metallic triangles can be observed by AFM

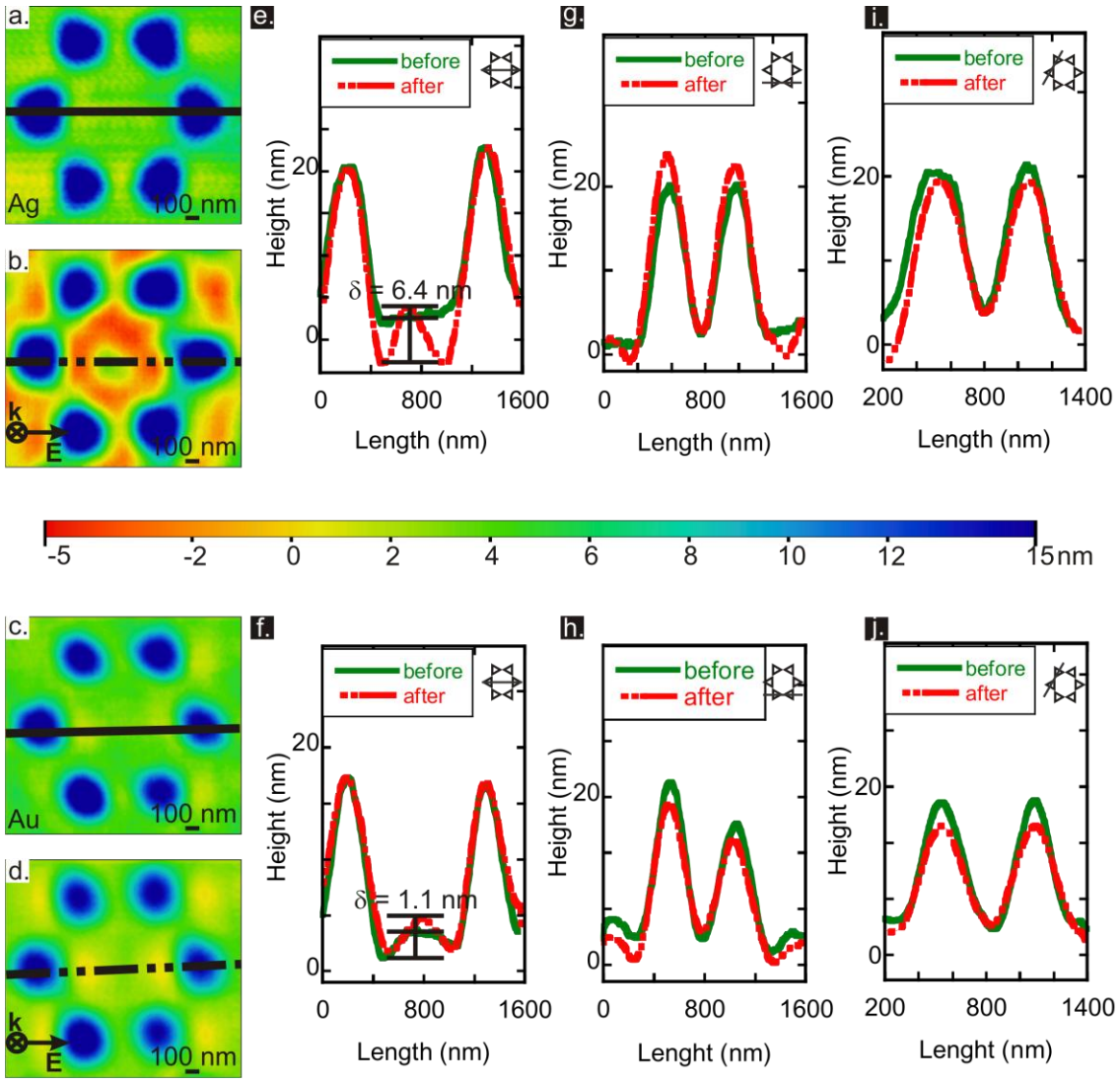

Figure 4.9. AFM image of a hexagonal array of silver (top set) and gold (bottom set) nanotriangles coated with pDR1M before (a, c) and after irradiation (b, d). The cross section profiles (e) and (f) show the change in topography before (green) and after (red) irradiation for silver and gold at the center of the lattice, respectively. The cross sections profiles (g) and (h) show the change of topography along the bow tie assemblies parallel to the input polarized light, as shown in the inset; and the profiles (i) and (j) show the change of topography along the bow tie assemblies oriented at 60° with respect to the direction of the linearly polarized light, as shown in the inset.

evidencing the mass transport of azopolymer from high intensity regions to lower intensity regions confirming the intensity profile shown in **Figure 4.7.b**. However such observation is not significant for gold patterns (**Figure 4.9.h**) nor for bow ties oriented at 60° with respect to the direction of the linearly polarized irradiation beam (**Figures 4.9.i, j**). More importantly, the difference in the height gradient (δ) measured at the center of the hexagonal lattice (**Figures 4.9.e, f**), allows one to quantify the topographical change. In the case of silver, the difference in height gradient is approximately 6.4 ±0.3 nm (**Figure 4.9.e**); while for the gold nanostructures δ is 1.1 ±0.3 nm (**Figure 4.9.f**). Such difference can be explained by analyzing the calculated electric field distribution cross section of these two arrays.

As mentioned earlier, the silver array presents an electric field distribution of higher intensity than the gold nanostructures (**Figures 4.7.a,b**). Therefore, it is not surprising that the azobenzene polymer surrounding the silver structures goes through a more drastic change in their topography, compared to those with gold nanostructures for a given irradiation wavelength. In addition, the silver array exhibits a more pronounced depression on the closest regions to the metallic triangles; while in the case of gold, the deformation tends to elevate the surface close to the center of the lattice unit.

The effect may be interpreted if the cross section intensity profile from base to base of the nanotriangles is analyzed (**Figure 4.10**). In the case of the gold array (**Figure 4.10.a**) the hot-spots are localized at the corners of the structures. In silver nanotriangles, the same hot-spots (**Figure 4.10.b**) tend to be more intense promoting the molecular migration of the polymer away from these areas towards regions with minimum electric field. More specifically, it appears that mainly the Ex component drives the polymer migration towards the center of the lattice as seen for Au and Ag in **Figure 4.10.c** and **Figure 4.10.d**, respectively.

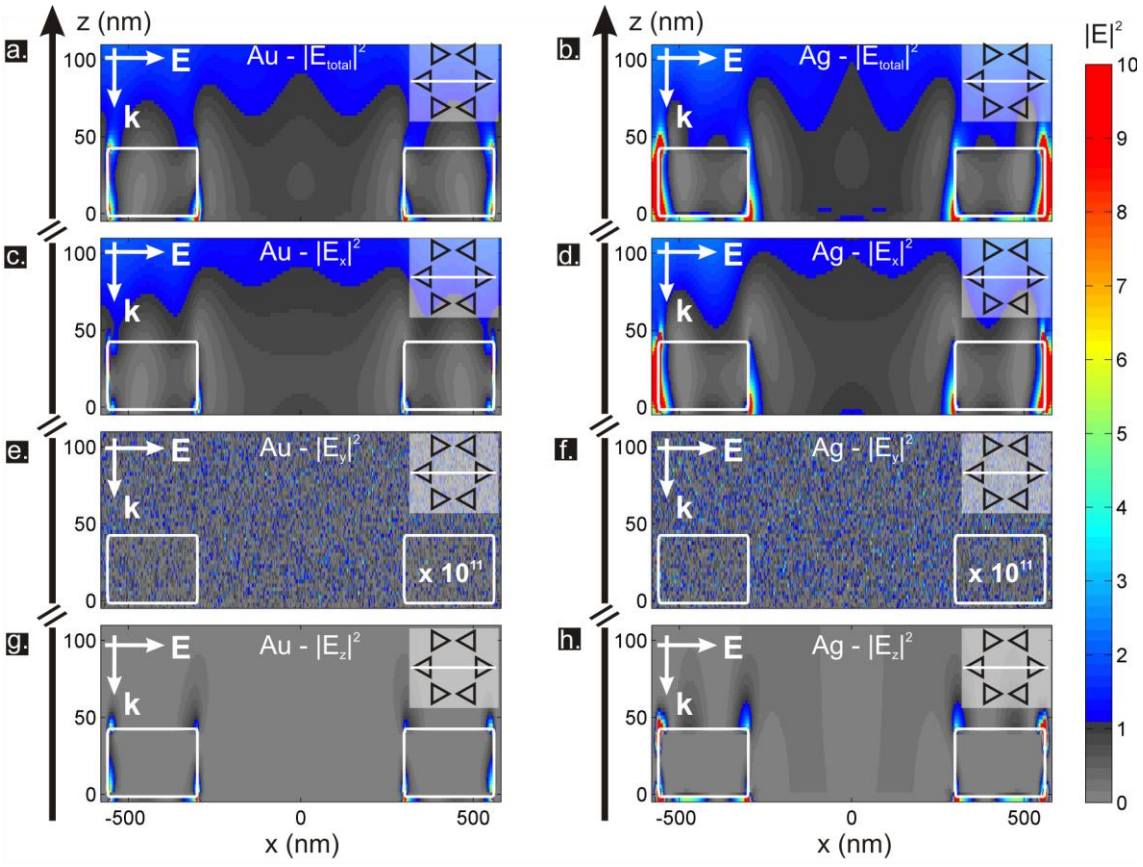

Figure 4.10. Calculated electric field distribution cross sections for gold (left side) and for silver (silver) hexagonal array of nanotriangles along the center of the lattice unit, when irradiated with a linearly polarized beam is polarized along the X direction, as shown on the insets. The total (a, b) and partial field components: $|E_x|^2$ (c, d), $|E_y|^2$ (e, f), $|E_z|^2$ (g, h) are shown.

The Ey field contribution is extremely weak and does not contribute to any sort of local hot-spot (**Figures 4.10.e,f**). The amplitude and the variation of Ez along the cross section (**Figures 4.10g,h**) are also larger for silver compared to gold but are mostly confined around the metallic structure. In addition such calculations show that the center of the gold lattice unit presents a region where there is an electric field is smaller than for the silver nanotriangles (**Figures 4.10.a-d**). This central region would also be ideal to localize

the migrated azobenzene polymer but it appears that the overall effect comes mainly from the gradient of the total field (**Figures 4.10.a,b**) which is a combination of both Ex and Ez components. In the case of silver, the total field shows larger variations along the X and the Z directions promoting a more efficient photo-induced migration of the photopolymer from the base of the triangles towards the center of the lattice (P1 in **Figure 3.2**) where the field is weak.

4.5. Conclusions

Topographical deformation of azobenzene polymer thin films can be used in the experimental detection of near-field distribution around metallic nanostructures. This chapter has shown the distribution of the electric field and its polarized components in hexagonal array of nanotriangles inscribed in glass and made by electron beam lithography by using an azobenzene polymer thin film. Surface photoinduced deformation on the thin film of azobenzene polymer was observed and is consistent with the localization of the electric field.

Larger surface deformation was observed when the irradiation wavelength matches both the LSPR band of the metallic structure and the azobenzene moiety absorption, and even larger enhancements are observed when the beam is polarized along the axis of two facing triangles.

Due to the field gradient in the laterals direction with respect to the platform surface, trapping and localization of small particles within the center of such hexagonal lattice could be performed using higher irradiances.

4.6. References

(1) Haynes, C. L.; Van Duyne, R. P.; *J. Phys. Chem. B,* **(2003)**, *107*, 7426.

(2) Hulteen, J. C.; Van Duyne, R. P.; *J. Vac. Sci. Technol., A,* **(1995)**, *13*, 1553.

(3) Haynes, C. L.; McFarland, A. D.; Smith, M. T.; Hulteen, J. C.; Van Duyne, R. P.; *J. Phys. Chem. B,* **(2002)**, *106*, 1898.

(4) Gibson, K. F.; Correia-Ledo, D.; Couture, M.; Graham, D.; Masson, J.-F.; *Chem. Comm.,* **(2011)**, *47*, 3404.

(5) Huang, W.; Qian, W.; El-Sayed, M. A.; *Nano Lett.,* **(2004)**, *4*, 1741.

(6) Huang, W.; Qian, W.; El-Sayed, M. A.; Ding, Y.; Wang, Z. L.; *J. Phys. Chem. C,* **(2007)**, *111*, 10751.

(7) Li, J. F.; Huang, Y. F.; Ding, Y.; Yang, Z. L.; Li, S. B.; Zhou, X. S.; Fan, F. R.; Zhang, W.; Zhou, Z. Y.; Wu, D. Y.; Ren, B.; Wang, Z. L.; Tian, Z. Q.; *Nature,* **(2010)**, *464*, 392.

(8) Moula, G.; Aroca, R. F.; *Anal. Chem.,* **(2011)**, *83*, 284.

(9) König, T.; Goldenberg, L. M.; Kulikovska, O.; Kulikovsky, L.; Stumpe, J.; Santer, S.; *Soft Matter,* **(2011)**, *7*, 4174.

(10) Hulteen, J. C.; Treichel, D. A.; Smith, M. T.; Duval, M. L.; Jensen, T. R.; Van Duyne, R. P.; *J. Phys. Chem. B,* **(1999)**, *103*, 3854.

(11) Marquestaut, N.; Martin, A.; Talaga, D.; Servant, L.; Ravaine, S.; Reculusa, S.; Bassani, D. M.; Gillies, E.; Lagugné-Labarthet, F.; *Langmuir,* **(2008)**, *24*, 11313.

(12) Billot, L.; Lamy de la Chapelle, M.; Grimault, A. S.; Vial, A.; Barchiesi, D.; Bijeon, J. L.; Adam, P. M.; Royer, P.; *Chem. Phys. Lett.,* **(2006)**, *422*, 303.

(13) Galarreta, B. C.; Harté, E.; Marquestaut, N.; Norton, P. R.; Lagugné-Labarthet, F.; *Phys. Chem. Chem. Phys.,* **(2010)**, *12*, 6810.

(14) Etchegoin, P. G.; Galloway, C.; Le Ru, E. C.; *Phys. Chem. Chem. Phys.,* **(2006)**, *8*, 2624.

(15) Foteinopoulou, S.; Vigneron, J. P.; Vandenbem, C.; *Opt. Express,* **(2007)**, *15*, 4253.

(16) Garcia de Abajo, F. J.; *Rev. Mod. Phys.,* **(2010)**, *82*, 209.

(17) Cinchetti, M.; Gloskovskii, A.; Nepjiko, S. A.; Schonhense, G.; Rochholz, H.; Kreiter, M.; *Phys. Rev. Lett.,* **(2005)**, *95*, 047601.

(18) Hartschuh, A.; *Angew. Chem., Int. Ed.,* **(2008)**, *47*, 8178.

(19) Hubert, C.; Bachelot, R.; Plain, J.; Kostcheev, S.; Lerondel, G.; Juan, M.; Royer, P.; Zou, S.; Schatz, G. C.; Wiederrecht, G. P.; *J. Phys. Chem. C,* **(2008)**, *112*, 4111.

(20) Juan, M. L.; Plain, J.; Bachelot, R.; Royer, P.; Gray, S. K.; Wiederrecht, G. P.; *ACS Nano,* **(2009)**, *3*, 1573.

(21) Griffiths, J.; *Chem. Soc. Rev.,* **(1972)**, *1*, 481.

(22) Natansohn, A.; Rochon, P.; *Chem. Rev.,* **(2002)**, *102*, 4139.

(23) Nakatani, K.; Delaire, J. A.; *Chem. Mater.,* **(1997)**, *9*, 2682.

(24) Bian, S.; Williams, J. M.; Kim, D. Y.; Li, L.; Balasubramanian, S.; Kumar, J.; Tripathy, S.; *J. Appl. Phys.,* **(1999)**, *86*, 4498.

(25) Kumar, J.; Li, L.; Jiang, X. L.; Kim, D.-Y.; Lee, T. S.; Tripathy, S.; *Appl. Phys. Lett.,* **(1998)**, *72*, 2096.

(26) Pedersen, T. G.; Johansen, P. M.; Rømer Holme, N. C.; Ramanujam, P. S.; Hvilsted, S.; *J. Opt. Soc. Am. B,* **(1998)**, *15*, 1120.

(27) Lefin, P.; Fiorini, C.; Nunzi, J.-M.; *Pure Appl. Opt.,* **(1998)**, *7*, 71.

(28) Tanchak, O. M.; Barrett, C. J.; *Macromolecules,* **(2005)**, *38*, 10566.

(29) Yager, K. G.; Barrett, C. J.; *Macromolecules,* **(2006)**, *39*, 9320.

(30) Pedersen, T. G.; Johansen, P. M.; Holme, N. C. R.; Ramanujam, P. S.; Hvilsted, S.; *Phys. Rev. Lett.,* **(1998)**, *80*, 89.

(31) Fabbri, F.; Garrot, D.; Lahlil, K.; Boilot, J. P.; Lassailly, Y.; Peretti, J.; *J. Phys. Chem. B,* **(2011)**, *115*, 1363.

(32) Sekkat, Z.; Dumont, M.; *Synth. Met.,* **(1993)**, *54*, 373.

(33) Lagugné-Labarthet, F.; Bruneel, J.-L.; Buffeteau, T.; Sourisseau, C.; Huber, M. R.; Zilker, S. J.; Bieringer, T.; *Phys. Chem. Chem. Phys.,* **(2000)**, *2*, 5154.

(34) Priimagi, A.; Lindfors, K.; Rochon, P.; Kaivola, M.; *ACS Appl. Mater. Interfaces,* **(2009)**, *1*, 1182.

(35) Lagugné-Labarthet, F.; Freiberg, S.; Pellerin, C.; Pézolet, M.; Natansohn, A.; Rochon, P.; *Macromolecules,* **(2000)**, *33*, 6815.

(36) Rochon, P.; Batalla, E.; Natansohn, A.; *Appl. Phys. Lett.,* **(1995)**, *66*, 136.

(37) Ishow, E.; Camacho-Aguilera, R.; Guérin, J.; Brosseau, A.; Nakatani, K.; *Adv. Funct. Mater.,* **(2009)**, *19*, 796.

(38) Jiang, X. L.; Li, L.; Kumar, J.; Kim, D. Y.; Shivshankar, V.; Tripathy, S. K.; *Appl. Phys. Lett.,* **(1996)**, *68*, 2618.

(39) Hubert, C.; Fiorini-Debuisschert, C.; Maurin, I.; Nunzi, J.-M.; Raimond, P.; *Adv. Mater.,* **(2002)**, *14*, 729.

(40) Hubert, C.; Rumyantseva, A.; Lerondel, G.; Grand, J.; Kostcheev, S.; Billot, L.; Vial, A.; Bachelot, R.; Royer, P.; Chang, S.; *Nano Lett.,* **(2005)**, *5*, 615.

(41) Juan, M. L.; Plain, J.; Bachelot, R.; Vial, A.; Royer, P.; Gray, S. K.; Montgomery, J. M.; Wiederrecht, G. P.; *J. Phys. Chem. A,* **(2009)**, *113*, 4647.

(42) Juan, M. L.; Plain, J.; Bachelot, R.; Royer, P.; Gray, S. K.; Wiederrecht, G. P.; *J. Phys. Chem. Lett.,* **(2010)**, *1*, 2228.

(43) Palik, E. D.; Ghosh, G. *Handbook of optical constants of solids II*, 2nd ed.; Academic press: London, 1998; Vol. I.

(44) Lide, D. R. *CRC Handbook of Chemistry and Physics*, 90th ed.; CRC Press: New York, 2009.

(45) Galarreta, B. C.; Norton, P. R.; Lagugné-Labarthet, F.; *J. Phys. Chem. C,* **(2010)**, *114*, 19952.

(46) Chan, G. H.; Zhao, J.; Schatz, G. C.; Van Duyne, R. P.; *J. Phys. Chem. C,* **(2008)**, *112*, 13958.

Chapter 5: Detecting the Enhancement Factor on Hexagonal Array of Nanotriangles

5.1. Introduction

The controlled amplification of the Raman signals through a surface enhanced Raman spectroscopy effect is shown to be effective by finely tuning the properties of the metallic nanostructured surfaces.[1-5]However, since its discovery by Fleischmann's group,[6] and later by the correct interpretation by Albrecht and Van Duyne,[7,8] the quantification of the SERS enhancement factor has never been a straightforward task. Both research groups were conducting independent Raman experiments with pyridine adsorbed onto rough silver electrodes. Their initial assumption of an increase in the signal due to the growth on the surface of the electrode was quickly rejected. They quantified the contribution of the number of adsorbed molecules on the surface, and determined that the strong increase in the Raman signals (around 10^5 times) could not be related to the number of probed molecules, and concluded that the magnification of the signal came from an electric field enhanced Raman scattering effect.[7,8]

Since this early work, it is known that the effects responsible of such enhancement come from both an electromagnetic and chemical mechanisms, that are well explained in the literature.[4,9-11] A brief description of all the different factors responsible for the SERS enhancement was given in Chapter 1. However, from the experimental point of view, it is necessary to provide a rigorous methodology that allows one to quantify the enhancement factor and to compare with the estimation done for other structures. Up to now, it is difficult to establish a comparison of the different SERS enhancement factor reported in the literature for the various plasmonic nanostructures.[12-15] As it was discussed in the previous chapters, a large variety of structures have been prepared, and their plasmonic properties, responsible of the electromagnetic mechanism, have been studied experimentally and numerically; however, there are still some discrepancies in the estimation of the enhancement factor. Le Ru and his group have recently presented a

detailed analysis of the quantification process of the SERS enhancement factor.[13,14,16] They suggested that in some cases there is a misconception of the proper determination of the enhancement factor under different experimental conditions, and that in some reports there is not enough information about the experimental details to properly normalize the scattering cross-section of the probed molecules.[14] As a result, the determination of the enhancement factor in several published work is incorrectly estimated.

The scope of this chapter is to experimentally determine the enhancement factor of the hexagonal array of gold nanotriangles fabricated in this project. The estimation of this parameter will be done using the methodology established by Le Ru's group. A summary of this protocol will be developed in this chapter, not only as a review of the method, but also to provide the reader a better understanding of the practical considerations that must be taken once the fabricated nanostructured platforms are use with a confocal Raman microscope, points that will be useful when designing any SERS experiment. Finally, the enhancement factor of different hexagonal array of gold nanotriangles will be studied and compared with their plasmonic properties to establish the link between them.

5.2. Enhancement Factor

Generally speaking the definition of the SERS enhancement factor can be consider as the ratio between the SERS intensity per adsorbed molecule and the normal Raman intensity per bulk molecule.[17] However, the determination of the number of molecules that are responsible of the Raman signal and their contribution to the enhancement factor is not a trivial parameter and it may lead to erroneous estimation. The ensemble of parameters that need to be consider when performing a SERS experiment, such as probing a single molecule or multiple molecules, the orientation of the molecules in the experimental system, the spatial distribution, or the experimental limitations in resolution, make difficult the enclose the enhancement factor in only one definition.[13,15] Following Le Ru,[13,14] three different definitions of the enhancement factor are : the single molecule

enhancement factor (SMEF), the analytical enhancement factor (AEF) and the SERS substrate enhancement factor (SSEF).

5.2.1. Single molecule enhancement factor

SERS has caught the attention of several research groups since there were reports claiming that single molecule detection was achieved under enormous SERS enhancement factor conditions.[18,19] Since then, it was thought that in order to pursue the analysis of only one molecule required a SERS enhancement factor of the order of 10^{14}-10^{16}. However, recent reports suggest that these parameters are over estimated,[13,20,21] and the nature of the enhancement was not entirely understood in those initial reports. Thus, almost 10 years after those report suggested the single molecule detection of rhodamine 6G, a study of the same system suggested that the resonance Raman contribution of the rhodamine 6G/silver complex is of the order of 10^7.[22] Nowadays, there has been some progress in the field of single molecule detection and it is consider that SERS enhancement factor of the order of ~10^8 are enough to detect the SERS spectra of one molecule.[12,23]

The definition of the SERS single molecule enhancement factor (SMEF) comes from theoretical estimations, that consider the intensity of only one molecule at a specific point, the hot-spot location of the metallic nanostructure, and it is dependent of the Raman tensor of the molecule of interest, the orientation of the molecule on the surface, and the orientation of the molecule-SERS surface complex with respect to the polarization of the incoming field. Thus, the SMEF can be defined in **(1)** as the ratio of the SERS intensity of the probed molecule (I_{SERS}^{SM}) over the average Raman intensity per molecule of the same probe ($\langle I_{RS}^{SM} \rangle$).

$$SMEF = \frac{I_{SERS}^{SM}}{\langle I_{RS}^{SM} \rangle} = \frac{d\sigma_{SERS}^{SM}}{d\Omega} \Big/ \frac{d\sigma_{RS}}{d\Omega} \qquad \textbf{(1)}$$

This equation can also be defined in terms of the ratio between the SERS ($d\sigma_{SERS}^{SM}/d\Omega$) and regular Raman ($d\sigma_{RS}/d\Omega$) differential cross section. Since the detection of the SERS intensity of only one molecule it is difficult and the experimental volume analyzed contains more than one molecule on the SERS surface with different orientations.[13] It is convenient to define the orientation average of the SMEF (OASMEF in **(2)**), where the average of the SERS intensity for every possible orientation of the probe is considered ($[I_{SERS}^{SM}]$).[13,14]

$$OASMEF = (SMEF(= \frac{([I_{SERS}^{SM}]}{\langle I_{RS}^{SM} \rangle} \quad \textbf{(2)}$$

This work does not focus on single molecule detection, and a deeper description can be found elsewhere[5,14,21,22] about other practical consideration in the quantification of the SMEF, however the description given here highlights the importance of understanding the studied system and to take into account the different parameters responsible of the enhancement of the signal.

5.2.2. Analytical enhancement factor

In the case of solutions, where molecules are probed surrounded by a colloidal solution of metallic nanoparticles that produce the SERS enhancement, it is possible to assume that the quantification of the enhancement factor is the ratio between two experiments performed under the exact same conditions, and where the only difference is the presence of colloidal nanoparticles that generate SERS. Thus, the ratio calculated is between the SERS intensity (I_{SERS}) of the molecules probed within the colloidal solution (c_{SERS}), and the regular Raman intensity (I_{RS}) of a solution of the same molecular probe with no colloids involved (c_{RS}), as described in **(3)**.

$$AEF = \frac{I_{SERS}/c_{SERS}}{I_{RS}/c_{RS}} \quad \textbf{(3)}$$

However, this intuitive estimation, although practical from the analytical chemistry point of view, needs to consider that the principle behind the enhancement factor is a surface dependent effect. Therefore, the field enhancement decays exponentially as it goes away from the surface, and an excess in the number of molecules probed might lead to the formation of multilayers on the surface that would not have the same the same SERS enhancement.[13] Experimentally, the determination of the AEF considers a concentration of the molecules probed under SERS conditions well below the monolayer coverage of the metallic nanoparticles, which avoids the formation of such multilayer effect.

5.2.3. SERS substrate enhancement factor

As the SERS signals come from the molecules adsorbed at the surface of a metallic nanostructure, then it is logical to think that the surface must be considered in the determination of the SERS enhancement factor, and several reports focus in this fact, as described in **(4)**. Where the enhancement factor is defined as the ratio between the SERS intensity (I_{SERS}) per molecule adsorbed at the surface (N_{Surf}), and the Raman intensity under non-SERS conditions (I_{RS}) per average number of molecules in the scattering volume ($N_{Vol} = c_{RS}V$).

$$EF = \frac{I_{SERS}/N_{Surf}}{I_{RS}/N_{Vol}} \quad \textbf{(4)}$$

However, this definition does not provide enough details about the quantification of the molecules probed under SERS and non-SERS conditions. Thus, a more detailed description of these parameters is considered in the SERS substrate enhancement factor (SSEF), shown in **(5)**.[13]

$$SSEF = \frac{I_{SERS}/\mu_M \mu_S A_M}{I_{RS}/c_{RS}V_{eff}} \quad \textbf{(5)}$$

Herein, the number of molecules adsorbed in the surface is indeed related to the surface density of the hot-spots present in the metallic nanostructures (μ_M), the density of the

molecular probes adsorbed on metallic surface (μ_S), and the total metallic surface area (A_M). In the case of the estimation of the number of molecules probed under non-SERS conditions, the concentration (c_{RS}) and effective scattering volume (V_{eff}) must be considered. This last parameter needs to be determined experimentally, as it depends on the system used. A more detailed description will be given in the next section. The advantage of the SSEF over the traditional concept of the enhancement factor is the careful consideration of the different practical parameters that must be taken into account in order to rigorously quantify the SERS enhancement factor of the studied system. This last approach is used in the determination of the fabricated SERS platforms in this project.

5.3. Experimental consideration

The multiple definitions of the enhancement factor described in the previous section reflect the necessity of reporting the different experimental details of the SERS enhancement factor experiments. Following this approach, it becomes possible to establish normalization mechanisms, which allow the comparison between the different estimations of the enhancement factor reported in the literature. Therefore, a thorough description of all the necessary parameters to determine the number of molecules probed under SERS and non-SERS conditions needs to be described.

More specifically, two points are considered in this section to estimate correctly the number of molecules probed. First, it is described a practical method to determine the effective scattering volume, by measuring the lateral and axial cross sections of the focal volume is described. Second, the number of molecules adsorbed in the metallic surface, is determined.

5.3.1. Scattering volume

The estimation of the scattered volume in the SERS enhancement factor experiment depends on the characteristics of the experimental setup used. Thus, the use of a confocal Raman microscope with a specific microscope objective presents specific characteristics that need to be determined in order to rigorously quantify the region probed.

Experimentally, this volume is characterized by performing appropriate excitation and detection profiles of the system. Assuming an excitation intensity profile $I(\rho, z)$, whose intensity depends on the z position and is non uniform; and a detection efficiency profile $\eta(\rho,z)$, which is also strongly dependent of the experimental setup; the effective scattering volume (V_{eff}) can be defined by equation **(6)**. Where V_{eff} represents the volume of the Raman observed, and that is smaller than the actual volume probed. In order to detect the whole volume, both the excitation and detection profiles would have to be uniforms and equivalent to their maximum values (I_0 and η_0).[13]

$$V_{eff} = \int_{\rho=0}^{\rho=\infty} 2\pi\rho \int_{z=-\infty}^{z=+\infty} \frac{I(\rho,z)}{I_0} \frac{\eta(\rho,z)}{\eta_0} d\rho dz \quad \textbf{(6)}$$

Now, the effective scattering volume can be defined as the product of effective scattered area (A_{eff}) and the effective scattered height (H_{eff}), defined in **(7) - (9)**.

$$V_{eff} = A_{eff}.H_{eff} \quad \textbf{(7)}$$

$$A_{eff} = \frac{\pi {\omega_0}^2}{2} \quad \textbf{(8)}$$

$$H_{eff} = \int_{\rho=-\infty}^{\rho=+\infty} \frac{\eta_\perp(z)}{\eta_0} dz \quad \textbf{(9)}$$

Experimentally, these two parameters can be characterized by performing some beam profile experiments. In the case of the A_{eff}, the waist of the excitation profile (ω_0) can be detected by measuring the Raman intensity of a thin film with a strong Raman signal,

such as silicon, focus on the surface and as a function of the lateral movement over a sharp edge. On the other hand, the effective scattering height, the experimental detection requires some careful consideration as the axial detection efficiency ($\eta_{\perp}$) is strongly dependent of the wavelength, microscope objective and the confocal pinhole size. However, it is possible to assume that the Raman intensity function is proportional to the axial detection efficiency function when the pinhole is completely open. In that case, by obtaining a Raman intensity profile of silicon as a function of the focal point distance it is possible to estimate H_{eff}.[13,24] The experimental detection of both A_{eff} and H_{eff} are shown in the experimental section.

5.3.2. Number of molecules probed

The determination of the number of molecules, adsorbed on the metallic nanostructure, depends on the nature of the molecule itself as well as its interaction with the surface. From the different molecules used in the quantification of the enhancement factor under non-resonance Raman conditions, benzenethiol (BT) is one of the most common molecules probed and serves as a model molecule for SERS measurements.[25-30]

BT is adsorbed on a gold surface through a S-Au interaction, as well as other alkanethiols. Although the chemical nature of such adsorption it is not completely understood,[31,32] it is stable. Studies done on the surface functionalization of BT on gold, suggest that the Au-S-C bond angle presents a tilted orientation with a preference for a sp^3 hybridization, and where the surface density of the molecules are in the order of $4.4x10^{-10}$ mol/cm^2 (37.8 Å^2/molecule).[28,30] These parameters are important, as they allow one to estimatethe density of the molecular probes adsorbed on metallic surface (μ_S).

With these general considerations, it is possible to estimate the enhancement factor of the fabricated SERS platforms. The experimental section allows the reader to find a practical example of the parameters described, and sets all the different variables to rigorously

quantify the SERS enhancement factor of six different hexagonal arrays of gold nanotriangles.

5.4. Experimental section

5.4.1. Fabrication of SERS platforms

A detailed description of the fabrication process can be found in Chapter 2. In short, samples were fabricated by EBL on VistaVision™ microscope cover glass slides. The patterns consist of hexagonal arrangements of gold nanotriangles. By changing the area dose of the electron beam (70, 145($\mu C/cm^2$ the length and interparticle distance of the triangles was modified. Typical dimensions of (215, 135(nm were obtained for the triangle base size, and (55, 135(nm for the interparticle distance between nanotriangles, and with a thickness of Au or Ag of 50 ± 5 nm.

5.4.2. Extinction spectra

The LSPR bands of the samples were determined from the extinction spectra. A detailed description of the experiment was given in Chapter 2. In short, a halogen lamp source illuminates the sample with a collimated beam of 60 microns diameter. The transmitted light is then collected by a microscope objective prior to analysis by the spectrometer in the 400-900 nm spectra range. Typically, each spectrum is the result of 30 accumulations.

5.4.3. Physical characterization

Images were acquired using a scanning electron microscope (SEM), LEO 1530 Field Emission, with a 1.5-3.0 keV field-emission electron source. Atomic force microscopy (AFM) images were collected on a NanoWizard® II Bioscience AFM (JPK Instruments Inc.) in contact mode using a CONT-20 cantilever (k=0.2 N/m, Nano World Inc.). SEM and AFM scans were performed on several surface positions to check the surface

uniformity, the parameters obtained from the SEM scans were used in the detection of the length, interparticle distance, and the projected gold area of the arrays, while the information obtained from the AFM scans was used to quantify the thickness of the metallic patterns. The average size values are the result of at least ten different measurements on different spots of the scanned areas.

5.4.4. Functionalization of the SERS platforms

Samples were cleaned with Nano-strip solution for 3 minutes at r.t. The cleaned samples were immersed in a 10 mM solution of benzenethiol (Sigma-Aldrich) in ethanol (HPLC grade from Sigma-Aldrich) for 24 hours at room temeperature. Then, they were washed thoroughly with ethanol, and finally blown dry with nitrogen.

Table 5.1. Experimental conditions of the Raman experiments.

Experiment	Molecular probe	Filter[a]	Phinhole[b] (μm)	Irradiation time (s)	Accumulation number
Filter selection	silicon	D0-D4	1000	1	3
Pinhole	silicon	D0	20-1000	1	3
A_{eff}	silicon	D0.6	1000	1	2
H_{eff}	silicon	D0	1000	1	3
SSEF	BT	D1	500	20	3

[a]Density filters used in the optical path of the Raman system used to decrease the intensity of the excitation source. [b]Pinhole size of the confocal Raman microscope.

5.4.5. Raman spectra

Vibrational Raman spectra were recorded with a LabRAM HR (Horiba Scientific) spectrometer equipped with a Helium-Neon (He-Ne) laser (laser at 632.8 nm), a 600 grooves per mm grating and a 20x/N.A 0.50 objective. Raman bands were measured with an accuracy of about 1.2 cm^{-1}. The conditions for the different Raman experiments done are summarized in **Table 5.1**. All the SERS experiments were done with a careful control

over the orientation of the platform, in order to have the polarizer of the input laser parallel to a bow tie axis.

5.5. Results and discussion

5.5.1. Optimization of the parameters of the microscope

The intense Raman signal of silicon at 520 cm^{-1} was used as a calibration parameter in all the microscope optimization experiment.

Filters. The intensity of the Raman laser was controlled by the use of internal filter in the system. **Figure 5.1.a** shows the correlation between the filter number and the power intensity of the beam. This last parameter is the result of a correction factor established between the intensity of the silicon signal (intensity: 10563.3 ± 3.1counts) and the power intensity measured of the incoming laser (power: 11.8 ± 0.1 mW) at 632.8 nm, when no filter was present. The correction factor was then used for all the other filters. Each point in the graph represents at least three different measurements taken.

Pinhole. The adjustable pinhole is an important part in a confocal microscope, as it allows filtering out the scattering signal from the regions that are not at the focal point. This property might be useful in some experiments when the background signal presents a strong scattering cross that overlaps the signal of the analyte, but in some cases it also affect the intensity of the molecular probe as well. **Figure 5.1.b**, shows the effect in the intensity of the silicon signal when the pinhole size is modified. From the graph, it is possible to detect a plateau in intensity, when the confocal hole size is above 200 μm. This is an important result that helps to understand the behavior of the LabRam HR, and to design new experiments.

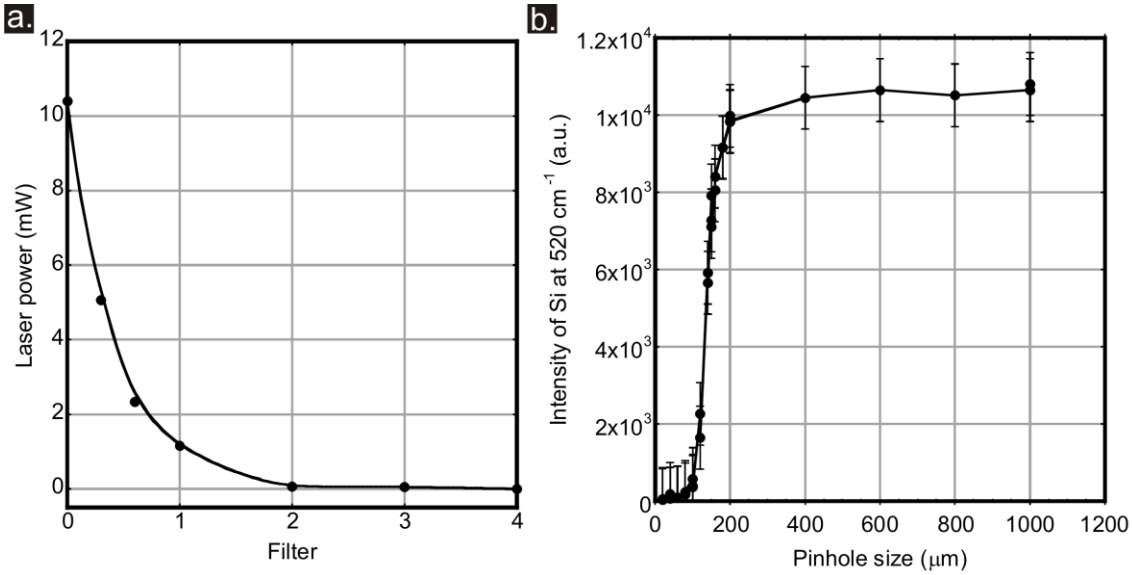

Figure 5.1. Effect of the microscope internal filters (a) and of the pinhole size (b) in the intensity of the Raman laser and of the silicon signal, respectively.

Effective scattered area (A_{eff}). As described in Section 5.3.1 the experimental estimation of A_{eff} can be performed by scanning the surface of a thin film of silicon. Herein, we decided to perform this experiment by taking advantage of the Raman mapping of the LabRam HR in communication with the piezoelectric stage of the JPK-AFM. Thus, a small scan area of 20 x 2.5 μm^2 was mapped, and the Raman spectrum in the [400-600] cm^{-1} was collected at every point. The size of each pixel was set to 0.5 x 0.5 μm^2. The result of this map is shown in **Figure 5.2.a**. The color bar indicates the integral intensity of the Raman signal of silicon, as shown in the inset. The intensity values were collected and analyzed to generate the plot shown in **Figure 5.2.b**. The width, or the waist of the extinction profile (ω_0), can be calculated by full width of the half height measure. In this case the half height of the Gaussian bell shape must consider as a base the intensity plateau when the beam is focus on the surface. Therefore, from the results it is possible to estimate the effective scattering area (A_{eff}: 19.80 μm^2).

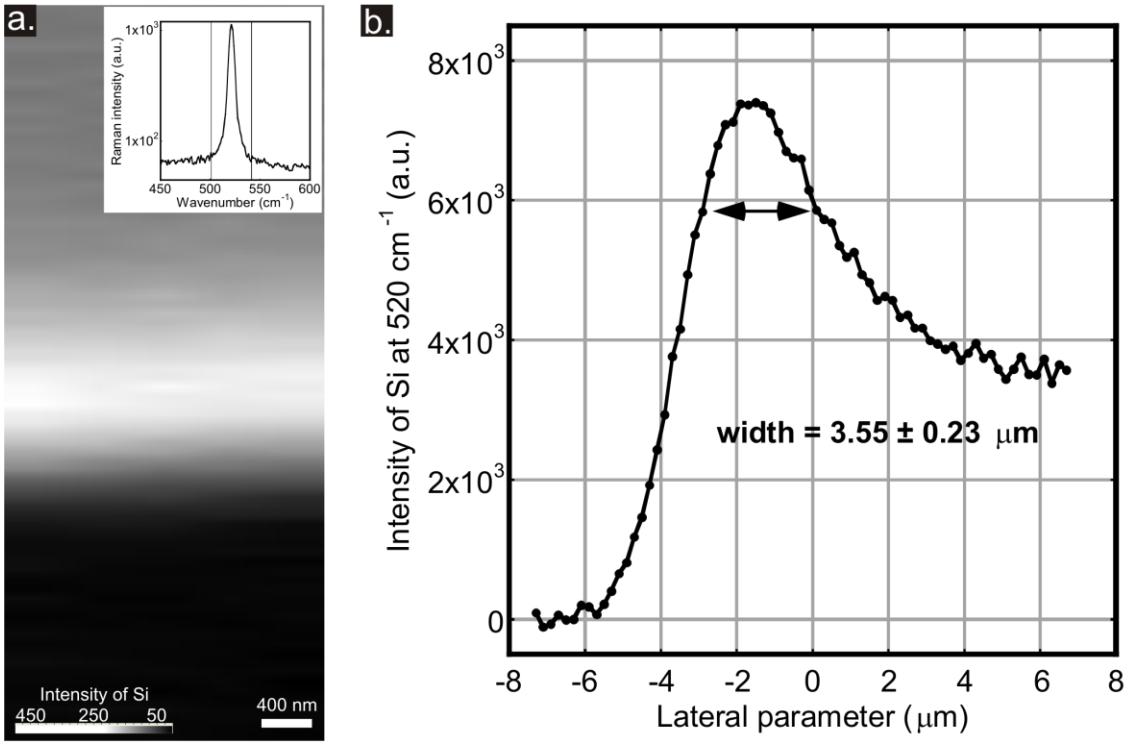

Figure 5.2. Raman map of the border of a silicon thin film (a) and profile intensity plot of the silicon signal that allows the estimation of effective scattering area (b).

Effective scattered height (H_{eff}). This parameter can also be estimated by the analysis of the silicon intensity profile when the focal point is tuned. This experiment, although similar confocal experiments traditionally done in optical microscopy,[24] provides a close approximation of the H_{eff}, only if all the other variables that affect the axial detection efficiency ($\eta_{\perp}$) become negligible in the calculation. Thus, keeping constant the effect of the intensity of the incoming beam, or the microscope objective, and having the pinhole completely open, made possible this approximation. **Figure 5.3** shows the intensity profile plot, and by quantifying the full width at half maximum of the Gaussian bell shape, the effective scattered height ($H_{eff} \approx 111.1$ μm) can be determined for the 20x/N.A. 0.50 objective.

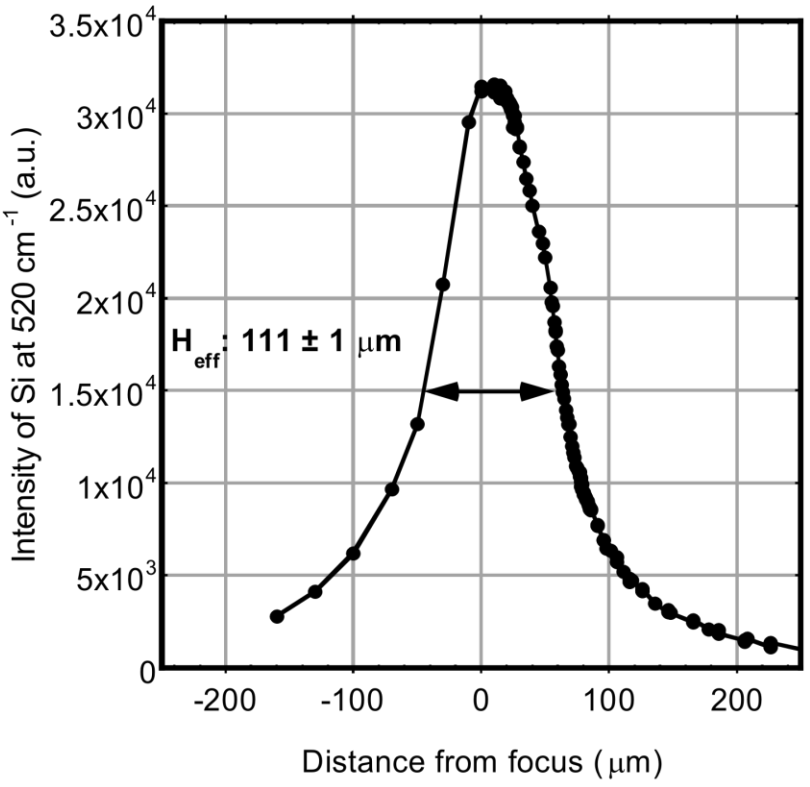

Figure 5.3. Intensity profile of silicon when the distance from the focal point is tuned.

5.5.2. Characteristics of SERS Platforms

Six different arrays of hexagonal array of gold nanotriangles, or Fischer's patterns, were prepared by EBL. The physical and optical characterization of these structures is summarized in **Figure 5.4**. A change in the nominal area dose of the electron beam allows one the fabrication of triangles of different length and different gap, or interparticle distance. In addition, this graph also summarizes the plasmon band detected from the extinction spectra of these arrays. The trends described in Chapter 2 are also detected for these six different arrays of smaller lattice size.

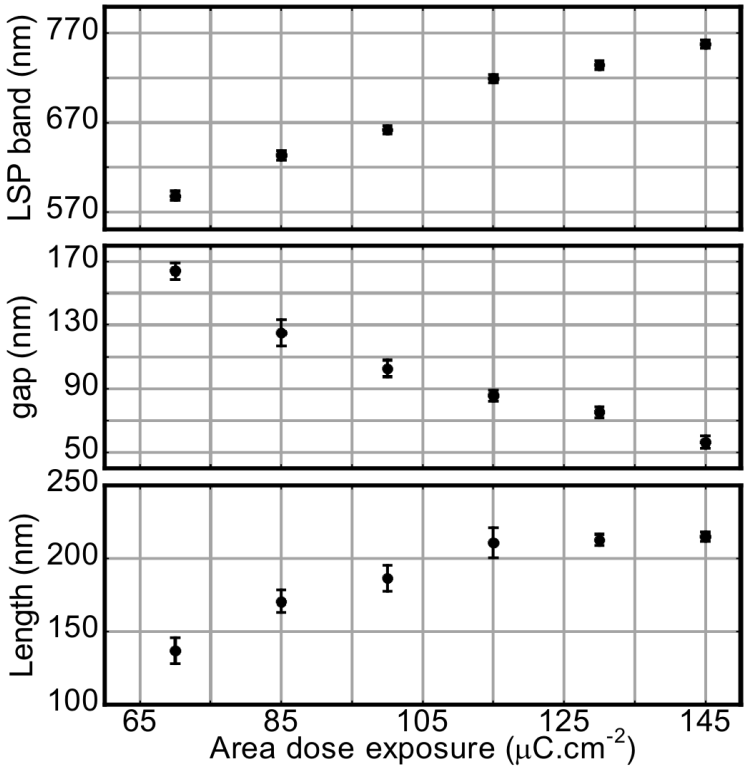

Figure 5.4. Summary of the properties of the Fischer's patterns studied.

5.5.3. SERS Surface Enhancement Factor

Raman spectrum of benzenethiol (BT). The Raman spectrum of BT was obtained as a reference (**Figure 5.5**). A concentrated solution of BT ([BT] = 15.39 M) was characterized under the Raman conditions described in **Table 5.1**.From its spectrum it is possible to identify the in-plane bending (β) and stretching (ν) modes of BT, such as β_{CCC} and ν_{CS} (415, 619, 700, 1093 cm^{-1}), β_{SH} (919 cm^{-1}), β_{CCC} (1002 cm^{-1}), β_{CH} (1027, 1125, 1158, 1187 cm^{-1}), and ν_{CC} (1584 cm^{-1}). This information and the estimation of the effective scattered volume provide all the necessary details to obtain the intensity and number of molecules of the non-SERS parameters of the enhancement factor ($I_{RS}/c_{RS}V_{eff}$).

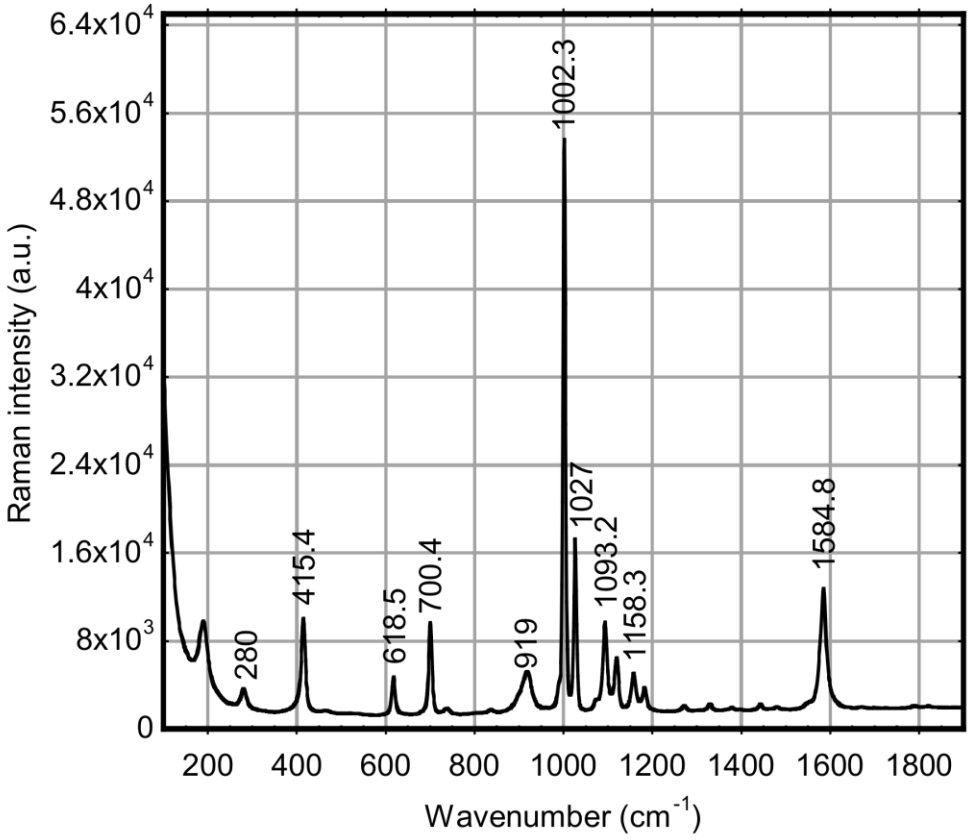

Figure 5.5. Raman spectrum of concentrated solution of benzenethiol when excited with a 632.8 nm laser.

SERS spectrum of BT adsorbed on Fischer's patterns. The spectrum of the functionalized benzenethiol on the SERS platforms was obtained under the same experimental conditions of the concentrated solution of BT. **Figure 5.6** shows an example of one of the spectra obtained for each pattern. These patterns have been labeled according their fabricated area dose exposure. From this group of spectra, it is possible to notice a change in intensity for the different patterns. The four most intense bands in the spectrum were chosen to quantify the SERS enhancement factor in these platforms. These bands correspond to: β_{CCC} (999 cm^{-1}), β_{CH} (1024 cm^{-1}), β_{CCC} and ν_{CS} (1074 cm^{-1}) and ν_{CC} (1584 cm^{-1}). The best SERS spectra are obtained for the platforms with the smaller triangle size and the largest interparticle distance (**Figure 5.4**).

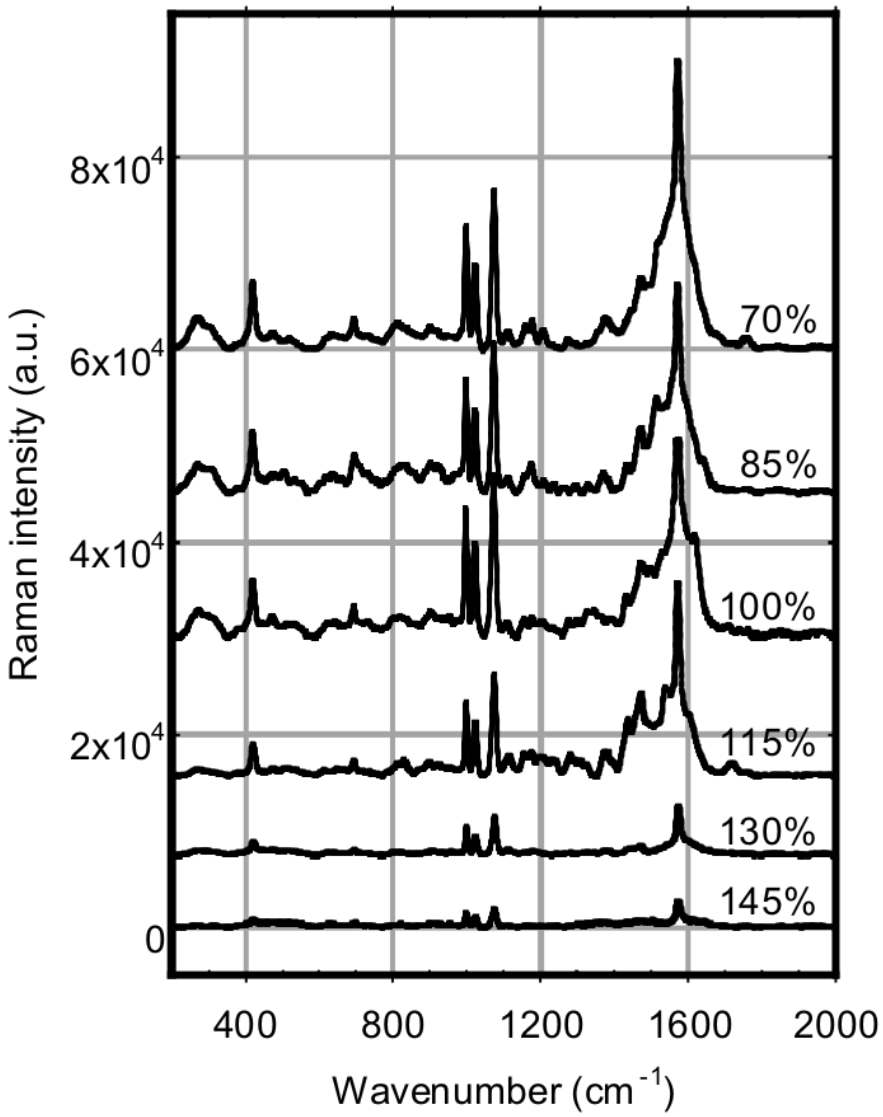

Figure 5.6. SERS spectra of adsorbed benzenethiol on SERS platforms.

With such set of collected data, it is possible to determine the SERS enhancement factor of these structures. The SERS intensity is obtained from the spectrum itself, the metallic surface area is determined by the structural information collected from the SEM and AFM images. Finally the determination of the number of molecules probed can be calculated using the surface density parameter from the literature. Therefore, the results

obtained from these SERS platforms combined with the parameters from the normal Raman spectrum of a concentrated solution of BT, make possible the quantification of the SERS enhancement factor on these nanostructured platforms, as it is illustrated in **Figure 5.6.a**. From the graph it is possible to detect that for all the different arrays and using the different Raman signal, the estimated enhancement factor is of the order of 10^4-10^6. Now, it is also possible to detect that those arrays that were fabricated under a longer exposure of the electron beam, meaning a larger area dose that generates bigger features with smaller interparticle distance and with a red-shifter plasmon band, there is a decay of the enhancement factor. However, it seems there is a breaking point at 115 μC/cm^2, where the enhancement factor of all the arrays prepared by a larger area dose than that value, present a sharper decaying slope.

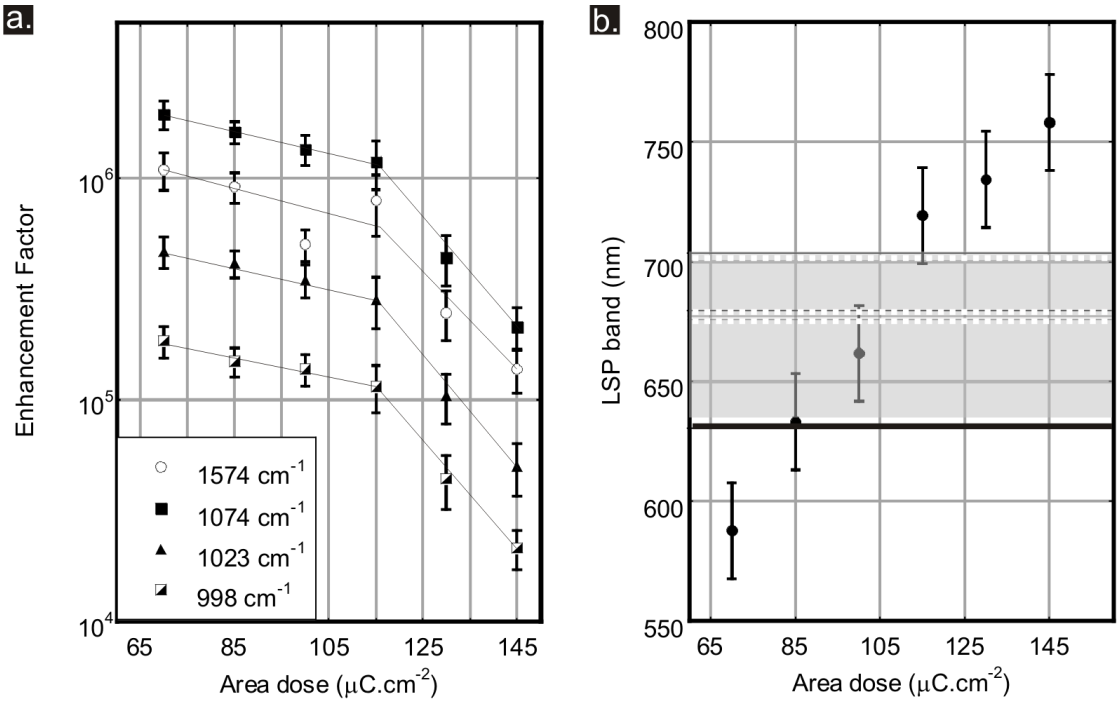

Figure 5.7. SERS enhancement factor (a) and plasmon band (b) of the arrays fabricated by a different area dose.

A possible interpretation of this change in the decaying slope can be done by comparing the plasmon bands of such structures (**Figure 5.6.b**), and the correlation with the incident Raman beam, shown as a bold black line in **Figure 5.6.b**. As well as the region corresponding to the Raman spectral region, illustrated as a gray area in **Figure 5.6.b**, where the Raman signal has been converted from wavenumbers to wavelengths and highlighted in **Figure 5.6.b** with dash lines. This plot shows that then enhancement is magnified when the plasmon band is localized between, or very close to, the incident beam and the Raman spectral region analyzed. A similar connection between the plasmon band and the enhancement factor has been given in the literature,[12,17] strengthen the interpretation given here.

In addition, it is possible to notice that not all the SERS signals exhibit the same enhancement factor, and from the four selected vibrational modes, the band that is closer to the incident frequency is the least enhanced. It is not surprising to find that the signals do not have the same enhancement factor, as each Raman tensor presents a different scattering cross section, which is also responsible of the intensity of the Raman band.

5.6. Conclusions

A complete analysis was given about the different parameters that need to be taken into consideration when quantifying the SERS enhancement factor. Using the concept and practical considerations described here it was possible to properly estimate the enhancement factor of different arrays of gold nanotriangles.

A rigorous quantification of the enhancement factor of the fabricated structures was performed and analyzed. All the fabricated nanostructures present a large enhancement of the order of 10^4-10^6 obtained in non-resonant conditions against benzenethiol, strengthening the properties of the SERS platforms designed in this project. In addition, a

comparison of the calculated enhancement factor and the plasmonic band of the arrays was given, establishing a correlation between both of them as well as with some of the experimental conditions, such as the Raman laser, or the scattering cross section of the Raman tensor of the probed molecule. All of these, factors that need to be taken into account when designing new experiments with these or other nanostructures.

5.7. References

(1) Aroca, R. *Surface-Enhanced Vibrational Spectroscopy*; John Wiley & Sons, Ltd: West Sussex, England, 2006.

(2) Kneipp, K.; Moskovits, M.; Kneipp, H. *Surface-Enhanced Raman Scattering: Physics and Applications*; Springer- Verlag Berlin: Berlin, 2006.

(3) Morton, S. M.; Silverstein, D. W.; Jensen, L.; *Chem. Rev.*, **(2011)**, *111*, 3962.

(4) Moskovits, M.; *J. Raman Spectrosc.*, **(2005)**, *36*, 485.

(5) Moskovits, M.; Tay, L. L.; Yang, J.; Haslett, T. SERS and the single molecule. In *Optical properties of Nanostructured Random Media*; Shalaev, V. M., Ed.; Springer: Berlin, 2002; pp 215.

(6) Fleischmann, M.; Hendra, P. J.; McQuillan, A. J.; *Chem. Phys. Lett.*, **(1974)**, *26*, 163.

(7) Albrecht, M. G.; Creighton, J. A.; *J. Am. Chem. Soc.*, **(1977)**, *99*, 5215.

(8) Jeanmaire, D. L.; Van Duyne, R. P.; *J. Electroanal. Chem.*, **(1977)**, *84*, 1.

(9) Barnes, W. L.; Dereux, A.; Ebbesen, T. W.; *Nature*, **(2003)**, *424*, 824.

(10) Campion, A.; Kambhampati, P.; *Chem. Soc. Rev.*, **(1998)**, *27*, 241.

(11) Kambhampati, P.; Child, C. M.; Foster, M. C.; Campion, A.; *J. Chem. Phys.*, **(1998)**, *108*, 5013.

(12) Haynes, C. L.; Van Duyne, R. P.; *J. Phys. Chem. B*, **(2003)**, *107*, 7426.

(13) Le Ru, E. C.; Blackie, E.; Meyer, M.; Etchegoin, P. G.; *J. Phys. Chem. C*, **(2007)**, *111*, 13794.

(14) Le Ru, E. C.; Meyer, M.; Blackie, E.; Etchegoin, P. G.; *J. Raman Spectrosc.*, **(2008)**, *39*, 1127.

(15) Natan, M. J.; *Faraday Discuss.*, **(2006)**, *132*, 321.

(16) Le Ru, E. C. L.; Galloway, C.; Etchegoin, P. G.; *Phys. Chem. Chem. Phys.*, **(2006)**, *8*, 3083.

(17) Henry, A.-I.; Bringham, J. M.; Ringe, E.; Marks, L. D.; Schatz, G. C.; Van Duyne, R. P.; *J. Phys. Chem. C*, **(2011)**, *115*, 9291.

(18) Kneipp, K.; Wang, Y.; Kneipp, H.; Perelman, L. T.; Itzkan, I.; Dasari, R.; Feld, M. S.; *Phys. Rev. Lett.*, **(1997)**, *78*, 1667.

(19) Emory, S. R.; Haskins, W. E.; Nie, S.; *J. Am. Chem. Soc.*, **(1998)**, *120*, 8009.

(20) Etchegoin, P. G.; Le Ru, E. C.; *Phys. Chem. Chem. Phys.*, **(2008)**, *10*, 6079.

(21) Wustholz, K. L.; Brosseau, C. L.; Casadio, F.; Van Duyne, R. P.; *Phys. Chem. Chem. Phys.*, **(2009)**, *11*, 7350.

(22) Shim, S.; Stuart, C. M.; Mathies, R. A.; *ChemPhysChem*, **(2008)**, *9*, 697.

(23) Blackie, E. J.; Ru, E. C. L.; Etchegoin, P. G.; *J. Am. Chem. Soc.*, **(2009)**, *131*, 14466.

(24) Baldwin, K. J.; Batchelder, D. N.; *J. Appl. Spectrosc.*, **(2001)**, *55*, 517.

(25) Aggarwal, R. L.; Farrar, L. W.; Diebold, E. D.; Polla, D. L.; *J. Raman Spectrosc.*, **(2009)**, *40*, 1331.

(26) Biggs, K. B.; Anker, J. N.; Van Duyne, R. P.; *J. Phys. Chem. A*, **(2009)**, *113*, 4581.

(27) Gartia, M. R.; Xu, Z.; Behymer, E.; Nguyen, H.; Britten, J.; Larson, C.; Miles, R.; Bora, M.; Chang, A. S.-P.; Bond, T. C.; Liu, G. L.; *Nanotechnology*, **(2010)**, *21*, 395701.

(28) Sabatani, E.; Cohen-Boulakia, J.; Bruening, M.; Rubinstein, I.; *Langmuir*, **(1993)**, *9*, 2974.

(29) Diebold, E. D.; Peng, P.; Mazur, E.; *J. Am. Chem. Soc.*, **(2009)**, *131*, 16356.

(30) Tao, Y.-T.; Wu, C.-C.; Eu, J.-Y.; Lin, W.-L.; *Langmuir*, **(1997)**, *13*, 4018.

(31) Ostuni, E.; Yan, L.; Whitesides, G. M.; *Colloids Surf., B* **(1999)**, *15*, 3.

(32) Jadzinsky, P. D.; Calero, G.; Ackerson, C. J.; Bushnell, D. A.; Kornberg, R. D.; *Science*, **(2007)**, *318*, 430.

Chapter 6: Applications and Integration of SERS Platforms in Bioanalysis℘

6.1. Introduction

The possibility to probe trace chemicals, i.e. vibrationally, that are adsorbed in a functionalized surface, and study *in-situ* dynamical processes in a complex monolayer assembled environment, is of great interest and potentially opens many opportunities to understand fundamental issues at surfaces and interfaces. However, the general difficulty of probing monolayers on flat surfaces using vibrational techniques arises from the small number of molecules to be probed and the possible large background signal of the substrate. Nevertheless, modern vibrational techniques such as polarization modulation infrared reflection absorption (PM-IRRAS) or vibrational sum frequency generation (VSFG) have a monolayer sensitivity, and specificity in the case of VSFG. Therefore both techniques allow one to detect the fingerprints of a monolayer adsorbed onto a substrate or located at the surface of a liquid.[1-3] However, both methods generally require long acquisition times, i.e. several minutes, and the accessible spectral range can be limited due to the optical design of the apparatus. In this context, Raman spectroscopy is of interest since, when combined with surface enhanced effects, it can amplify the signal of adsorbed molecules onto a metal surface by several orders of magnitude.[4,5]

The previous chapters described some of the different approaches concerning the fabrication of surface enhanced Raman spectroscopy (SERS) active metallic surfaces,[6-8] as well as a summary of the different effects responsible of the enhancement.[5] Although the first observations of the SERS effect were reported almost four decades ago,[9,10] recent publications have shown a renewed interest in SERS for the study of biomolecules and

---

℘ Sections of this chapter have been published elsewhere. Reproduced with permission from [*Langmuir* (**2011)** *27*, 1494.] Copyright 2011 American Chemical Society.

biophysical processes.[8,11,12] The design and synthesis of new metallic nanomaterials and nanostructures are of great interest and are applied to a variety of bio related issues.

Among these nanomaterials, patterned metallic surfaces have shown great promise due to their high reproducibility and control of the substrates. Such metallic nanostructures, most often made of silver and gold, are inscribed on a surface with 2D or 3D architectures that exhibit sharp features.[6,13-15] Nanohole arrays, nanosphere lithography templates, as well as arrays of 3D tips, needle arrays and pillars are some of the structures that have shown large Raman enhancements varying from 10^4 to 10^6.[16-20] In the case of the Fischer's patterns developed in this project, the enhancement factor obtained is of the order of 10^5-10^6, as described in Chapter 5. Such enhancement factors are in many instances, sufficient to probe the vibrational signature of monolayers with acquisition times limited to a few seconds and under non-destructive laser intensity.

Two different systems were chosen as possible applications of the fabricated SERS platforms. Both of them required the functionalization of the gold nanostructures by using self-assembly monolayers. The first example given involves the study of a host-guest protein interaction between Streptavidin and biotinylated surfaces. The interaction of the Streptavidin/biotin complex has been broadly used in the development of molecular sensors,[21] and the detection of this bio-molecular donor receptor employing a SERS platforms is attractive in the bio-analysis.[22-25] The second example concerns the field of aptamer-based sensors.[26,27] Herein, an alkanethiolated aptamer sequence chemically modifies the gold surface of the nanostructures and promotes the adsorption of a specific target molecule, and a change in conformation of the aptamer, which can be detected by comparing the SERS spectra.[28-31] Detection of ochratoxin A, a mycotoxin present in different food commodities, using a self-assembled monolayer aptamer was performed in a microfluidic SERS device, showing that the SERS platforms can be used in the design of toxicological sensors. The scope of this chapter is therefore to illustrate the versatility

of our SERS platforms and the feasibility to integrate them in a micro-total analysis system (μ-TAS).

6.2. Self-assembled monolayers (SAMs)

The modification of the physical and chemical properties of solid surfaces is possible by the use of self-assembled monolayers. Herein molecules with an end group that can react with the external face of the solid, are spontaneously chemiadsorbed on the surface, and the presence of alkyl chains in the molecules promote van der Waals interactions that lead to the formation of organized monomolecular assemblies.[32,33] As a result, by selecting different groups at the other extremity of the molecules, it is possible to rationally design surfaces with different properties.

Alkanethiols (*X-R-SH*) self-assembled monolayers on gold are one of the assemblies most studied[33] and used in sensor development due to its reproducibility, straightforward preparation and versatility.[2,25,32,34,35] Although, it is known that the *S-Au* interaction is relatively stable ($\Delta H^o \approx 28$ kcal/mol),[36] the nature of such interaction is still a contradictory topic.[34,37] One of the proposed theories suggests the transformation of Au(0) to Au(I) thiolate, as shown in **(1)**.[34]

$$X\text{-}R\text{-}SH + Au(0)_n \rightarrow X\text{-}R\text{-}S\text{-}Au(I)\text{-}Au(0)_n + \tfrac{1}{2}H_2 \qquad \textbf{(1)}$$

The preparation of the organized SAMs only requires a clean gold surface and a solution of alkanethiols. The surface is previously cleaned to remove any contaminants from the surface. Contrary to other metals, such as silver or copper, gold is inert to the environment and does not tend to oxidize under normal conditions. Therefore the cleaning process only requires a piranha solution that removes any organic and leave a hydrophilic gold surface ready to be functionalized. The alkanethiols are dissolved in pure solvents, ethanol in the case of non-polar molecules or water for the polar

alkanethiols, and usually the surface is immersed in a millimolar solution of the alkanethiol. The concentration of the solution and the time are parameters that can be tuned to achieve a full coating of the surface. Finally, the surface is rinsed several times with the same solvent to remove any non-adsorbed molecules, and finally dried.[34,35]

The other extremity of the alkanethiol (X) provides the different chemical properties of the surface and are responsible of the multiple applications of SAMs. Functional groups whose size is similar to methyl groups do not tend to modify the orientation of the assembly. Thus, it has been reported that a mixture of alkanethiols can be also used and the molar ratio seems to be preserved on the surface.[35] However this condition is not so trivial when the X group become larger or is part of bigger systems, such as antibodies, aptamers or proteins.[29,34,38-40] In some cases a mixture of alkanethiols with small head groups (e.g. X = -OH, -COOH, $-NH_2$) will first form a SAM on the surface, and then some of this head groups are derivatized into more complex ligands.[34,38] A different approach requires a two-step process, where first the alkanethiol with the voluminous head group is chemiadsorbed to the surface and in a second step a different alkanethiol is added to prevent other species from free-interaction with the surface. [29,39,40] As a result the different functional groups at the end of the alkanethiol, in a mixture or in a pure environment, are responsible for the different physical and chemical properties of the solid surface.

The characterization methods of SAMs are diverse and each of them provides different information about the surface. As it was described in the introduction, the focus of this chapter concerns in the vibrational characterization of SAMs on gold nanostructures, however some of the multiple techniques used in the characterization of alkanethiolate SAMs on gold surfaces are summarized in **Table 6.1**.[32,34]

Table 6.1. Methods for the characterization of alkanethiolated SAMs on gold.[32,34]

Property of SAM	Technique
Thickness	Ellipsometry, surface reflectivity
Wettability	Contact angle, surface energy
Defects and/or degree of perfection	Scanning probe microscopy (STM, AFM), wet chemical etching, electrochemistry (e.g. cyclic voltametry)
Composition	X-ray photoelectron spectroscopy (XPS), mass spectrometry
Structure and order	STM, AFM, X-ray diffraction, surface plasmon resonance (SPR), vibrational spectroscopy (PMIRRAS, VSGR, SERS)

Table 6.1 highlights that the characterization of SAM cannot be performed solely based on one technique However, from the different techniques, SERS presents some advantages over the others in the study of complex biological media with surfaces since: (i) it provides structural information about the surface; (ii) it allows the study in situ without destroying or directly interacting the surface; (iii) it requires a minimum amount of material, no need of a large scanned area; (iv) it presents a high signal to noise ratio under optimal conditions and with short acquisition times. All these advantages make of SERS an attractive method to study complex surface systems.

6.3. Streptavidin/biotin molecular system

Streptavidin/biotin assemblies are model systems for molecular recognition and biorecognition.[21] Due to the high affinity between biotin derivatives and the tetrameric active sites in Streptavidin, as well as the high stability of this molecular assembly ($K_d \approx 10^{-15}$),[41,42] numerous fundamental studies and applications have emerged for this stable biosystem.[43] The strong affinity of both molecules derives from intra- and

intermolecular interactions between tryptophan (Trp) residues and non-polar side chain of the protein with the non-polar moieties of biotin, based on hydrogen bonding and hydrophobic interactions. All these characteristics make of the Streptavidin/biotin supramolecular system an ideal model for biomolecular recognition and binding site identification.

Surfaces can be functionalized with biotinylated molecules and can be used as the basic elements for biosensing applications, such as their integration in micro-total analysis systems for further real-time monitoring of specific guest molecules. Once the surface is functionalized, techniques to judge the quality of the Streptavidin/biotin complex surface with a monolayer are often based on typical surface measurements, such as surface contact angle, or localized surface plasmon resonance measurements,[38,44-46] but these approaches generally lack molecular specificity. In contrast, vibrational spectroscopy is a direct technique to identify the intra- and intermolecular interactions in the assembly without the need of a molecular label as in fluorescence spectroscopy. Up to now, vibrational studies of this complex have been conducted in solution,[47,48] using IR or Raman spectroscopies with colloidal metallic nanoparticles to benefit from a local SERS enhancement.[22-25] However, such measurements are much more difficult to conduct on functionalized surfaces due to the weak signal of an adsorbed monolayer. As a result, the possibility to use SERS platforms in the detection of Streptavidin/biotin surface molecular system is of interest in the bio-analytical field.

6.4. Ochratoxin A-binding aptamer

Sensing technology has turned its attention into the development of aptamer-based systems. These short single-stranded oligonucleotides (20-100 unit bases) of DNA or RNA, defined as aptamers, are now widely use as molecular receptors because of their ability to detect and identify specific target molecules. The process behind the design of the aptameric sequence is called SELEX (Systematic Evolution of Ligands by

EXponential enrichment). This technique uses the principles behind combinatorial chemistry to select from a library of oligonucleotides the sequence or sequences that best interact with the probed molecule. Thus, by an interactive screening of the libraries used it is possible to discard the sequences that are not selective and to amplify the concentration of those oligonucleotides that can bind to the specific target molecule.[49,50]

There are multiple examples in the literature of the use of aptamer-based sensors to detect large systems, such as proteins, and pathogenic microorganisms;[51-54] or small atoms and molecules, such as amino acids, cations, toxins and others.[26,27,55,56] In all these cases the aptamer interacts with the target molecule producing a change in conformation of the oligonucleotide that can be detected in a direct or indirect manner, by the use of fluorescence,[57-70] electrochemistry,[71-76] colorimetry using gold nanoparticles,[26,77-79] as well as SERS.[28-31,39,80,81]

Ochratoxin-A (OTA) represents an interesting target molecule that can be detected using aptamers. This nephrotic mycotoxin has been detected in different food commodities,[82-84] such as cereals, wine, or coffee beans,[85-88] resulting in probable human exposure[89] and presenting potential public health risks.[90] To protect humans and animals from OTA exposure, many countries have set limits on OTA levels in food, typically 1-10 ppb.[91]

Few studies have been done in OTA-binding aptamers, where fluorescence,[65-70] electrochemistry,[76] and colorimetry[77] have been the selected detection methods. Up to date there has been no report that detects the presence of OTA interacting with aptamers by using Raman spectroscopy. It is well established that, upon OTA binding, the OTA-aptamer turns from a random coil structure to a G-quadruplex structure.[77] The hypothesis of this work is that this conformational change could be converted into a suitable Raman signal, as it has been highlighted for other target molecules,[39,80,81] like thrombin (**Figure 6.1**).[31] Furthermore, the goal is to functionalize the SERS metallic nanostructures with an

alkanethiolated aptamer that selectively binds to OTA and detect the SERS signal and the spectral changes associated with the recognition event, within a microfluidic device. This opens new prospects in the field of micro total analytical systems where optical analytical measurements of reduced volumes are of interest.

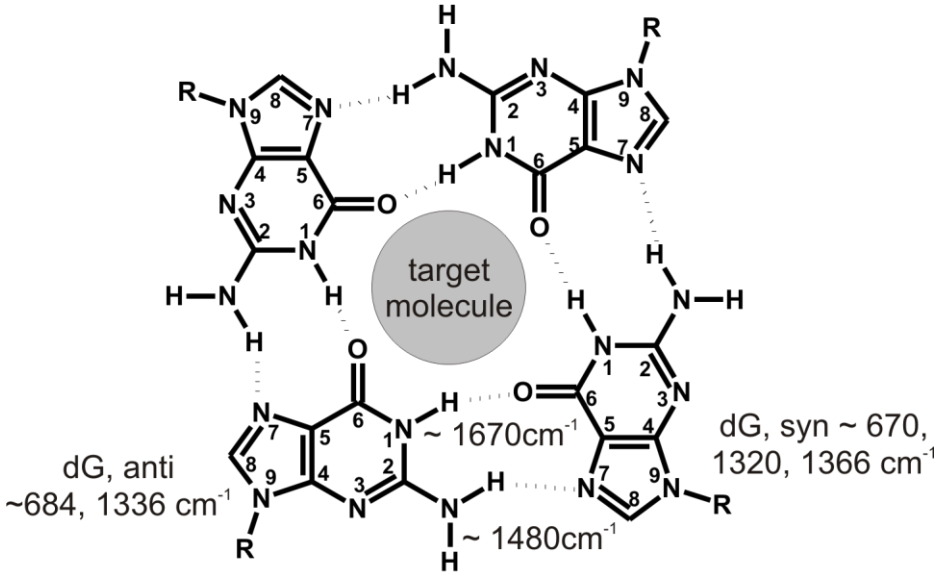

Figure 6.1. Guanine quartet of thrombin-binding aptamer showing the characteristics vibration frequencies.[31]

6.5. Micro-total analysis system (μ-TAS)

Micro-total analysis systems constitute an important field in analytical technology. They have potential of (i) reducing the amount of chemicals required, (ii) shorten the analysis times, (iii) improving the sensitivity of the detector, (iv) making the device portable, allowing *in situ* and real-time analysis, and (v) being disposable, if required.[92,93]

In this context, microfluidics is a key factor in the development of μ-TAS. Herein, under the right conditions of liquid flow, channel radius and geometry, and viscosity,[93,94] the

fluid flow is laminar, promoting rapid and effective mixing between the different components in the solution, and improving diffusion and mass transport through the channels.[92-94]

The integration of optical spectroscopy in μ-TAS is attractive, as it provides a good chemical analysis of the analytes. However, one of the challenges here is the limits of detection, the short optical path-length, and the small sample volumes.[95] Herein the the fabricated SERS platforms are integrated in a microfluidic device and used in the analysis of the OTA-binding aptamer system. This example tries to prove how the highlighted problem in the integration of optical detection systems in μ-TAS can be overcome.

6.6. Materials and methods

6.6.1. Fabrication of SERS platforms

A detailed description of the fabrication process can be found in Section 2.4.1. In short, SERS platforms were fabricated by electron beam lithography on VistaVision™ microscope cover glass slides. A 40 nm gold film was deposited on top of the revealed stencil resist film, and after the lift-off step, a periodic array of gold nanotriangles organized in a hexagonal conformation was revealed (**Figure 6.2.a**).

6.6.2. Functionalization of gold.

6.6.2.1. Streptavidin/biotin system.

Ethanol (HPLC grade) and Streptavidin from *S. avidinii* (Strep) were obtained from Aldrich. 11-mercaptoundecanoic-[13-biotinoylamido-4,7,10-trioxatrydecanyl]amide (BAT, **Figure 6.2**), and [11-mercaptoundec-11-yl]tryethylene glycol (OEG, **Figure 6.2**) were purchased from nanoScience instruments. Phosphate buffer solution (PBS) pH 7.4 was obtained from GIBCO.

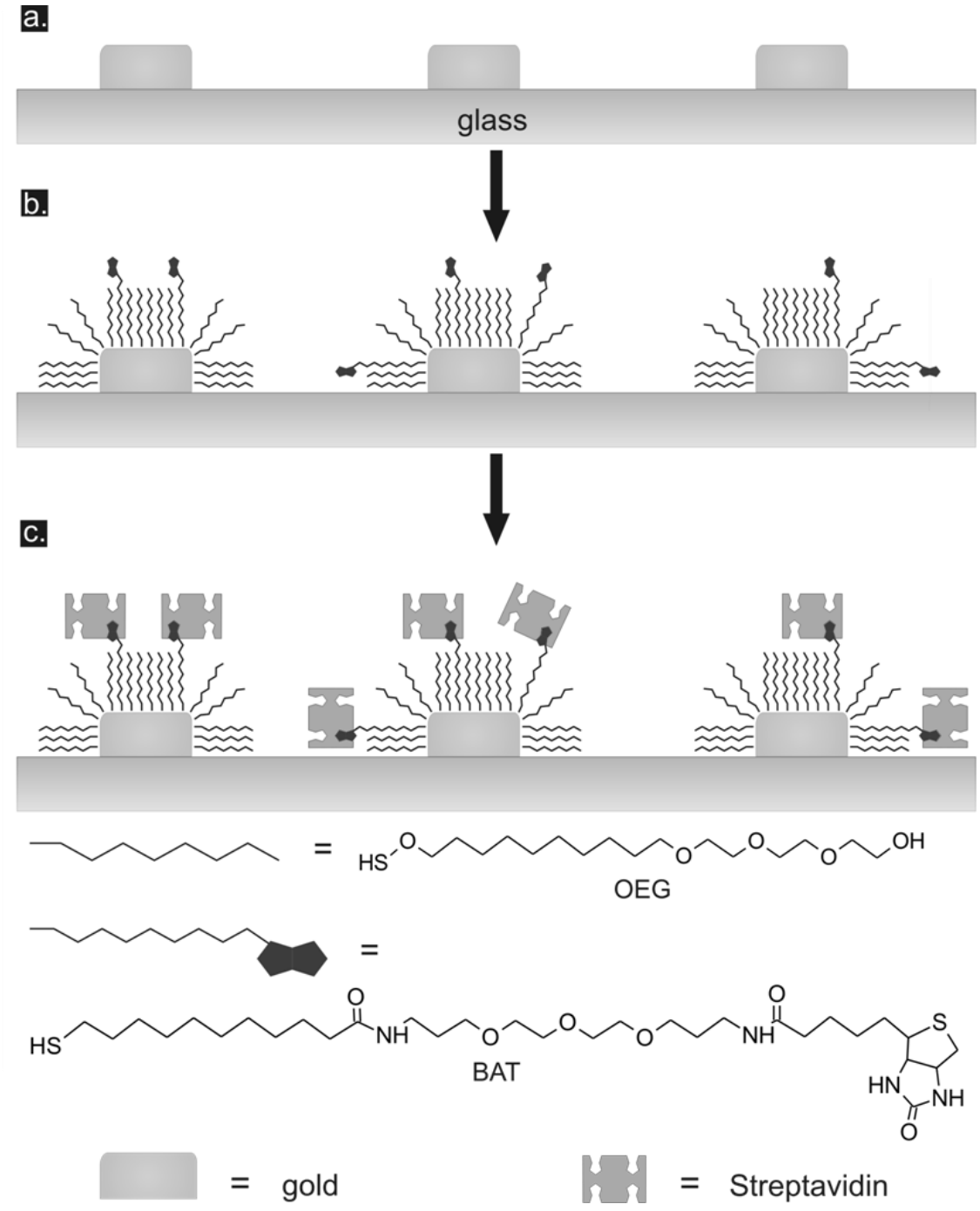

Figure 6.2. Sreptavidin/biotin functionalization process of nanostructured platforms.

Samples were cleaned with ethanol for approximately 30 minutes. Then, they were immersed in an 5 x10^{-4} M alkanethiol ethanolic solution (OEG:BAT 9:1 ratio) for twelve

hours, and rinsed thoroughly with ethanol (**Figure 6.2.b**). The adsorption of the host protein was accomplished by immersing the functionalized samples in a 5 x 10^{-7} M Strep solution in PBS for two hours, and washed several times with PBS solution. Finally, the samples were softly blown dry with air (**Figure 6.2.c**).

6.6.2.2. Aptamer/OTA System.

Methanol (HPLC grade), $CaCl_2$, KOH, KCl NaCl, and Tris(hydroxymethyl)aminomethane (Trizma® pH 8.4) were obtained from Sigma-Aldrich. Nano-strip solution was purchased from Cyantek Inc. Alkanethiolate-36-DNA oligonucleotide (HS-Apt = 5′-HS-$(CH_2)_6$-GAT-CGG-GTG-TGG-GTG-GCG-TAA-AGG-GAG-CAT-CGG-ACA-3′) was synthesized and HPLC-purified by Eurogentec (Angers, France). The identity of the modified oligonucleotides was confirmed by MALDI-TOF mass spectrometry.[96] Ochratoxin A from *Aspergillus ochraceus* was obtained from A.G. Scientific, Inc. Doubly distilled deionized water (DDDI) was obtained from the Nanofabrication facility at UWO.

Samples were rinsed in Nano-strip solution for at least 3 minutes at 80 °C, then washed with DDDI and blown dry with nitrogen. A 1 mM H-S-Apt stock solution in DDDI was prepared and stored at -15 °C Then, a fresh 1 x10^{-6} M HS-Apt in Tris buffer solution (TBS = 10 mM Trizma, 120 mM NaCl, 120 mM $CaCl_2$, 5 mM KCl at pH 8.5) was prepared at r.t.to functionalized the gold surfaces. Samples were immersed in this solution for ~4 hours. SERS platforms integrated in a microfluidic device were first washed with 200 µL of TBS, dried, and then 100 µL x 2 of HS-Apt at the same concentration as for the other samples was flowed through the channel for 4 hrs. For all samples, after functionalization, the surfaces were washed several times with TBS. A 24.7 mM OTA stock solution in methanol was prepared, and a final concentration of 2.5 µM in 0.001%methanol, 99.999% TBS was used in all the aptamer functionalized surfaces. In the case of the functionalized bare gold surfaces and SERS platforms, the samples were immersed in the OTA solution for 2 hours, and then washed several times with TBS, and finally blown dry with nitrogen. The adsorption of OTA in the aptamer-functionalized

SERS devices was done by flowing through the channels 50 μL x 2 solution of OTA for one hour and then washed three times with TBS and let it dried. . All the samples used for ellipsometry measurements had an additional step, before drying they were washed thoroughly with DDDI.

6.6.3. Fabrication of microfluidic SERS device

6.6.3.1. PDMS microfluidic channel layer

The microfluidic channels were prepared by conventional soft lithography techniques. The first step requires the fabrication of a negative master mold of the channels. Five inch silicon wafers were cleaned with Nano-strip (Cyantek Inc.) for 10 minutes at 80 ℃ and washed thoroughly with DDDI, and blown dry. Then the mold was prepared by spin casting a 20 nm layer of KMPR® 1025 negative photoresist (MicroChem[97]) on the cleaned wafers at 500 rpm for 8 seconds (spread) and 4000 rpm for 45 seconds (spin) using a Solitec 5110 spin coater (Solitec Wafer Processing) and soft baking the substrate at 100 ℃ for 15 minutes. The channel designs were obtained by exposure to 365 nm wavelength light through a photomask (Photoplot Store[98]) for 385 seconds at a power of 4 mW/cm^2 using a Karl Suss MA6 photolithography system. The exposed sample was then baked at 100 ℃ for 2 minutes. Finally the negative master mold was revealed after cleaning it with SU-8 developer (MicroChem[97]) at 500 rpm for 360 seconds and DDDI water at 500 rpm for 90 seconds using a Solitec 5110 developer (Solitec Wafer Processing), and blown dry with nitrogen. The microfluidic channels are then obtained by pouring a 10:1 mass ratio mixture of PDMS precursors Sylgard 184A and B (A.E. Blake Sales Ltd.) in the master mold. Then, the poured prepolymer was degassed at r.t. for 2 hours and then cured at 75 ℃ for 90 minutes in an oven, at which point the cured PDMS layer was peeled off carefully from the master mold. A summary of all the different steps of the process is illustrated in **Figure 6.3**.

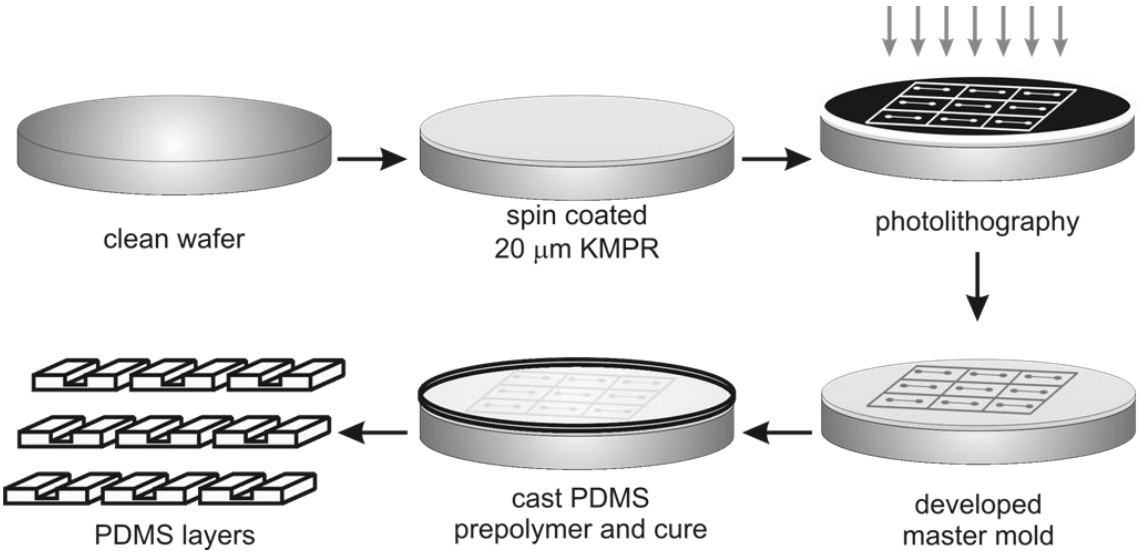

Figure 6.3. Fabrication process of master mold by photolithography and casting of PDM layers.

6.6.3.2. SERS platform microfluidic integration

The bonding between the PDMS microfluidic channel layer and the SERS platforms was done following a procedure described in the literature.[99] In short, the PDMS layer went through surface plasma modification. The PDMS layers were placed in a sputter system (Edwards Auto 500 Magnetron Sputtering System) operated at 300 W and 4.8 mTorr with Ar gas flowing at 15 sccm rate. The samples were exposed to the plasma for 5 minutes to enrich the silanol surface, and then the shutter was open to protect the modified surface with a 44 ± 3 nm aluminium layer. Prior the bonding between the glass and PDMS layer, fluid access ports were generated by boring holes through the PDMS layer using syringe needles 20 G (Fisher scientific Canada). The aluminium layer was etched with 1.8 M orthopohosphoric acid (Sigma-Aldrich) for 40 minutes and rinsed three times in DDDI and blown dry. In the case of the SERS platform, the surface was rinsed in Nano-strip at r.t. for 3 minutes, carefully washed with DDI and blown dry prior the bonding. Both layers were then aligned using an optical microscope (Leitz Microscope 3.5x/0.15p) and soft bake in a hot plate at 90 °C for 1 hour with light pressure. A summary of the binding process and a picture of the device are shown in **Figure 6.4**.

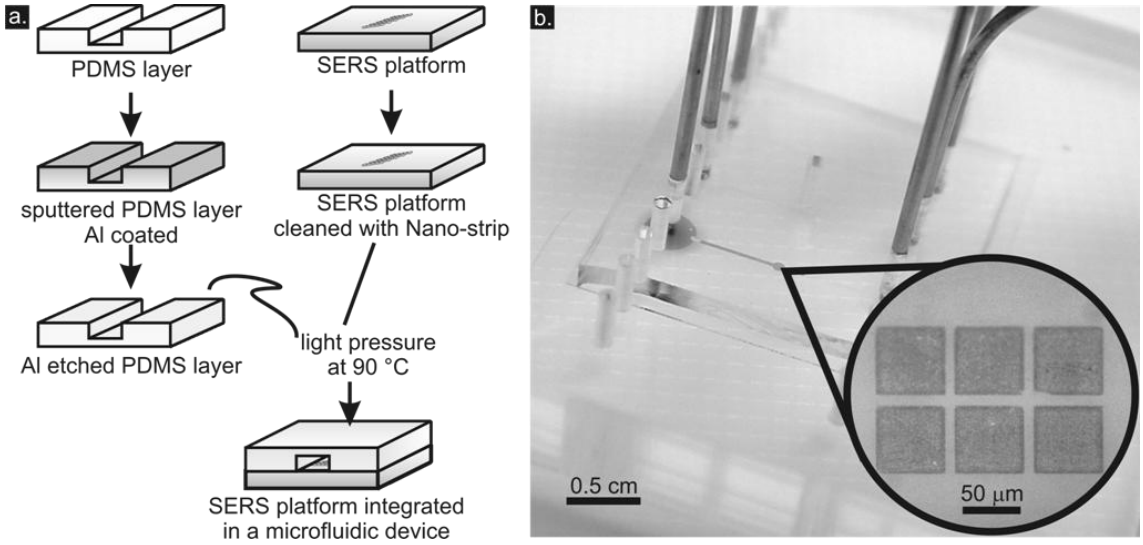

Figure 6.4. Binding process of SERS platforms and DPMS microfluidic layer (a) and optical picture of the assembled device.

6.6.4. Physical characterization

6.6.4.1. Structural analysis

Images were acquired using a scanning electron microscope (SEM), LEO 1530 Field Emission, with a 1.5-3.0 keV field-emission electron source. Atomic force microscopy (AFM) images were collected on a NanoWizard® II Bioscience AFM (JPK Instruments Inc.) in contact mode using a CONT-20 cantilever (k=0.2 N/m, Nano World Inc.). For each sample used in the Streptavidin/biotin experiment, SEM and AFM scans were performed on several surface positions to check the surface uniformity. The average size values are the result of at least ten different measurements on different spots of the scanned areas.

6.6.4.2. Ellipsometry

Silicon substrates were coated with a 3 nm interlayer of chromium and 100 nm layer of gold using an e-beam evaporation system (DOC) at a rate of 1Å/s and functionalzed with alkanethiolated aptamers as described in Section 6.6.3. A ellipsometer Model L116C (Gaertner Scientific Corporation), which was setup with a 632.8 nm laser, at 70° angle of incidence. A refractive index of 1.45 was assumed for all the organics used to determine the thickness and surface coverage of the gold surfaces, as well as to infer the adsorption of OTA on the functionalized surfaces. The results shown are the average of at least seven different measurements.

6.6.5. Finite difference time domain (FDTD) calculations

The relative electric field intensity distribution of the fabricated nanopattern was calculated with FDTD method (FDTD Solutions software from Lumerical), following the same conditions for the material and boundary parameters as described in Section 3.4. In short the simulation here mimics a plane wave source with an excitation input at 550-750 nm, which propagates perpendicular to the plane of the platform, and with a polarization parallel to the interparticle distance axis of the triangles.

6.6.6. Extinction spectra

The LSPR bands of the samples were determined from the extinction spectra. A detailed description of the experiment was given in Section 2.4.3. In short, a halogen lamp source illuminates the sample with a collimated beam of 60 microns diameter. The transmitted light is then collected by a microscope objective prior to analysis by the spectrometer in the 400-800 nm spectra range. Typically, each spectrum is the result of 30 accumulations. The extinction spectra of the SERS platforms integrated in the microfluidic devices was obtained before the binding process with the channel.

6.6.7. Raman spectroscopy

Vibrational Raman spectra were recorded with a LabRAM HR (Horiba Scientific) spectrometer equipped with a Helium-Neon (He-Ne) laser (λ= 632.8 nm), a 600 grooves per mm grating and a 40x/N.A 0.75 objective. Raman intensities were measured with an accuracy of about 1.2 cm^{-1}. The conditions for the different Raman spectra taken are summarized in **Table 6.2**. In all the SERS experiments, a careful control over the orientation of the platform was taken in order to have the polarizer of the input laser parallel to a bow tie axis.

Table 6.2. Experimental conditions of the Raman spectra taken.

sample	laser power (mW)	irradiation time (s)	accumulations
$Strep_{(solid)}$	1.1	1	30
BAT:OEG on bare gold	~0.06	1	3
SERS of BAT:OEG SAM	~0.06	1	3
SERS of $Strep_{(ads)}$ on OEG:BAT SAM	~0.06	1	10
$OTA_{(solid)}$	1.1	50	10
Apt on bare gold	~0.06	20	50
SERS of Apt SAM	~0.06	20	20
SERS of $OTA_{(ads)}$ on Apt SAM	~0.06	20	20

6.6.8. Fluorescence spectroscopy

Tris(hydroxymethyl)aminomethane, $CaCl_2$ and OTA were purchased from Sigma Aldrich (Saint-Quentin, France). KCl and NaCl were obtained from Prolabo (Paris, France) and Chimie-Plus laboratoires (Bruyères de Pouilly, France) respectively. Water was obtained from a Purite Still Plus water purification system (Thame, U.K.) fitted with a reverse osmosis cartridge. Fluorescein (F-Apt = 5′-F-GAT-CGG-GTG-TGG-GTG-GCG-TAA-AGG-GAG-CAT-CGG-ACA-3′) labeled 36-DNA aptamer and the corresponding

scrambled strand(F-Scr = 5'-F-GGC-ATA-GAG-GCG-GCG-AGA-GGT-CTG-TCA-GGT-GTA-GAG-3')[96] were synthesized and HPLC-purified by Eurogentec (Angers, France). The identity of the modified oligonucleotides was confirmed by MALDI-TOF mass spectrometry. Fluorescence anisotropy readings were taken on a Tecan Infinite F500 microplate reader (Männedorf, Switzerland) using black, 96-well Greiner Bio-One microplates (ref: 675086, Courtaboeuf, France). Excitation was set at 485 ± 20 nm and emission was collected with 535 ± 25 nm bandpass filters.

All fluorescence experiments were performed entirely by our collaborators.[100] A summary of the experiment is described here in short. The binding buffer consisted in 10 mM Tris-HCl, pH 8.75, 120 mM NaCl, 5 mM KCl, 120 mM $CaCl_2$. The aptamer solutions were prepared in water and stored at -20 °C. The working aptamer solutions were obtained by adequate dilution of the stock solution in 1.25× concentrated binding buffer. Prior their first use, the working solutions were heated at 80 °C for 5 minutes and left to stand at room temperature for 30 minutes. OTA was first dissolved in absolute methanol and then diluted in water. All solutions were filtered prior to use through 0.45 µm membranes. To construct the titration curves, the aptamer and analyte solutions were mixed into the individual wells (final volume: 100 µL) at room temperature. Blank wells of the microplate received 100 µL of the binding buffer. Aptamer probe concentration was set to 10 nM, and the OTA concentration range goes from 5 to 2000 nM. The microplate was immediately placed into the microplate reader for the measurement. All experiments were done in triplicate.

6.7. Results and discussion

6.7.1. Optimization of SERS platforms

The gold nanostructured platforms were physically and optically characterized. The SEM (**Figure 6.5.a**) and AFM images suggest a length of 310 ± 35 nm for each triangle, an interparticle distance of 91 ± 10 nm and a gold thickness of 45 ± 1 nm. Previous studies

suggest the highest enhancement factor occurs when the irradiation source is at slightly lower wavelength than the plasmon band.[101] FDTD calculations (**Figure 6.5.b**) shows the distribution of the electric field intensity at ~634 nm excitation input over the structure.[102]

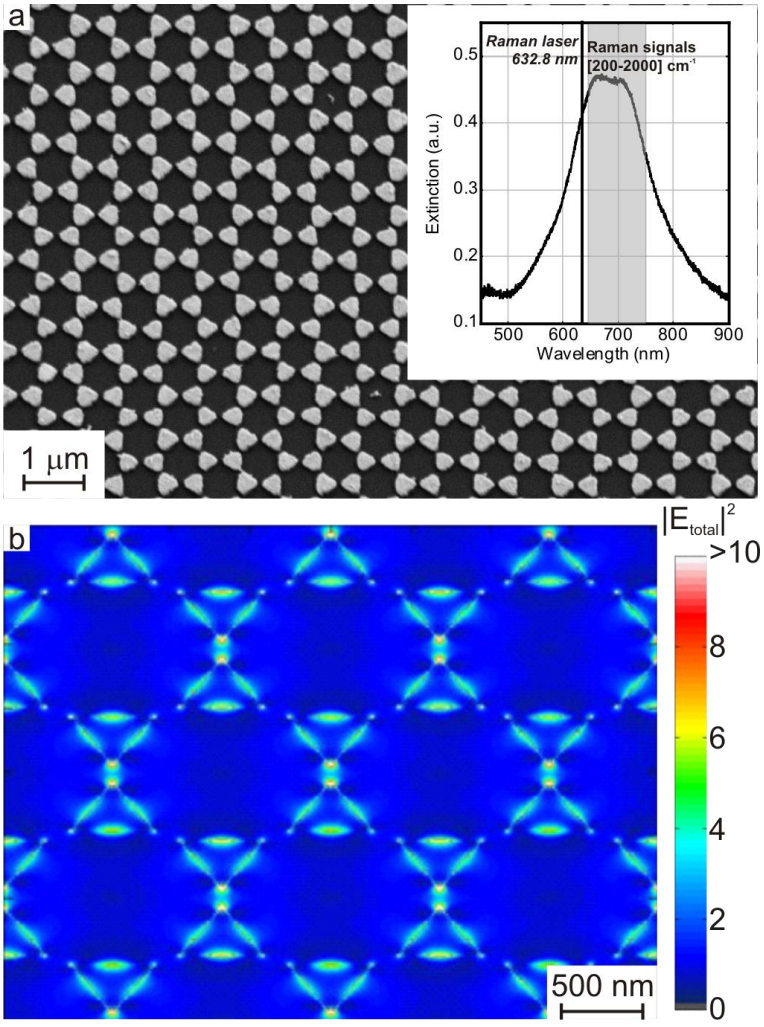

Figure 6.5. SEM image of fabricated array of gold nanotriangles over a glass slide. The inset plot shows the extinction spectrum of the platform together with the Raman excitation wavelength (λ= 632.8 nm) and the Raman signals regions used for the Raman experiment (a). Localization of the hot spot spots over a lattice unit of the SERS platform The input linear polarization direction is along a bow tie axis (b).

In these calculations, the impinging field was chosen to be linearly polarized along the interparticle distance axis and with a normal incidence. The calculated electric field intensity distribution shows larger local enhancement in the vicinity around a pair of triangles for a polarization set along the bow tie interparticle distance. This implies that the molecules that sense this electromagnetic enhancement are probably localized closer to the junction of the bow tie assembly and are oriented either parallel to the surface of the substrate and perpendicular to the gold surface as shown in the cross section of the SERS platform in **Figure 6.4**.[101] Therefore, the polarization input was also selected so that the linearly polarized light is parallel to the bow tie symmetry axis (y axis). In such conditions the enhancement was optimized and the presence of hot spots is expected at the locations of the junction between the triangles.

6.7.2. Streptavidin/biotin monolayer assemblies

6.7.2.1. Topographical analysis

The AFM scans allow one to probe the surface modification through the different functionalization steps of the gold nanostructures. The surface analysis of the reference clean gold nanostructured platform, the functionalized samples, and the Strep adsorbed on the substrates are shown in **Figure 6a-c**, respectively. The results suggest an increase in the height of the features on the gold structures after each step. The height difference (Δ Height) after the functionalization of the sample with the alkanethiol mixture is ~1 nm, and 2.1 nm when the Strep is adsorbed on the platform and compared with the clean sample (**Figure 6.6.d**). These values are small in contrast with the measured height of the gold nanostructures (~45 nm) but coincide with similar experiments reported in the literature.[103] In addition, the average roughness of the samples (Ra) increases from 1.9 to 3.8 nm when the Strep is assembled on the biotinylated platforms, such an increase has been observed for other gold structures modified with a Streptavidin-biotin system.[104] Both results suggest the nanostructured platform was functionalized with a self-assembled monolayer (SAM) of alkanethiols containing biotinylated groups that can selectively bind to Strep and which can therefore be further characterized by using Raman spectroscopy.

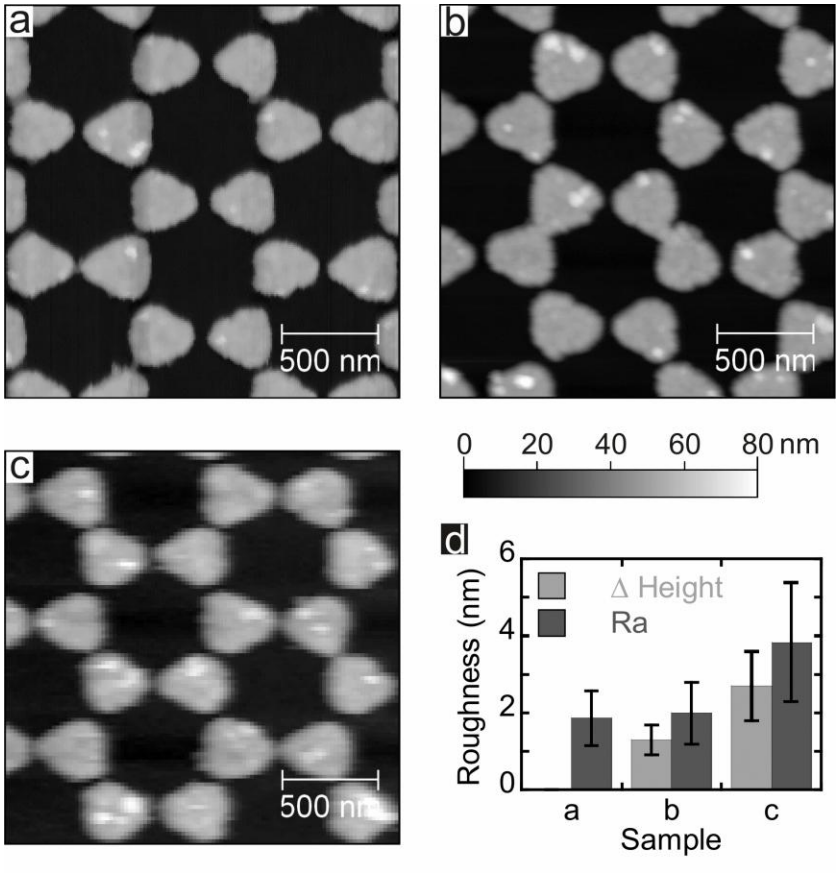

Figure 6.6. AFM scans of the gold nanostructured platforms before (a) and after being functionalized with BAT:OEG mixture (b), and when Strep assembled with the BAT molecules (c).The graph (d) summarizes the height difference and the average arithmetic roughness value (Ra) of samples a-c.

Raman spectroscopy. Beyond providing the vibrational fingerprints of a molecular material, Raman spectroscopy is also sensitive to the interaction between the biotinylated groups with the Streptavidin host protein. Thorough studies led by Fini and coworkers focused on this complex assembly in solution.[23,47,105,106] However in the case of a monolayer, located at a metal surface, interactions of the Strep/BAT complex on the gold substrate may lead to some changes of the Raman spectra due to a more anisotropic orientation of the probed molecules than when dissolved in solution. Therefore it is

expected that the assignment as well as the intensity and frequency of the vibrational band may be altered.[24,41,105]

The spectrum of the solid Strep (**Figure 6.7.a**) was first obtained as a reference and the signals have been identified and assigned on **Table 6.3** ($Strep_{(s)}$). The relative intensity values reported in **Table 6.3** have been normalized by assuming that the intensity at 1449 cm^{-1} of the δ-CH_2 band is unaffected by structural changes.[41] These bands have been previously described in the literature[23,24,41,47,105] for the amide III and amide I regions, as well as for the different protein residues. In the present sample, some of these Raman bands are susceptible to changes in conformation once Strep is linked to BAT and make possible to study their interaction. The presence of the adsorbed Strep ($Strep_{(ads)}$) on a functionalized gold surface was studied by SERS. The result (**Figure 6.7.a**, **Table 6.3**) is a complex Raman spectrum where both contributions of Strep and BAT:OEG are present with some overlapping (**Figure 6.7.b**, **Table 6.3**). Yet, it is possible to detect specific regions on the spectrum that only correspond to Strep/BAT binding.

The supramolecular interaction between Streptavidin and biotin is observed when the changes in the secondary structure of the protein alter the amide regions of the Streptavidin spectrum. Such is the case of the amide III signals in the 1230-1280 cm^{-1} region, that become less intense at 1238 cm^{-1} under the presence of biotin which presumably induces the decrease of the amount of the β-sheet conformation, while the intensity of the α-helix increases at 1279 cm^{-1}.[105] The spectral domain of the amide I (1630-1700 cm^{-1}) is also altered when the complex is formed, by a increase in the α-helix conformation and a decrease of the β-sheet.[41] In addition, the bands assigned to different tryptophan residues on Strep get slightly modified when interacting with biotin, like Trp18,[24] Trp17,[107] Trp13,[24,41] Trp7,[41,108] Trp5,[24] and Trp2,[41] that become less intense or slightly shifted. These changes have been previously interpreted as a result of a change to a more hydrophobic environment when biotin is added.[24,41]

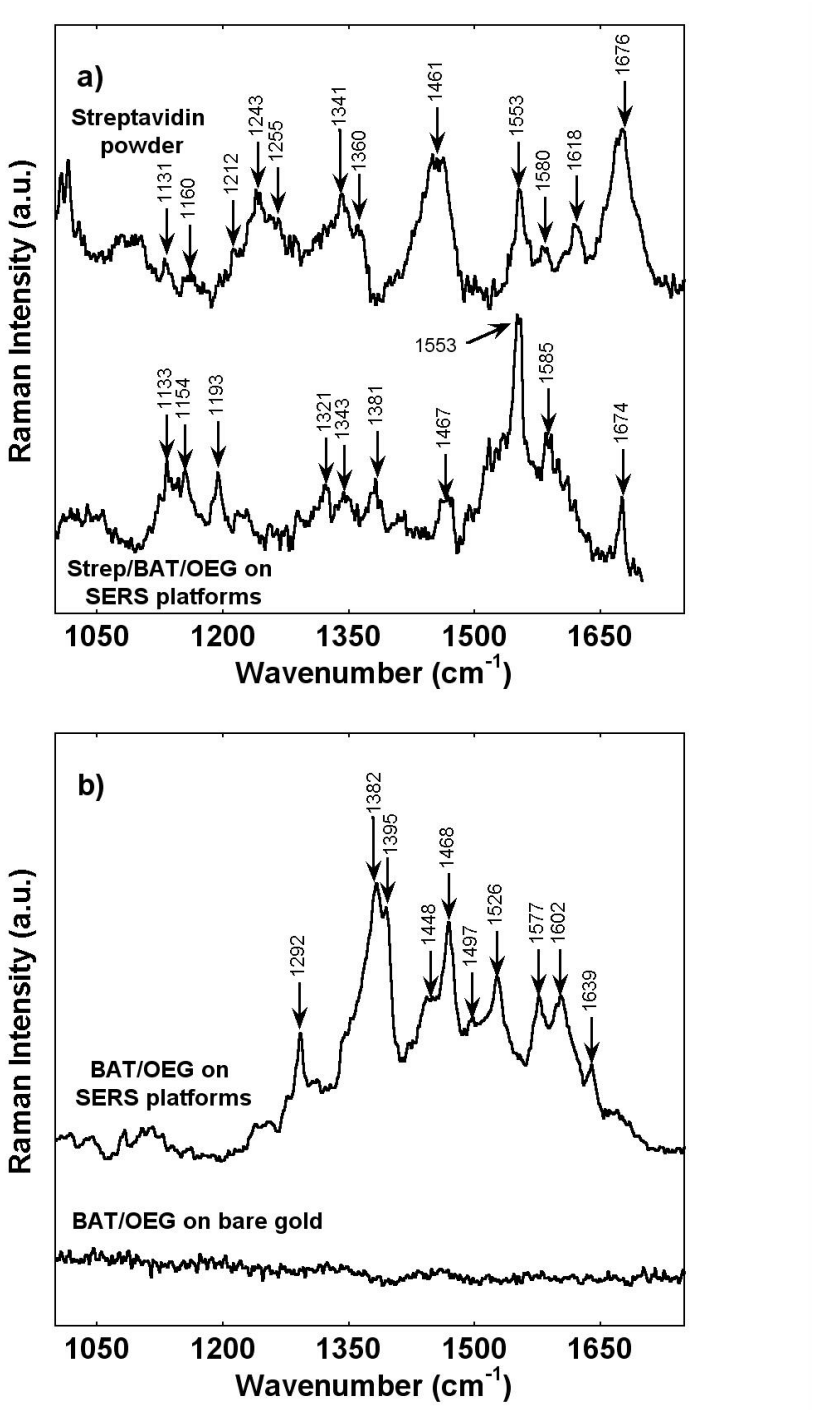

Figure 6.7. Raman spectra of Strep(s) and Strep(ads) on a functionalized gold SERS platform (a). Raman spectra BAT and OEG present at the surface of the gold SERS platform and at the surface of a bare gold substrate (b).

It is important to note, that in comparison with the spectrum of the $Strep_{(s)}$, where the number of probed molecules is only limited by the scanned volume region of the Raman system, the spectrum of the $Strep_{(ads)}$ is the result of probing just few molecules adsorbed in an already diluted SAM containing biotinylated groups. This makes the Raman experiment extremely challenging to obtain under normal conditions using a bare gold substrate (**Figure 6.7.b**) where no Raman bands were detected even at longer acquisition times. To overcome this problem, one can make use of the gold nanostructured arrays described herein as part of a SERS system, and be able to enhance the Raman signals of adsorbed molecules. Furthermore, it is important to remember that the relative intensities of the measured SERS signal cannot be directly compared to measurements done in solution. In rough metal surfaces the extension of the SERS effect above the metal surface would be limited to a few nanometers and the intensities of the Strep would presumably be less intense than the biotin located at the nanostructure due to a shielding effect of the BAT/OEG.

In addition to these observations, these plasmonic platforms are known to have maximum enhancement at the junctions of two facing metallic triangle (**Figure 6.5**). This means that the field enhancement varies locally but since we are not performing spatially resolved measurements, the SERS contributions are an average from the molecules adsorbed in different locations over the gold structure.

Table 6.3. Assignment of the Raman bands in the spectra of Strep, and Strep/BAT complex.

Wavenumber (cm^{-1})			Assignment	Reference
*$Strep_{(s)}$	*$Strep_{(ads)}$	*BAT:OEG		
761 (1.6)	760 (0.4)		Trp18	41
879 (3.0)	881 (2.6)		Trp17	41
1006 (3.4)	1007 (0.4)		Trp16	41
1015 (8.6)	1017 (2.3)		Trp1	46
1027 (2.2)	1027 (1.5)		Phe, Ser	41
1080 (1.7)	1080 (1.4)		Glu, Thr	41
		1082	ν-C-C	107
1101 (0.9)			Ala, Lys	41
1132 (0.3)	1132 (5.0)		ν-C-N, Trp13	41,46
1212 (0.6)	1213 (1.0)		Tyr7a	41
1239 (0.8)	1239 (0.1)		Amide III (β-sheet)	105
1243 (0.1)			Trp10	46
	1247 (0.7)	1248	Bio: ureido ring	107
1254 (0.8)	1254 (0.3)		Amide III (r. coil)	41
1279 (1.0)	1279 (2.8)		Amide III (α-helix)	41
		1292	ω-CH_2	107
1320 (1.5)	1320 (2.4)		Ser (γ-CH_2)	41
1341 (3.4)	1342 (1.2)		Trp7	38,41,46,105
1348 (0.7)	1348 (0.1)		Trp7	46
		1382	ω-CH_2	
1449 (1.0)	1447 (1.0)		δ-CH_2, δ-CH_3	41
1462 (1.7)	1462 (0.2)		Trp5	46
		1468	Bio: ν-CH_2-ring	107
1551 (7.6)	1551 (22.1)		Trp3	46
		1577	ν-C-N	46
1580 (0.9)	1582 (0.3)		Trp2	46
		1602	ωC=C	46
1618 (2.6)	1618 (0.9)		Trp1, Tyr8a	41
1637 (1.0)	1637 (0.4)		Amide I (β-sheet)	105
		1639	ν-C=O	107
1646 (0.6)	1646 (1.8)		Amide I (α-helix)	41
1668 (0.7)	1669 (0.6)		Amide I (r.coil)	41
1675 (3.8)	1675 (2.2)		Amide I (β-sheet)	41

*Raman signals of solid Strep ($Strep_{(s)}$) and of the complex Strep/BAT when adsorbed on a functionalized gold SERS platform ($Strep_{(ads)}$) shown on Figure 6.7.a, and the mixture of BAT and OEG present on the surface of the gold SERS platform (BAT:OEG), shown on Figure 6.7.b. The values reported in brackets represent the relative intensity of the signal when normalized with the intensity of δ-CH_2 at 1449 cm^{-1} that is assumed non-affected by structural changes.

6.7.3. OTA aptameric sensor

6.7.3.1. Surface functionalization

The coating of the gold surfaces with the alkanethiolated aptamer was first evaluated by ellipsometry. Although, different functionalization period were tested to determine the optimal conditions of surface coverage, no major change was observed when samples were immersed in the thiolate solution for longer time. The thickness of the SAM obtained through the ellipsometer measurements was 2.9 ± 0.1 nm, and comparable with other aptamers functionalized on gold surfaces in the literature.[40] Although, it was possible to detect a change in thickness after adding OTA (Δ = 1.0 ± 0.4 nm), this method is limited to suggest if the OTA molecules are binded to the aptameric sequence.

6.7.3.2. Fluorescence polarization target binding

To avoid any misinterpretation of the Raman signals and to prove the binding mechanism occurring between the anti-OTA aptamer and its target, a fluorescence polarization (FP) assay strategy dedicated to small molecule sensing was applied, according to a method described elsewhere.[62] This method is based on the conversion of the target binding event into a detectable fluorescence anisotropy signal (*f.a.s.*), calculated by the instrument software and mathematically described in **(2)**.[109]

$$f.a.s. = \frac{I_{vv} - GI_{vh}}{I_{vv} + 2GI_{vh}} \qquad \textbf{(2)}$$

Herein, I_{vv} and I_{vh} are the vertically and horizontally polarized components of the emission after excitation by vertically polarized light. The instrumental correction factor (G) was determined from standard solutions according to the manufacturer's instructions. Using these results, it is then possible to plot the anisotropy changes in the aptamer when different concentrations of OTA are added (**Figure 6.8**). The vertical axes in the plot represents a ratio of the anisotropy of the aptamer at various concentrations when the target molecules is present (R) over the anisotropy of the aptamer in the absence of the target molecule (R_f).

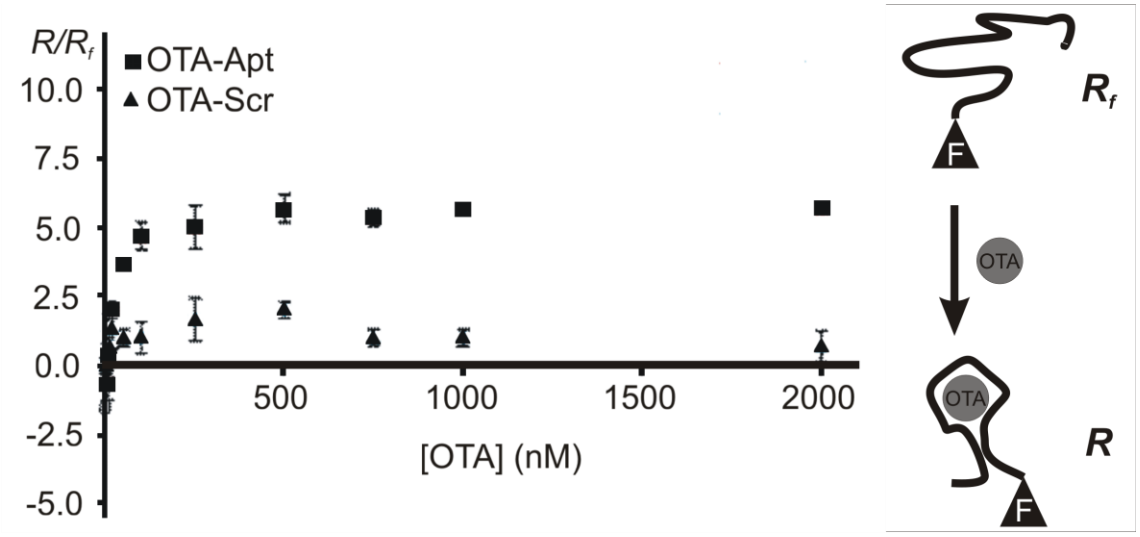

Figure 6.8. Effect of OTA on the fluorescence anisotropy of the aptamer.

From these measurements it is possible to detect an increase in the anistotropy ratio (R/R_f) at higher concentrations of OTA. In addition, a similar experiment was performed using a scramble aptameric sequence, which should not present any affinity for OTA. The results confirm that the binding process is responsible of the fluorescence polarization signal due to an obvious conformational change.

6.7.3.3. Raman spectroscopy

Although the previous two experiments confirmed that the aptamer sequence gets adsorbed on the gold surface by changing the thickness of the assembled layer, and that OTA specifically binds to such an aptamer by altering its conformation, the interaction between the Aptamer SAM and its target molecule has not been analyzed on a surface. Only one study has reported a similar surface system to the one presented in this project, but where the target molecule selected was thrombin.[31] Other reports done using SERS and aptamers that go through a G-quadruplex conformation to bind a target molecule do not consider the functionalization of the metallic nanostructures, and their results lie on

the formation of hot-spots in colloidal nanoparticles to enhance the Raman signal.[80,81] As a result, there is a limited amount of reference that can be used to identify the Raman signals of this particular system, and the assignment done considers any possible analogies between different aptameric systems as well as the work done for DNA strands.[110-114]

The Raman spectrum of solid OTA was taken as a reference. The results shown in **Figure 6.9.a** correspond to a spectrum obtained after a large number of accumulations, and processed by using a polynomial baseline correction and smoothing. Some of these signals have been reported in the literature as part of the vibrational fingerprint of the toxin, [115,116] and an analysis of its structure (**Figure 6.9.b**). Thus, the signal at 1028 cm^{-1} has been assign to C-Cl stretching mode, and the signals at 1530 and 1657 cm^{-1} more than likely correspond to the vibrational mode of the amide present in OTA in solid state. The carbonyl stretching mode of the lactone has been reported in the IR spectrum of OTA,[115] and here it can be detected as a weak signal. Other Raman bands that are detected as well correspond to the vibrational deformation (1000 cm^{-1})and stretching (1316 cm^{-1}) modes of the aromatic rings. It must be pointed out, that it is not expected to detect the vibrational signals of OTA once gets adsorbed in the aptameric surface. The reason for this is the distance between the target molecule and the region where the electric field is enhanced, and in LSPR this enhancement decays exponentially as it goes away from the surface. Therefore, more than likely only the signals from the aptamer will be detected and altered once the OTA binds to it.

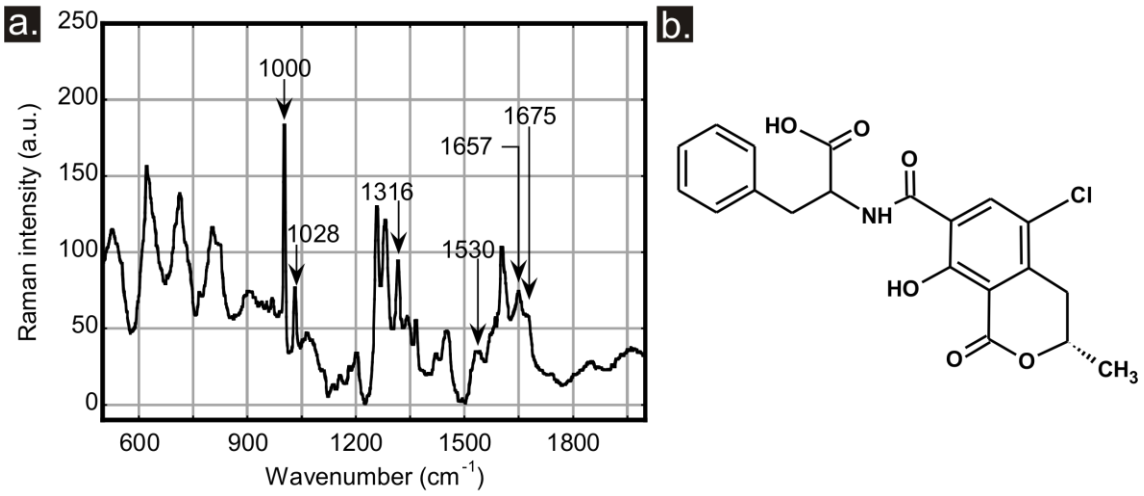

Figure 6.9. Raman spectrum (a) of ochratoxin-A (b) in solid state.

Taking advantage of the reduced amount of chemicals required to functionalize a surface once integrated in a microfluidic device, it was decided to functionalize the SERS platforms with the aptameric solution. Then, once this step was done and the device was cleaned with TBS, the SERS spectrum of the aptameric assembly was obtained, before an OTA solution was flowned through the channels and to record again the spectrum, this time of the aptamer/OTA (Apt/OTA) complex. The results are shown in **Figure 6.10** and in **Table 6.4**. In addition, **Figure 6.10** also shows the Raman spectrum of a bare gold surface functionalized with the same aptamer, and where it proves the difficulty of study the surface chemistry of these systems without enhancing the Raman signal. In a similar manner as performed on the Streptavidin/biotin study, the intensity of the signals were calculated and normalized in order to compare the spectra before and after the adsorption of OTA. In this case, all the intensity values were normalized with respect to the most intense signal in the spectra that seems unaffected by the interaction with OTA, the signal at 1617 cm^{-1}, and more than likely corresponding to a carbonyl stretching bond.[112]

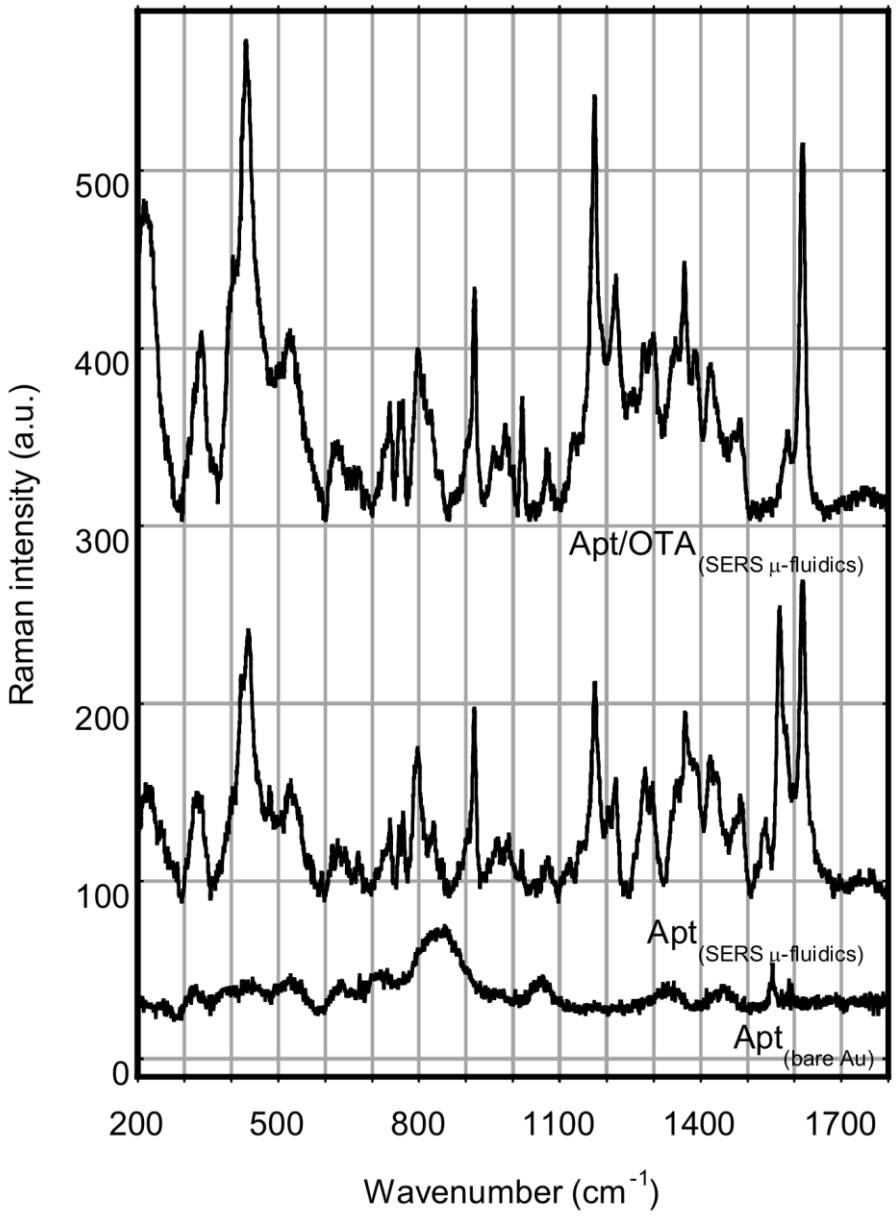

Figure 6.10. Raman spectra of aptamer SAM on bare gold surface ($Apt_{(bare\ Au)}$), aptamer SAM functionalized in a SERS platform integrated in a microfluidic device ($Apt_{(SERS\ \mu\text{-}fluidic)}$) and after OTA was adsorbed on this functionalized nanostructured platform($Apt/OTA_{(SERS\ \mu\text{-}fluidics)}$).

Table 6.4. Assignment of the Raman bands in the spectra of Aptamer and Aptamer/OTA complex.

$\bar{\nu}$ (cm^{-1})	Intensity[a]		Assignment	Reference
	*Apt	* Apt/OTA		
528	0.20	0.19	G out of plane	114
670	0.02	0.00	dG: C2' endo/syn	31,111
737	0.07	0.05	OPO stretching	114
757	0.07	0.04	C-sugar	114
764	0.09	0.07	OPO stretching	114
794	0.52	0.33	OPO symmetric stretching	31
830	0.05	0.04	sugar vibration C2' endo	31,110
918	0.49	0.49	G, sugar vibration	114
1018	0.06	0.22	dG, N-H deformation	31
1074	0.04	0.13	PO_2^- stretching (TGT loop)	31
1175	0.81	0.95	C-N ring vibration	113
1278	0.09	0.08	ring stretching, C-H deformation of T	31
1364	0.11	0.19	G deformation (N2)C2 endo anti	80,81
1390	0.08	0.11	ring stretching of G	112
1422	0.12	0.16	deoxyribosyl (C5') H-bond deformation	31
1484	0.25	0.13	C8=N7 H-bond deformation	81
1569	0.51	0.00	C2=N3 of G, (G4T4G4) complex	31,81
1586	0.02	0.03	G: N2-H interbase H-bond	81
1616	1.00	1.00	C=O stretching	112

*Raman signals of aptmaer (Apt) and aptamer/OTA complex (Apt/OTA) when adsorbed on a functionalized gold SERS platform integrated in a microfluidic device. [a] The intensity values reported in these columns represent the relative integral intensity of the signal when normalized with the intensity of the C=O stretching signal (1616 cm^{-1}) that is assumed non-affected by any surface modification.

The Raman spectrum of the surface functionalized with aptamers allows one to identify multiple signals belonging to the vibration of sugar residues present in the oligonucleotide.[31,110,114] The bands a 432, 757, 830, 918 and 1422 cm^{-1} are some of the vibrational modes of the different ribose and deoxyribosil residues present in the aptamer and that seem the least affected after OTA is adsorbed at the surface. Similarly some of the stretching modes of the phosphate groups, such as the 637 and 764 cm^{-1} that correspond to the phosphodiester (OPO) backbone stretching,[114] does not seem affected by the presence of OTA, while the band at 764 cm^{-1}, related to the symmetric stretching of the same OPO becomes slightly less intense.[31] Furthermore, the signal at 1074 cm^{-1}, assigned to the symmetric stretching mode of the ionized phosphate backbone (PO_2^-) and

to phosphate groups involved in a TGT loop that form the G-quadruplex conformation, is indeed affected and an increase in the intensity might suggest a proximity to the surface.[31]

Being the aptamer used rich in guanine (G) residues; it is not surprising to find several signals related to the vibrational modes of the different components of this nucleic acid. Thus, on one hand there are bands related to the vibrational mode of out of plane (528 cm^{-1}),[114] to the ring stretching of guanine (1390 cm^{-1}),[112] or to the stretching mode of deoxyguanosine (1586 cm^{-1}), are unaffected by OTA.[81,111] On the other hand, the spectrum also exhibits marker bands related to the G-quadruplex complex whose intensity is altered when OTA is added, these signals are assigned to the C2' endo/syn expected in an anti-parallel quadruplex (670 cm^{-1}),[31,111] to the N-H deformation (1018 cm^{-1})[31] or C2' endo/anti (1364 cm^{-1})[80,81] in deoxyguanosine; as well as the change in the bands related to the deformation of both C8=N7 (1484 cm^{-1}) and C2=N3 (1569 cm^{-1}) in the quadruplex (G4T4G4).[31,81]

6.8. Conclusion

This work demonstrates a successful approach leading to detection of good quality Raman spectra of complex surface systems such as Strep/BAT and Aptamer/OTA by using the fabricated SERS platforms developed in this project. It emphasizes the use of optical measurements, and more specifically spectroscopic measurements, in the fields of molecular recognition. The SERS platforms used in this study were successfully designed for optimal detection at the excitation wavelength and with a very good quality of reproducibility. No signal could be measured on the functionalized gold surface free of nanostructures.

In the case of the Strep/BAT system, the analysis of the various Raman bands from the amide regions, as well as from the tryptophan residues, confirms the change in the

environment of the protein to a more hydrophobic environment, and confirms the supramolecular assembly of this system.

The Raman study of the Aptamer/OTA surface complex system highlights some of the different interactions between the target molecule and the oligonucleotide. The results strongly suggest the presence of a G-quadruplex conformation for the aptameric sequence, which gets altered under the presence of OTA. As expected, the Raman signals from this target molecule were not detected in the spectrum of the complex system, confirming the relationship between the LSPR enhancement properties and the distance apart from the surface. However, the results suggest that the method established could be used to detect indirectly the presence of OTA.

Finally, the SERS platform produced on pristine glass cover slips were easily integrated on a microfluidic device and used in one of the studies done on complex surface systems. The fabrication method of this device shows the feasibility of the fabricated platforms and to be part of more complex analytical devices such as μ-TAS. Integration of other optical or electrical probes or dynamical studies of complexation/decomplexation cycles could be performed in such devices with volumes that do not exceed a couple hundred of microlitres.

6.9. References

(1) Fonder, G.; Cecchet, F.; Peremans, A.; Thiry, P. A.; Delhalle, J.; Mekhalif, Z.; *Surf. Sci.*, **(2009)**, *603*, 2276.

(2) Leitch, J.; Kunze, J.; Goddard, J. D.; Schwan, A.; Faragher, R. J.; Naumann, R.; Knoll, W.; Dutcher, J. R.; Lipkowski, J.; *Langmuir*, **(2009)**, *25*, 10354.

(3) Blaudez, D.; Buffeteau, T.; Cornut, J. C.; Desbat, B.; Escafre, N.; Pézolet, M.; Turlet, J. M.; *Thin Solid Films*, **(1994)**, *242*, 146.

(4) Moscovits, M.; *Rev. Mod. Phys.*, **(1985)**, *57*, 783.

(5) Moscovits, M.; *J. Raman Spectrosc.*, **(2005)**, *36*, 485.

(6) Gartia Manas, R.; Xu, Z.; Behymer, E.; Nguyen, H.; Britten Jerald, A.; Larson, C.; Miles, R.; Bora, M.; Chang Allan, S. P.; Bond Tiziana, C.; Liu, G. L.; *Nanotechnology*, **(2010)**, *21*, 395701 (9pp).

(7) Blackie, E. J.; Ru, E. C. L.; Etchegoin, P. G.; *J. Am. Chem. Soc.*, **(2009)**, *131*, 14466.

(8) Tripp, R. A.; Dluhy, R. A.; Zhao, Y.; *Nano Today*, **(2008)**, *3*, 31.

(9) Fleischman, M.; Hendra, P. J.; McQuilla, A. J.; *Chem. Phys. Lett.*, **(1974)**, *26*, 163.

(10) Jeanmaire, D. L.; Van Duyne, R. P.; *J. Electroanal. Chem.*, **(1977)**, *84*, 1.

(11) Wei, F.; Zhang, D.; Halas, N. J.; Hartgerink, J. D.; *J. Phys. Chem. B*, **(2008)**, *112*, 9158.

(12) Barhoumi, A.; Zhang, D.; Tam, F.; Halas, N. J.; *J. Am. Chem. Soc.*, **(2008)**, *130*, 5523.

(13) Cintra, S.; Abdelsalam, M. E.; Bartlett, P. N.; Baumberg, J. J.; Kelf, T. A.; Sugawara, Y.; Russell, A. E.; *Faraday Discuss.*, **(2006)**, *132*, 191.

(14) De Jesus, M. A.; Giesfeldt, K. S.; Oran, J. M.; Abu-Hatab, N. A.; Lavrik, N. V.; Sepaniak, M. J.; *J. Appl. Spectrosc.*, **(2005)**, *59*, 1501.

(15) Guieu, V.; Lagugné-Labarthet, F.; Servant, L.; Talaga, D.; Sojic, N.; *Small*, **(2008)**, *4*, 96.

(16) Yang, Y.; Tanemura, M.; Huang, Z.; Jiang, D.; Li, Z.-Y.; Huang, Y.-P.; Kawamura, G.; Yamaguchi, K.; Nogami, M.; *Nanotechnology*, **(2010)**, *21*, 325701.

(17) Min, Q.; Santos, M. J. L.; Girotto, E. M.; Brolo, A. G.; Gordon, R.; *J. Phys. Chem. C.*, **(2008)**, *112*, 15098.

(18) McFarland, A. D.; Young, M. A.; Dieringer, J. A.; Van Duyne, R. P.; *J. Phys. Chem. B*, **(2005)**, *109*, 11279.

(19) Ormonde, A. D.; Hicks, E. C. M.; Castillo, J.; Van Duyne, R. P.; *Langmuir*, **(2004)**, *20*, 6927.

(20) Yu, Q.; Golden, G.; *Langmuir*, **(2007)**, *23*, 8659.

(21) Wilchek, M.; Bayer, E. A.; Livnah, O.; *Immunol Lett.*, **(2006)**, *103*, 27.

(22) Barbucci, R.; Magnani, A.; Roncolini, C.; Silvestri, S.; *Biopolymers*, **(1991)**, *31*, 827.

(23) Torreggiani, A.; Bottura, G.; Fini, G.; *J. Raman Spectrosc.*, **(2000)**, *31*, 445.

(24) Clarkson, J.; Batchelder, D. N.; Smith, D. A.; *Biopolymers*, **(2001)**, *62*, 307.

(25) Brady, C. I.; Mack, N. H.; Brown, L. O.; Doorn, S. K.; *Anal. Chem.*, **(2009)**, *81*, 7181.

(26) Zhang, J.; Wang, L.; Pan, D.; Song, S.; Boey, F. Y. C.; Zhang, H.; Fan, C.; *Small,* **(2008)**, *4*, 1196.

(27) Baker, B. R.; Lai, R. Y.; Wood, M. S.; Doctor, E. H.; Heeger, A. J.; Plaxco, K. W.; *J. Am. Chem. Soc.,* **(2006)**, *128*, 3138.

(28) Neumann, O.; Zhang, D.; Tam, F.; Lal, S.; Wittung-Stafshede, P.; Halas, N. J.; *Anal. Chem.,* **(2009)**, *81*, 10002.

(29) Kim, N. H.; Lee, S. J.; Moskovits, M.; *Nano Lett.,* **(2010)**, *10*, 4181.

(30) Chen, J.; Jiang, J.; Gao, X.; Liu, G.; Shen, G.; Yu, R.; *Chem. Eur. J.,* **(2008)**, *14*, 8374

(31) Pagba, C. V.; Lanea, S. M.; Wachsmann-Hogiu, S.; *J. Raman Spectrosc.,* **(2010)**, *41*, 241.

(32) Xia, Y.; Gates, B.; Yin, Y. Self-Assembled Monolayers. In *Biochip Technology*; Cheng, J., Kricka, L. Y., Eds.; Hardwood Academic Publishers: Philadelphia, PA, 2001; pp 39.

(33) Porter, M. D.; Bright, T. B.; Allara, D. L.; Chidsey, C. E. D.; *J. Am. Chem. Soc.,* **(1987)**, *109*, 3559.

(34) Ostuni, E.; Yan, L.; Whitesides, G. M.; *Colloids Surf., B* **(1999)**, *15*, 3.

(35) Wink, T.; van Zullen, S. J.; Bult, A.; van Bennekom, W. P.; *Analyst,* **(1997)**, *122*, 43R.

(36) Nuzzo, R. G.; Zegarski, B. R.; Dubois, L. H.; *J. Am. Chem. Soc.,* **(1987)**, *109*, 733.

(37) Jadzinsky, P. D.; Calero, G.; Ackerson, C. J.; Bushnell, D. A.; Kornberg, R. D.; *Science,* **(2007)**, *318*, 430.

(38) Yang, Z.; Frey, W.; Oliver, T.; Chilkoti, A.; *Langmuir,* **(2000)**, *16*, 1751.

(39) Ochsenkühn, M. A.; Campbell, C. J.; *Chem. Commun.,* **(2010)**, *46*, 2799.

(40) Balamurugan, S.; Obubuafo, A.; Soper, S. A.; McCarley, R. L.; Spivak, D. A.; *Langmuir,* **(2006)**, *22*, 6446.

(41) Fagnano, C.; Torreggiani, A.; Fini, G.; *Biospectroscopy,* **(1996)**, *2*, 225.

(42) Green, N. M.; *Methods Enzymol.,* **(1990)**, *184*, 51.

(43) Wu, S.-C.; Ng, K. K.-S.; Wong, S. L.; *Proteins,* **(2009)**, *77*, 404.

(44) Mittler-Neher, S.; Spinke, J.; Liley, M.; Nelles, G.; Weisser, M.; Back, R.; Wenz, G.; Knoll, W.; *Biosens.Bioelectron.,* **(1995)**, *10*, 903.

(45) Busse, S.; Kashammer, J.; Kramer, S.; Mittler, S.; *Sens. Actuators, B,* **(1999)**, *60*, 148.

(46) Boozer, C.; Yu, Q.; Chen, S.; Lee, C.-Y.; Homola, J.; Yee, S. S.; Jiang, S.; *Sens. Actuators, B,* **(2003)**, *90*, 22.

(47) Torreggiani, A.; Fini, G.; *J. Mol. Struct.,* **(1999)**, *480-481*, 459.

(48) Barbillon, G.; Bijeon, J. L.; Plain, J.; Lamy de la Chapelle, M.; Adam, P.-M.; Royer, P.; *Gold Bull.,* **(2007)**, *40*, 240.

(49) Ellington, A. D.; Szostak, J. W.; *Nature*, **(1990)**, *346*, 818.

(50) Tuerk, C.; Gold, L.; *Science*, **(1990)**, *249*, 505.

(51) Yamamoto, R.; Katahira, M.; Nishihira, A.; Baba, T.; Taira, K.; Kumar, P. K. R.; *Genes Cells,* **(2000)**, *5*, 371.

(52) Fukuda, K.; Vishnuvardhan, D.; Sekiya, S.; Hwang, J.; Kakiuchi, N.; Kazunari, T.; Shimotohno, K.; Kumar, P. K. R.; Nishikawa, S.; *Eur. J. Biochem.,* **(2000)**, *267*, 3685.

(53) Bock, L. C.; Griffin, L. C.; Latham, J. A.; Vermaas, E. H.; Toole, J. J.; *Nature,* **(1992)**, *355*, 564.

(54) Torres-Chavolla, E.; Alocilja, E. C.; *Biosens. Bioelectron.,* **(2009)**, *24*, 3175.

(55) Geiger, A.; Burgstaller, P.; vonderEltz, H.; Roeder, A.; Famulok, M.; *Nucleic Acids Res.,* **(1996)**, *24*, 1029.

(56) Ueyama, H.; Takagi, M.; Takenaka, S.; *J. Am. Chem. Soc.,* **(2002)**, *124*, 14286.

(57) Cruz-Aguado, J. A.; Penner, G.; *Anal. Chem.,* **(2008)**, *80*, 8853.

(58) Merino, E. J.; Weeks, K. M.; *J. Am. Chem. Soc.,* **(2005)**, *127*, 12766.

(59) Nutiu, R.; Li, Y.; *Angew. Chem. Int. Ed.,* **(2005)**, *44*, 5464.

(60) Shlyahovsky, B.; Li, D.; Weizmann, Y.; Nowarski, R.; Kotler, M.; Willner, I.; *J. Am. Chem. Soc.,* **(2007)**, *129*, 3814.

(61) Tang, Z.; Mallikaratchy, P.; Yang, R.; Kim, Y.; Zhu, Z.; Wang, H.; Tan, W.; *J. Am. Chem. Soc.,* **(2008)**, *130*, 11268.

(62) Ruta, J.; Perrier, S.; Ravelet, C.; Fize, J.; Peyrin, E.; *Anal. Chem. ,* **(2009)**, *81*, 7468.

(63) Perrier, S.; Ravelet, C.; Guieu, V.; Fize, J.; Roy, B.; Perigaud, C.; Peyrin, E.; *Biosens. Bioelec. ,* **(2010)**, *25*, 1652.

(64) Zhu, Z.; Ravelet, C.; Perrier, S.; Guieu, V.; Roy, B.; Perigaud, C.; Peyrin, E.; *Anal. Chem.,* **(2010)**, *82*, 4613.

(65) Cruz-Aguado, J. A.; Penner, G.; *J. Agric. Food Chem.,* **(2008)**, *56*, 10456.

(66) De Girolamo, A.; McKeague, M.; Miller, J. D.; DeRosa, M. C.; Visconti, A.; *Food Chemistry,* **(2011)**, *127*, 1378.

(67) Wang, L.; Chen, W.; Ma, W.; Liu, L.; Ma, W.; Zhao, Y.; Zhu, Y.; Xu, L.; Kuang, H.; Xu, C.; *Chem. Commun.,* **(2011)**, *47*, 1574.

(68) Rhouati, A.; Paniel, N.; Meraihi, Z.; Marty, J.-L.; *Food Control*, **(2011)**, *22*, 1790.

(69) Sheng, L.; Ren, J.; Miao, Y.; Wang, J.; Wang, E.; *Biosens. Bioelectron.,* **(2011)**, *26*, 3494.

(70) Barthelmebs, L.; Jonca, J.; Hayat, A.; Prieto-Simon, B.; Marty, J.-L.; *Food Control*, **(2010)**, *22*, 737.

(71) Ikebukuro, K.; Kiyohara, C.; Sode, K.; *Anal. Lett,* **(2004)**, *37*, 2901.

(72) Wang, Z.; Duan, N.; Hun, X.; Wu, S.; *Anal. Bioanal. Chem.,* **(2010)**, *398*, 2125.

(73) Du, Y.; Li, B.; Wang, F.; Dong, S.; *Biosens. Bioelectron.,* **(2009)**, *24*, 1979.

(74) Zuo, X.; Xiao, Y.; Plaxco, K. W.; *J. Am. Chem. Soc.,* **(2009)**, *131*, 6944.

(75) Sassolas, A.; Blum, L. J.; Leca-Bouvier, B. D.; *Electroanalysis*, **(2009)**, *21*, 1237.

(76) Bonel, L.; Vidal, J. C.; Duato, P.; Castillo, J. R.; *Biosens. Bioelectron.,* **(2011)**, *26*, 3254.

(77) Yang, C.; Wang, Y.; Marty, J.-L.; Yang, X.; *Biosens.Bioelec.* , **(2011)**, *26*, 2724.

(78) Zhang, J.; Wang, L.; Pan, D.; Song, S.; Boey, F. Y. C.; Zhang, H.; Fan, C.; *Small,* **(2008)**, *4*, 1196.

(79) Wanga, G.; Wanga, Y.; Chena, L.; Choo, J.; *Biosens. Bioelectron.,* **(2010)**, *25*, 1859.

(80) Breuzard, G.; Millot, J.-M.; Riou, J.-F.; Manfait, M.; *Anal. Chem.,* **(2003)**, *75*, 4305.

(81) Wei, C.; Jia, G.; Yuan, J.; Feng, Z.; Li, C.; *Biochemistry*, **(2006)**, *45*, 6681.

(82) Pfohl-Leszkowicz, A.; Manderville, R. A.; *Mol Nutr Food Res,* **(2007)**, *51*, 61.

(83) Hernandez Hierro, J. M.; Garcia-Villanova, R. J.; Rodriguez Torrero, P.; Toruno Fonseca, I. M.; *J Agric Food Chem,* **(2008)**, *56*, 751.

(84) Serra Bonvehi, J.; *J Agric Food Chem,* **(2004)**, *52*, 6347.

(85) Medina, A.; Valle-Algarra, F. M.; Gimeno-Adelantado, J. V.; Mateo, R.; Mateo, F.; Jimenez, M.; *J. Chromat. A,* **(2006)**, *1121*, 178.

(86) Zezza, F.; Longobardi, F.; Pascale, M.; Eremin, S. A.; Visconti, A.; *Anal. Bioanal. Chem.,* **(2009)**, *395*, 1317.

(87) Kabak, B.; *Food Chem Toxicol* **(2009)**, *47*, 348.

(88) Noonim, P.; Mahakarnchanakul, W.; Nielsen, K. F.; Frisvad, J. C.; Samson, R. A.; *Int J Food Microbiol* **(2008)**, *128*, 197.

(89) Coronel, M. B.; Sanchis, V.; Ramos, A. J.; Marin, S.; *Food Chem. Toxicol. ,* **(2009)**, *47*, 2847.

(90) McKeague, M.; Bradley, C. R.; Girolamo, A. D.; Visconti, A.; Miller, J. D.; DeRosa, M. C.; *Int. J. Mol. Sci.*, **(2010)**, *11*, 4864.

(91) http://www.fao.org/docrep/003/x6939e/X6939e04.htm.

(92) Duffy, D. C.; McDonald, J. C.; Schueller, O. J. A.; Whitesides, G. M.; *Anal. Chem.*, **(1998)**, *70*, 4974.

(93) Xu, Y.; Takai, M.; Konno, T.; Ishihara, K.; *Lab Chip*, **(2007)**, *7*, 196.

(94) Locascio, L. E.; *Anal. Bioanal. Chem.*, **(2004)**, *379*, 325.

(95) Hunt, H. C.; Wilkinson, J. S.; *Microfluid Nanofluid,* **(2008)**, *4*, 53.

(96) The scrambled strand was generated using http://www.sirnawizard.com/scrambled.php.

(97) www.microchem.com.

(98) www.photoplotstore.com.

(99) Patrito, N.; McLachlan, J. M.; Faria, S. N.; Chan, J.; Norton, P. R.; *Lab Chip*, **(2007)**, *7*, 1813.

(100) Guieu, V. Département de Pharmacochimie Moléculaire - UMR 5063 CNRS.

(101) Willets, K. A.; Van Duyne, R. P.; *Annu. Rev. Phys. Chem.*, **(2007)**, *58*, 267.

(102) Galarreta, B. C.; Harté, E.; Marquestaut, N.; Norton, P. R.; Lagugné-Labarthet, F.; *Phys. Chem. Chem. Phys.*, **(2010)**, *12*, 6810.

(103) Hyun, J.; Ahn, S. J.; Lee, W. K.; Chilkoti, A.; Zauscher, S.; *Nano Lett.*, **(2002)**, *2*, 1203.

(104) Im, H.; Huang, X.-J.; Gu, B.; Choi, Y.-K.; *Nat. Nanotechnol.*, **(2007)**, *2*, 430.

(105) Torreggiani, A.; Fini, G.; *Biospectroscopy*, **(1998)**, *4*, 197.

(106) Ahern, A. M.; Garrell, R. L.; *Langmuir*, **(1991)**, *7*, 254.

(107) Fagnano, C.; Fini, G.; Torreggiani, A.; *J. Raman Spectrosc.*, **(1995)**, *26*, 991.

(108) Torreggiani, A.; Bottura, G.; Fini, G.; *Journal of Raman Spectroscopy*, **(2000)**, *31*, 445.

(109) Fluorescence Anisotropy. In *Principles of Fluorescence Spectroscopy*; 3rd ed.; Lakowicz, J. R., Ed.; Springer Science: New York, 2006.

(110) Prescott, B.; Steinmetz, W.; Thomas, G. J.; *Biopolymers*, **(1984)**, *23*, 235.

(111) Thomas, G. J.; *Annu. Rev. Biophys. Biomol. Struct.*, **(1999)**, *28*, 1.

(112) Lafleur, L.; Rice, J.; Thomas, G. J.; *Biopolymers*, **(1972)**, *11*, 2423.

(113) Rappoport, D.; Shim, S.; Aspuru-Guzik, A.; *Phys. Chem. Lett*, **(2011)**, *2*, 1254.

(114) Nishimura, Y.; Tsuboi, M.; *J. Mol. Struct.*, **(1986)**, *146*, 123.

(115) Bredenkamp, M. W.; Dillen, J. L. M.; van Rooyen, P. H.; Steyn, P. S.; *J. Chem. Soc. Perkin Trans. II*, **(1989)**, 1835.

(116) Galvis-Sánchez, A. C.; Barros, A. S.; Delgadillo, I.; *Anal. Chim. Acta*, **(2008)**, *617*, 59.

Chapter 7: Conclusions and Prospects

The fabrication of hexagonal array of nanotriangles inscribed over glass cover slips, described in Chapter 2, was accomplished by electron beam lithography. Such samples allow one to benefit from surface enhancements using a confocal microscope on transparent samples; and open the possibility of performing measurements using petri dishes or microfluidics channels. In addition, the use of gold as the metal provides the required compatibility to study biomolecular systems. The methodology developed in the fabrication, allows one to prepare reproducible samples, with a full control over the design. By changing the area dose of the electron beam, physical parameters of the design, such as the size of the triangles or the interparticle distance between features, can be modified. Furthermore, this advanced fabrication method brings the possibility of finely tune the plasmon bands of the hexagonal array of nanotriangles.

The characterization of the fabricated nanostructured platforms was accomplished both, experimentally and numerically. Chapters 2 and 3, correlate the experimental extinction spectra with the finite-difference time domain calculations performed on the same structures. The results show a good agreement between both approaches, and confirm the predictive character of the FDTD modeling. As a result, it was possible to interpret the results, to determine the plasmonic properties of the metallic nanostructures, and to predict the behavior of other arrays.

For the first time, this dissertation project reports how the optical properties of hexagonal array of nanotriangles are affected by a probe light, polarized with respect to the nanostructure symmetry. The analyzed data obtained revealed a change in the plasmonic properties of the structures. The strong electric field enhancement is confined to the pairs of dimeric nanotriangles with a longitudinal axis parallel to the linearly polarization of the incoming electromagnetic field. This hexagonal arrangement of nanotriangles, although

widely reported in the literature, is therefore not optimal under linearly polarized light conditions since only a portion of nanotriangles dimers will show maximum enhancement. Further considerations must be taken to improve the electric field intensity distribution of the whole assembly.

In Chapter 4, a novel experimental method is used to determine the near-field intensity distribution in the vicinity of hexagonal arrays of gold nanotriangles. The topographical deformation, upon irradiation of a thin film of azobenzene polymer coating the probed metallic surface, allows one to map the localized field enhancement regions in the array. The comparison of these results with the numerical calculations performed in a similar system helps to understand the results and to study the different electric field components responsible of such deformation.

The quantification of the surface-enhanced Raman scattering enhancement factor of the fabricated nanostructures is useful in the optimization process of these fabricated platforms. A full description was given in Chapter 5 of the different parameters that need to be taken into consideration when measuring the enhancement factor. A rigorous data analysis was performed to determine that the enhancement factor, when the prepared structures are functionalized with benzenethiol and under non-resonant conditions, is typically of the order of 10^4-10^6. Such results become extremely valuable when other surface-enhanced Raman scattering experiments are performed at the monolayer level.

The study of two different surfaces functionalized with complex molecular systems, described in Chapter 6, illustrates the multiple applications of the fabricated SERS platforms. The information collected from the SERS spectra of the Streptavidin/biotin complex, or from the conformational change of aptameric self-assembled monolayers, proves that SERS is a promising tool in the development of new molecular sensors at the monolayer level.

Finally, the studied SERS structures were integrated in the design and fabrication of a microfluidic device. Such device was used as a toxicological sensor to detect in situ the presence of a micotoxin. This simple but efficient example proves the feasibility of the fabricated SERS platforms to be integrated in the development of micro-total analysis systems.

From a prospective point of view, the fabrication methodology, developed to prepare SERS platforms, provide a very high control and reproducibility, contrary to other methods described in Chapter 2. However, one of the drawbacks of EBL is the fabrication cost. In the last few years, different groups have proposed new fabrication methods with the advantages from EBL and at low cost.[1-3] These new techniques, based in soft lithography, imprinting, nanoskiving, or high throughput nanofabrication, could potentially be used in the design of new SERS platforms; and as well as the structures studied in this project, meet all the required criteria of transparency, biocompatibility, tunability, and feasible integration in a micro-total analysis system.

The experimental and numerical characterization of the metallic nanostructures prepared in this project, proved that these two methods are complementary. As a result, a rational design of new arrays could be optimized using FDTD method prior to their fabrication in a nanofabrication facility.

One of the current limitations to probe the near-field properties of metallic nanostructures is the spatial resolution. Although, progress has been developed in this field, by using azobenzene polymers for instance, there is still work that need to be done until we are able to map the electric field distribution with the same amount of details that the calculations suggest. In this context, a possible approach could be the use of a gold coated

tip that can magnify even more the field enhancement of the nanostructures.[2,4] Furthermore, as observed in the analysis of the different electric field components, the hot-spots present a strong contribution of the out-of-plane component, a condition that is necessary to perform tip-enhanced Raman spectroscopy, more commonly referred to as 'TERS'. As a result using a gold coated AFM might lead to a precise detection of the near-field distribution of two-dimensional nanostructures, and opens the possibility to develop a new generation of molecular sensor.

In the field of bio-analysis, two systems were studied and the results show a huge potential for further development. Streptavidin- biotin is a model system broadly used in sensing fabrication.[5,6] However most of the detection methods for monolayers are not Raman-based, proving the importance of our work. One area that still needs to be developed is the analysis of the SERS spectra when other biotinylated species interact with the surface. It is important to determine if further changes in the conformation would be detectable in the Raman spectra, and if it is possible to design specific experiments to analyze different biotinylated materials.

The study on aptameric sensors, which are integrated in a microfluidic device, and whose change in conformation is detected by their SERS fingerprint spectra, is a project with enormous potential. On one hand, there is still a necessity to improve the surface chemistry of the aptameric sensor.[7,8] The studied done did not make used of a second alkanethiol,[9] to promote the orientation of the alkanethiolated aptamer, or to avoid the non specific interaction of other molecules in the media. Although, the analysis of the SERS spectra proved the presence of the aptamer in the surface and the adsorption of OTA; it is still possible to improve even more the changes in conformation. Thus, if all the molecules present the same orientation, the Raman bands would be less broad and more defined, and the background signal coming from the other molecules in the media would be minimized or removed. In addition, the SERS experiments conducted on the OTA-binding aptamer used a micromolar concentration of the toxin. Instead, the

fluorescence experiments performed for the same aptamer-OTA system presented a limit of detection in the nanomolar range. It will be important to conduct further experiments using the SERS system to match or to improve the limits of detection reported using fluorescence spectroscopy. Finally, one of the attractive characteristics of aptamers is it capability to release the target molecule when the system presents a gradient of pH or salt concentration.[10] The conception of more complex microfluidic devices with several input and output channels could be implemented opening the possibility to measure in situ complexation/decomplexation cycles that are monitored by changes in the SERS spectra.

Finally, the integration of the SERS platforms in a microfluidic device opens up the door to the fabrication of micro-total analysis systems. Although a simple example shows the possibility to design a device with the fabricated nanostructured surfaces, improvement needs to be done until this device becomes commercially useful. On one hand, the binding process used herein, allows a non covalent interaction between the PDMS and glass layer. However, this bond is not permanent and considerations must be taken when introducing the fluids, to avoid leaks. Methods to improve such PDMS/glass binding have been developed,[11,12] but in most cases they require harsh oxygen plasma cleaning of the glass slide, that will remove the metallic nanostructures. Alternatively, microfluidics done entirely in glass would be of tremendous interest avoiding the drawbacks of PDMS.[13]

7.1. References

(1) Aksu, S.; Yanik, A. A.; Adato, R.; Artar, A.; Huang, M.; Altug, H.; *Nano Lett.,* **(2010)**, *10*, 2511.

(2) Konstantatos, G.; Sargent, E. H.; *Nat. Nanotechnol.* , **(2010)**, *5*, 391.

(3) Wiley, B. J.; Qin, D.; Xia, Y.; *ACS Nano*, **(2010)**, *4*, 3554.

(4) Novotny, L.; Beversluis, M. R.; Youngworth, K. S.; Brown, T. G.; *Phys. Rev. Lett.,* **(2001)**, *86*, 5251.

(5) Wilchek, M.; Bayer, E. A.; Livnah, O.; *Immunol Lett.,* **(2006)**, *103*, 27.

(6) Wu, S.-C.; Ng, K. K.-S.; Wong, S. L.; *Proteins,* **(2009)**, *77*, 404.

(7) Cruz-Aguado, J. A.; Penner, G.; *J. Agric. Food Chem.,* **(2008)**, *56*, 10456.

(8) Cruz-Aguado, J. A.; Penner, G.; *Anal. Chem.*, **(2008)**, *80*, 8853.

(9) Balamurugan, S.; Obubuafo, A.; Soper, S. A.; McCarley, R. L.; Spivak, D. A.; *Langmuir*, **(2006)**, *22*, 6446.

(10) Jayasena, S. D.; *Clin Chem*, **(1999)**, *45*, 1628.

(11) Bhattacharya, S.; Datta, A.; Berg, J. M.; Gangopadhyay, S.; *J. Microelectromech S.*, **(2005)**, *14*, 590.

(12) Kim, J.; Surapaneni, R.; Gale, B. K.; *Lab Chip*, **(2009)**, *9*, 1290.

(13) Vulto, P.; Huesgen, T.; Albrecht, B.; Urban, G. A.; *J. Micromech. Microeng. J. Micromech. Microeng.* , **(2009)**, *19*, 077001.

Appendix A.

Copyrights

RSC | Advancing the Chemical Sciences

Rights retained by journal authors

When the author signs the exclusive Licence to Publish for a journal article, he/she retains certain rights that may be exercised without reference to the RSC. He/she may:

- Reproduce/republish portions of the article (including the abstract)
- Photocopy the article and distribute such photocopies and distribute copies of the PDF of the article that the RSC makes available to the corresponding author of the article upon publication of the article for personal or professional use only, provided that any such copies are not offered for sale.

Persons who receive or access the PDF mentioned above must be notified that this may not be further made available or distributed.

- Adapt the article and reproduce adaptations of the article for any purpose other than the commercial exploitation of a work similar to the original
- Reproduce, perform, transmit and otherwise communicate the article to the public in spoken presentations (including those which are accompanied by visual material such as slides, overheads and computer projections)

The author(s) must submit a written request to the RSC for any other use than those specified above. All cases of republication/reproduction must be accompanied by an acknowledgement of first publication of the Work by the RSC. The acknowledgement depends on the journal in which the article was published.

- For *New Journal of Chemistry* the acknowledgement is:
  - [Original citation] - Reproduced by permission of The Royal Society of Chemistry (RSC) on behalf of the Centre National de la Recherche Scientifique (CNRS) and the RSC
- For PCCP the acknowledgement is:
  - [Original citation] - Reproduced by permission of the PCCP Owner Societies
- For *Photochemical & Photobiological Sciences* the acknowledgement is:
  - [Original citation] - Reproduced by permission of The Royal Society of Chemistry (RSC) on behalf of the European Society for Photobiology, the European Photochemistry Association, and RSC
- For all other journals the acknowledgement is:
  - [Original citation] - Reproduced by permission of The Royal Society of Chemistry (RSC)

The acknowledgement should also include a hyperlink to the article on the RSC website.

The author also has some rights concerning the deposition of the whole article, details of which are given on the Author Deposition pages.

Contact and Further Information

Gill Cockhead
Contracts & Copyright Executive
Tel: +44(0) 1223 432 134
Email: Gill Cockhead

© Royal Society of Chemistry 2011

American Chemical Society's Policy on Theses and Dissertations

If your university requires you to obtain permission, you must use the RightsLink permission system.
See RightsLink instructions at http://pubs.acs.org/page/copyright/permissions.html.

This is regarding request for permission to include **your** paper(s) or portions of text from **your** paper(s) in your thesis. Permission is now automatically granted; please pay special attention to the **implications** paragraph below. The Copyright Subcommittee of the Joint Board/Council Committees on Publications approved the following:

> Copyright permission for published and submitted material from theses and dissertations
> ACS extends blanket permission to students to include in their theses and dissertations their own articles, or portions thereof, that have been published in ACS journals or submitted to ACS journals for publication, provided that the ACS copyright credit line is noted on the appropriate page(s).
>
> Publishing **implications** of electronic publication of theses and dissertation material
> Students and their mentors should be aware that posting of theses and dissertation material on the Web prior to submission of material from that thesis or dissertation to an ACS journal may affect publication in that journal. Whether Web posting is considered prior publication may be evaluated on a case-by-case basis by the journal's editor. If an ACS journal editor considers Web posting to be "prior publication", the paper will not be accepted for publication in that journal. If you intend to submit your unpublished paper to ACS for publication, check with the appropriate editor prior to posting your manuscript electronically.

Reuse/Republication of the Entire Work in Theses or Collections: Authors may reuse all or part of the Submitted, Accepted or Published Work in a thesis or dissertation that the author writes and is required to submit to satisfy the criteria of degree-granting institutions. Such reuse is permitted subject to the ACS' "Ethical Guidelines to Publication of Chemical Research" (http://pubs.acs.org/page/policy/ethics/index.html); the author should secure written confirmation (via letter or email) from the respective ACS journal editor(s) to avoid potential conflicts with journal prior publication*/embargo policies. Appropriate citation of the Published Work must be made. If the thesis or dissertation to be published is in electronic format, a direct link to the Published Work must also be included using the ACS Articles on Request author-directed link – see http://pubs.acs.org/page/policy/articlesonrequest/index.html

* Prior publication policies of ACS journals are posted on the ACS website at
http://pubs.acs.org/page/policy/prior/index.html

If your paper has **not** yet been published by ACS, please print the following credit line on the first page of your article: "Reproduced (or 'Reproduced in part') with permission from [JOURNAL NAME], in press (or 'submitted for publication'). Unpublished work copyright [CURRENT YEAR] American Chemical Society." Include appropriate information.

If your paper has already been published by ACS and you want to include the text or portions of the text in your thesis/dissertation, please print the ACS copyright credit line on the first page of your article: "Reproduced (or 'Reproduced in part') with permission from [FULL REFERENCE CITATION.] Copyright [YEAR] American Chemical Society." Include appropriate information.

Submission to a Dissertation Distributor: If you plan to submit your thesis to UMI or to another dissertation distributor, you should not include the unpublished ACS paper in your thesis if the thesis will be disseminated electronically, until ACS has published your paper. After publication of the paper by ACS, you may release the entire thesis (**not the individual ACS article by itself**) for electronic dissemination through the distributor; ACS's copyright credit line should be printed on the first page of the ACS paper.

10/10/03, 01/15/04, 06/07/06, 04/07/10, 08/24/10, 02/28/11

Curriculum Vitae

Name: Betty C. Galarreta

Post-secondary Education and Degrees:
Pontificia Universidad Católica del Perú
Lima, Peru
2000-2006 B.Sc. Chemistry

Honours and Awards:
- Dissertation Year Fellowship Award (UWO), 2010-2011
- Western Graduate Research Scholarship. 2007-2011
- First Place Poster Presentation, NanoOntario, 2010
- Graduate Thesis Research Award (UWO), 2010
- Best Poster Presentation in Surface Science Division (CSC), 2009

Related Work Experience
Teaching Assistant
The University of Western Ontario
2007-2010

Publications:

1. Hug, S.; Grohe, B.; Jalkanen, J.; Chan, B.; **Galarreta, B. C.**; Vincent, K.; Lagugné-Labarthet, F.; Lajoie, G.; Goldberg, H. A.; Karttunen, M.; Hunter, G. K. *Soft Matter*, submitted.
2. **Galarreta, B. C.**; Rupar, I.C.; Young, A.; Lagugné-Labarthet, F.; *J. Phys. Chem. C*; in press.
3. **Galarreta, B. C.**; Norton, P. R.; Lagugné-Labarthet, F.; *Langmuir*, **(2011)**; *27*: 1494.
4. **Galarreta, B. C.**; Norton, P. R.; Lagugné-Labarthet, F.; *J. Phys. Chem. C*, **(2010)**; *114*: 19952.
5. **Galarreta, B. C.**; Harté, E.; Norton, P. R.; Lagugné-Labarthet, F.; *Phys. Chem. Chem. Phys.*. **(2010)**; 12: 6810.
6. Varma, S.; McLachlan, J.; Leclair, A.M.; **Galarreta, B. C.**; Norton, P. R.; Lagugné-Labarthet, F.; *Anal. Bioanal. Chem.* **(2010)**; 396: 1159.
7. **Galarreta B. C.**; Sifuentes, R.; Carrillo, A. K.; Sanchez, L.; Amado, M. R. I.; Maruenda, H. *Bioorg. Med. Chem.* **(2008)**; *16*: 6689.

.